



Syed Hamza Safer Gardezi

**Atomically Thin Semiconducting
Transition-Metal Dichalcogenides: From
Synthesis to Electro-Optical Properties**

Tese de Doutorado

Thesis presented to the Programa de Pós-graduação em Física of PUC-Rio in partial fulfillment of the requirements for the degree of Doutor em Ciências - Física.

Advisor: Prof. Victor Carôzo Gois de Oliveira

Rio de Janeiro
September 2020

Syed Hamza Safeer Gardezi

**Atomically Thin Semiconducting
Transition-Metal Dichalcogenides: From
Synthesis to Electro-Optical Properties**

Thesis presented to the Programa de Pós-graduação em Física of PUC-Rio in partial fulfillment of the requirements for the degree of Doutor em Ciências - Física. Approved by the Examination Committee:

Prof. Victor Carôzo Gois de Oliveira

Advisor

Departamento de Física – PUC-Rio

Prof. Fernando Lázaro Freire Junior

Departamento de Física – PUC-Rio

Prof. Isabel Cristina dos Santos Carvalho

Departamento de Física – PUC-Rio

Prof. Cristiano Fantini Leite

UFMG

Prof. Bruno Ricardo de Carvalho

UFRN

Prof. Daniel Grasseschi

UFRJ

Rio de Janeiro, September 29th, 2020

All rights reserved. Total or partial reproduction of this work is forbidden without the authorization of the university, the author, and the advisor.

Syed Hamza Safeer Gardezi

Obtained his Master's degree in Physics from Quaid-i-Azam University, Islamabad, Pakistan.

Bibliographic data

Syed Hamza Safeer Gardezi

Atomically Thin Semiconducting Transition-Metal Dichalcogenides: From Synthesis to Electro-Optical Properties / Syed Hamza Safeer Gardezi; advisor: Victor Carôzo Gois de Oliveira. – Rio de Janeiro: PUC-Rio, Departamento de Física, 2020.

v., 141 f: il. color. ; 30 cm

Tese (doutorado) - Pontifícia Universidade Católica do Rio de Janeiro, Departamento de Física.

Inclui bibliografia

1. Informática – Teses. 2. Dicalcogenetos de metais de transição;. 3. APCVD;. 4. Síntese;. 5. Raman;. 6. Fotoluminescência;. 7. Cálculos de primeiros princípios;. 8. Geração de segundo harmônico;. 9. óptica não linear;. 10. Defeitos;. 11. Dispositivos..

I. Victor Carôzo Gois de Oliveira. II. Pontifícia Universidade Católica do Rio de Janeiro. Departamento de Física. III. Título.

“Dedicated to my beloved parents”
For their love, endless support,
encouragement and sacrifices.

Acknowledgments

(All praises to ALLAH ALMIGHTY, The Creator and Sustainer of The Universe, The most gracious, The invincible and the all-wise. All esteem to His Holy Prophet Muhammad (Peace be upon Him) for eternal source of guidance and knowledge for mankind.)

This work would not have been possible without the help and support of many people, and I hereby would like to take the opportunity to thank them. First of all, my supervisor Prof. Victor Carozo. His enthusiasm for my project and his constant belief in my abilities have been an invaluable support. He always encouraged my ideas and gave me the freedom and financial framework to realize them.

I would like to thank Prof. Fernando Lazaro head of our group and Prof. Marcelo da Costa for allowing me to work in their laboratory and added their scientific knowledge from time to time to make our work better and successful.

My colleagues at Van de Graaff Laboratory, most notably André do Nascimento, Zhang Shuai, Antônio Federico, Ceser Diaz, Neileth Stand, Cintia Aparecida, Nilton and, Suellen Tozetti, who helped by raising questions and having conversations to create a pleasant working environment. I enjoyed my discussions with them, and thanks to Ceser Diaz for doing SEM on our sample.

I extend a special thank you to Michael Nazarkovsky from Chemistry department for collaborating with us in a project and helping me in understanding the chemical aspects of my work.

I would like to thank Prof. Christiano de Matos from Mack Graphe, Mackenzie University, S.P, for collaboration on the non-linear optical properties of our samples, and allowing me to work in his laboratory. Prof. Isabel Carvalho who gave the idea to work on the non-linear properties. I acknowledge the use of the Mack Graphe, Mackenzie University, S.P. and special thanks to Alaxandre Samuel who measured the SHG for us.

I would like to thank Prof. Marcus Moutinho from Núcleo Multidisciplinar de Pesquisas em Computação NUMPEX-COMP, Campus Duque de Caxias, UFRJ, who performed the first-principle calculations.

I acknowledge the use of the Brazilian National Laboratory of Nanoscience and Nanotechnology (LABNANO/CBPF). I acknowledge the use of the XFlow Chemistry and Nanochemistry Lab, PUC-Rio for Raman measurements. This study was financed in part by the Coordenação de Aperfeiçoamento de Pessoal de Nível Superior - Brasil (CAPES) - Finance Code 001. I acknowledge support from CNPq grant numbers 304144/2018-5 and 429773/2018-8.

Thank you to my Pakistani friends who give me the backup all the time, not a single moment I felt that I am away from my family, namely Adnan Raza, Rafqat Ali, Quaid Zaman, Tahir Jan, Asmat Pervaiz, Khalil ur Rehman and Rafi Khan.

And most of all, my family in Pakistan. I cannot express in words how grateful I am for your understanding and encouragement, and the constant love and support you have given me during all my life. Especially, I would like to thank my mother, who always pray for me back home and I thought its because of her prayers I achieve success.

Finally, thank you to the Brazilian government for giving me the opportunity to study in such a beautiful country. I experienced no discrimination here, Brazilian people are very friendly and hospitable, wherever I traveled in Brazil. I will not forget the time I spent here, my entire life.

Abstract

Syed Hamza Safeer Gardezi; Victor Carôzo Gois de Oliveira (Advisor). **Atomically Thin Semiconducting Transition-Metal Dichalcogenides: From Synthesis to Electro-Optical Properties**. Rio de Janeiro, 2020. 141p. Tese de doutorado – Departamento de Física, Pontifícia Universidade Católica do Rio de Janeiro.

The aim of this work was to develop reliable and repeatable methods for growing high-quality monolayer MoS₂, WS₂, and their vertical heterostructure by atmospheric pressure chemical vapor deposition (APCVD) technique. The monolayer of these materials have vital importance in the fabrication of new optical and nanoelectronic devices. Thin and low-cost devices have increased the demand for new synthesis processes. Usually, the synthesis requires temperatures around 800°C, which is an issue for applications mentioned above. In this thesis, we propose a new route using the APCVD technique to grow monolayers of MoS₂ at 550°C mediated by sodium as a catalyst. We have produced single crystals and polycrystals by controlling the NaNO₃/MoO₃ precursor's ratio and growth time. Using first-principles calculations, we find out that sodium is the nucleation site of the growth process. The precursor's ratio is crucial to decrease the energy formation and the synthesis temperature. First-principles calculations and experiments agree with the ideal precursor's rate of 0.3 and with the decrease of the synthesis temperature of 250°C. We investigated the CVD grown sample with X-ray photoelectron spectroscopy, atomic force microscopy, Raman spectroscopy, photoluminescence spectroscopy, and transport experiments.

Few layers of TMDs allow us to create new materials and find new physical phenomena. The stacking sequence in few-layer TMDs can significantly impact on their electrical and optical properties. We also synthesized few layers of MoS₂ and WS₂ via APCVD. Two and three layers of MoS₂, WS₂, and their vertical heterostructures were characterized by second harmonic generation (SHG). The SHG shows that the layers in bilayers grow with 0° or 60° has different phase stacking. The SHG from 0° stacked bilayer has increased when compared to monolayer, while the generated signal from bilayer with 60° stacking is zero. This behavior of SHG suggests that the two layers of MoS₂ or WS₂ when stacked at 0° have no inversion symmetry to 3R(AB) phase stacking between the top layer and the bottom layer. While when stacked with 60° has inversion symmetry (Centrosymmetric) and have 2H(AA') phase stacking.

Finally, the devices were fabricated on good quality samples to investigate their electrical performance. The fabricated devices show typical n-type

behavior and mobility was estimated by measuring transport curves. The dependence of Raman modes of our heterostructure device with electron doping was also studied. By applying a voltage across our device the A'_1 mode shows blueshift and a new mode emerges at $\sim 410 \text{ cm}^{-1}$, which is attributed to the defects (D) in the crystal.

Keywords

Transition metal dichalcogenide; APCVD; Synthesis; Raman; Photoluminescence; First-principles calculations; Second harmonic generation; Nonlinear optics; Defects; Devices.

Resumo

Syed Hamza Safeer Gardezi; Victor Carôzo Gois de Oliveira. **Dicalcogenetos de metal de transição semicondutores atômicamente finos: da síntese às propriedades eletro-ópticas.** Rio de Janeiro, 2020. 141p. df de Doutorado – Departamento de Física, Pontifícia Universidade Católica do Rio de Janeiro.

O objetivo deste trabalho foi desenvolver métodos eficientes e reproduzíveis de crescimento de monocamadas de WS_2 , MoS_2 e outras heteroestruturas verticais por deposição química em fase de vapor à pressão atmosférica (APCVD). A monocamada separada destes materiais tem grande importância na fabricação de novos dispositivos óticos e Nano eletrônicos. Dispositivos finos e de baixo custo necessitam temperaturas em torno de $800^\circ C$, o que é um problema para aplicações mencionadas acima. Nesta tese, nós propusemos uma nova rota usando APCVD para crescer monocamadas de MoS_2 a $550^\circ C$, usando sódio como catalisador. Nós produzimos monocristais e poli cristais controlando a razão de precursores $NaNO_3/MoO_3$ e tempo de crescimento. Usando cálculos de primeiros princípios, mostramos que o sódio atua como centro de nucleação para o processo de síntese. A razão de precursores é crucial para diminuir a energia de formação e a temperatura de síntese. Cálculos de primeiros princípios e experimentos concordam que uma razão ideal é em torno de 0.3, proporcionando uma queda de $250^\circ C$ na temperatura de crescimento. Nós investigamos as amostras crescidas por APCVD usando espectroscopia de fotoelétrons induzidos por raios-X, microscopia de força atômica, espectroscopia Raman, fotoluminescência e mediadas de transporte.

Dicalcogenetos de metais de transição (TMD) dispostos em poucas camadas permitem-nos criar materiais e estudar novos fenômenos físicos. A sequência de empilhamento dos TMDs pode modificar suas propriedades óticas e elétricas. Também sintetizamos poucas camadas de MoS_2 e WS_2 usando APCVD. Duas e três camadas de WS_2 , MoS_2 e suas heteroestruturas verticais foram caracterizadas através de geração de segundo harmônico (SHG). SHG mostra que as bicamadas crescidas com ângulos de rotação relativos de 0° e 60° possuem diferentes fases de empilhamento. O SHG do empilhamento bicamada com ângulo relativo de 0° aumentos, enquanto para amostras com empilhamento de 60° foi zerado. Este comportamento do SHG sugere que duas camadas de MoS_2 ou WS_2 , quando empilhados a 0° não possuem simetria de inversão para 3R(AB) entre as camadas inferiores e superiores, enquanto as camadas de 60° possuem simetria de inversão (centrossimétricas) e possuem empilhamento na forma 2H(AA).

Finalmente, dispositivos foram fabricados em amostras de boa qualidade para a investigação de sua performance elétrica. Os dispositivos mostram comportamento típico tipo-n e sua mobilidade foi estimada a partir das curvas de transporte. A dependência dos modos Raman das nossas amostras de heteroestruturas também foi estudada. Aplicando uma tensão nos dispositivos, o modo A'_1 mostrou um desvio para o azul e um novo modo surge em 410 cm^{-1} , atribuídos defeitos (D) no cristal.

Palavras-chave

Dicalcogenetos de metais de transição; APCVD; Síntese; Raman; Fotoluminescência; Cálculos de primeiros princípios; Geração de segundo harmônico; óptica não linear; Defeitos; Dispositivos.

Table of contents

1	Introduction	22
2	Properties of Transition Metal Dichalcogenides	27
2.1	Introduction to Transition Metal Dichalcogenides	27
2.1.1	Structure of TMDs	28
2.1.2	Stacking Sequences of Two Layers	29
2.2	Phonon Dispersion	31
2.3	Electronic Dispersion	32
2.4	Linear Optical Spectroscopy	34
2.4.1	Photoluminescence in TMDs	34
2.4.2	Raman Modes in TMDs	36
2.5	Non-Linear Optical Spectroscopy	38
2.6	Photoelectron Spectroscopy	39
3	Experimental Methodology	41
3.1	Chemical Vapor Deposition	41
3.1.1	Preparation of the Substrate	43
3.1.2	Precursors and Crucible	43
3.1.3	Growth Process	43
3.1.4	Synthesis of Bilayers MoS ₂ , WS ₂ , and MoS ₂ /WS ₂ Vertical Heterostructures	45
3.2	Optical Microscope	46
3.3	Scanning Electron Microscope	47
3.4	Raman Spectroscopy	49
3.4.1	Raman Effect	49
3.4.2	Theory of Raman Scattering	50
3.4.3	Raman Spectrometer	51
3.5	Photoluminescence Spectroscopy	53
3.6	Atomic Force Microscopy	55
3.7	X-ray Photoelectron Spectroscopy	56
3.8	Introduction to Second Harmonic Generation	58
3.8.1	Second Harmonic Generation Measurements	59
3.9	Device Fabrication	61
3.9.1	Resist Coating	62
3.9.2	Lithography	62
3.9.3	Development	65
3.9.4	Metal deposition	65
3.9.5	Lift off	66
3.10	Electrical Measurements	67
3.10.1	Electro-Raman	68
4	CVD Grown MoS ₂ , WS ₂ Monolayer, and their Vertical Heterostructure	69
4.1	Introduction	69
4.2	MoS ₂ and WS ₂ Monolayer	69

4.3	MoS ₂ /WS ₂ Vertical Heterosctructure	74
4.4	Sodium Mediated Low Temperature Synthesis of Monolayers of Molybdenum Disulfide	75
4.4.1	Catalytic Behaviour of Na Explained by DFT Calculations	79
4.4.2	Chemical Equations Explaining the Growth	82
4.4.3	Characterization of Na Mediated Synthesized Samples	82
4.5	Synthesis of MoS ₂ on Glass	86
4.6	Partial Conclusion	88
5	Second Harmonic Generation in Two and Three Layers of Transition Metal Dichalcogenides	90
5.1	Introduction	90
5.2	Two and Three Layers of Transition Metal Dichalcogenides	90
5.3	Raman and Photoluminescence of Trilayer Samples	92
5.4	Second Harmonic Generation in Two and Three Layers of MoS ₂ , WS ₂ with Different Stacking Orientation	95
5.4.1	SHG in MoS ₂ /WS ₂ Heterostructure with Different Stacking Orientation	101
5.4.2	Interference of Two S.H Fields	103
5.5	Partial Conclusion	104
6	Electrical Measurements	106
6.1	Introduction	106
6.2	Field Effect Transistor	107
6.2.1	Operating Principle of FETs	107
6.3	Device Structure	108
6.4	Transport Measurement of MoS ₂	109
6.5	Transport Measurement of WS ₂	111
6.6	Transport Measurement of MoS ₂ /WS ₂ Heterostructure	112
6.7	Defect Related Raman Peak Reveled by Electro-Raman of MoS ₂ /WS ₂ Device	113
6.8	Partial Conclusion	116
7	Conclusions and Future Work	117
	Bibliography	120

List of figures

- Figure 2.1 Periodic table and different TMDs. 28
- Figure 2.2 (a) 3D representation of the layered structure of transition metal dichalcogenides (TMDs). Adopted from [63]. (b) Archetypal coordination in TMDs. Octahedral coordination (left) triangular prismatic coordination (right) and top view of monolayers constructed from octahedral (left) and triangular prismatic (right) coordination. Adopted from [86]. 29
- Figure 2.3 Side and top views of (a) 2H stacking pattern of bilayer MX_2 , 2H is the most stable stacking pattern (also named as AA' stacking)(b) 3R (also named as AB stacking) 30
- Figure 2.4 (a) Phonon dispersion curve of monolayer MoS_2 calculated by A.Molina, et al. [90]. (b) and WS_2 . 31
- Figure 2.5 Electronic band structures of (a) bulk MoS_2 and, (b) monolayer MoS_2 calculated from first principles using DFT–GGA approach. Valence band maxima and conduction band minima are indicated by red and blue circles, respectively. Energies are given relative to the VBM. Schematic drawings of low-energy bands in (c) bulk MoS_2 and (d) monolayer MoS_2 showing the band gaps E_g , as well as the valence band spin–orbit splitting Δ_{so} and the Γ valley band offset $\Delta_{\Gamma-K}$ for the case of monolayer MoS_2 . The band structure was adopted from [103]. 33
- Figure 2.6 Absorption (gray lines) and PL (color lines) spectra of monolayer semiconducting TMDs crystals (MoS_2 , MoSe_2 , WS_2 , WSe_2). Measurements were made on layers produced by mechanical exfoliation of bulk crystals. The photoluminescence peak coincides with the bandgap exciton absorption peak. Adopted from [107]. 35
- Figure 2.7 (a) Raman active modes of monolayer TMDs. (b) Schematics of triangular shape TMDs, the grey atom is a transition metal and yellow is the chalcogen. (c) Raman spectra of MoS_2 and WS_2 showing vibrational modes inset are their triangular structure. 37
- Figure 2.8 SHG characteristics from MoS_2 (a) Power dependence of SHG from a monolayer MoS_2 , the upper inset shows the fundamental spectra (red) and the SHG (blue). The lower inset shows the layer-dependent intensity of the SHG. Adopted from [52]. (b) SHG and THG intensities as functions of the number of layers. Adopted from [122]. 38
- Figure 3.1 (a) Schematic diagram for the CVD synthesis of TMDs inside a quartz tube, showing the crucibles, and the substrate, two zones are heated independently at different temperatures. (b) CVD system at Protective Coatings and Nanostructured Materials Laboratory vandegraaff PUC-Rio. 42

Figure 3.2 (a) Alumina crucible showing three different positions of the substrate. In every position substrate is facing downwards.	
(b) Temperature profile of the growth procedure, Ar flow rate is 100 sccm during the whole process.	44
Figure 3.3 Optical images of some CVD grown TMDs. (a) WS ₂ monolayer on SiO ₂ /Si 300 nm. (b) WS ₂ monolayer on quartz.	
(c) Bilayer MoS ₂ on SiO ₂ /Si 300 nm. Scale bars are 10 μm	45
Figure 3.4 (a) Schematic of an optical microscope image formation.	
(b) ZEISS Axio Scope. A1 at Protective Coatings and Nanostructured Materials Laboratory Vandegraff PUC-Rio.	47
Figure 3.5 (a) Schematic of a SEM image formation. Adopted from [140]. (b) JEOL JSM-7610F Field Emission SEM at vandegraff PUC-Rio.	48
Figure 3.6 Stokes and anti-Stokes Raman scattering.	51
Figure 3.7 (a) Schematics of Raman spectrometer. (b) NT-MDT, NTEGRA Spectrometer at Protective Coatings and Nanostructured Materials Laboratory Vandegraff PUC-Rio.	52
Figure 3.8 Schematic diagram of the PL experimental setup.	54
Figure 3.9 Cantilever deflection detection scheme by means of a beam of laser. Adopted from [146].	56
Figure 3.10 Experimental setup for XPS. Adopted from [152].	57
Figure 3.11 General second harmonic generation phenomena.	58
Figure 3.12 (a) Schematic diagram of harmonic generation (SHG and THG) microscopy system. (b) Experimental setup for harmonic generation measurements at Mackgraphe, Mackenzie Presbyterian University, SP.	60
Figure 3.13 (a) Spin coater (model WS-650Hzb-23NPPB-UD-3, at labnano CBPF) was used to cover our sample with a resist. (b) Heating the sample coated with resist on a hot plate.	62
Figure 3.14 Laser writer lithography system model Heidelberg μPG 101 Laser writer at lab nano CBPF.	63
Figure 3.15 (a) Design on a LibreCAD program. (b) Optical images of a sample after development on which dose test was performed with different laser powers.	64
Figure 3.16 Edwards thermal evaporator equipment at vandegraff PUC-Rio.	66
Figure 3.17 General device fabrication procedure.	67
Figure 3.18 Experimental setup for transport measurements.	67
Figure 3.19 Schematic of the experimental setup.	68
Figure 4.1 (a) Optical microscopy images of MoS ₂ grown on SiO ₂ /Si 285 nm, scale bars are 50 μm and 20 μm. (b) Optical images of WS ₂ grown on SiO ₂ /Si 400 nm.	70
Figure 4.2 (a) AFM topography, profile of MoS ₂ flake, inset the line profile shows the step of 1 nm. (b) AFM image of WS ₂ flake.	71
Figure 4.3 Raman spectra of MoS ₂ at different excitation wavelengths.	71
Figure 4.4 Raman spectra of WS ₂ at different excitation wavelengths.	72
Figure 4.5 (a) Photoluminescence spectra of monolayer MoS ₂ . (b) Photoluminescence spectra of monolayer WS ₂ .	73

- Figure 4.6 (a,b) Optical images of MoS₂/WS₂ vertical heterostructure scale bar is 20 μm. (c) Raman spectra of MoS₂/WS₂ heterostructure taken at point 1 and 2 as shown in figure 4.6(b). (d) Photoluminescence of the same triangle at point 1 and 2. 74
- Figure 4.7 Dependence of synthesis parameters in the growth process. (a) Optical images of single-crystalline MoS₂ changing the precursor's ratio NaNO₃/MoO₃ from 0.3 to 3.0. (b) Optical images show the island coalescence and form the polycrystal MoS₂ by increasing the time from 14 to 20 min, scale bar 10 μm. 76
- Figure 4.8 SEM images of MoS₂ single crystals. 77
- Figure 4.9 XPS experiments. (a) XPS spectra of the grown sample before and after water bath for 2 hr. (b) Detailed XPS spectra of Na 1s peak before and after water bath. Detailed XPS spectra and fitting of Mo and S peaks. (c) Molybdenum 3d spectrum of MoS₂ grown on SiO₂/Si substrate. (d) S 2p spectrum of the same sample. 78
- Figure 4.10 DFT calculations of the formation energy. (a-f) Atomic positions after minimization of the energy and forces in a 3 × 3 fixed size supercell of MoS₂ in the presence of Na atoms. The light blue, dark grey and dark yellow balls represent the Na, Mo, and S atoms, respectively. (g) Formation energy per atom computed with the MoS₂ constrained by the presence of the Na after the minimization (black circles) and fully relaxed (red circles). The full black and red lines are guides to the eyes. The vertical axis on the right side is a conversion of energy to temperature. 80
- Figure 4.11 Final structures for large concentrations of Na in MoS₂. (a-c) top view of the 3 × 3 MoS₂ supercell with 7, 8, and 9 Na atoms, respectively. (d-f) side view of the same structures in (a-c), respectively. The average distance between Na atoms and the plane with Mo are approximately 4.0 Å (first layer) and 5.8 Å (second layer). For the low concentration regimes (i.e. < 0.45) the average distance varies approximately linearly between 3.7 Å and 4.0 Å with the number of the Na atoms in the supercell. 81
- Figure 4.12 Characterization of single crystal. (a) AFM image of a monolayer of MoS₂, inset the line profile shows the step of 1 nm. (b) Raman spectra of MoS₂ monolayer from 473 nm laser line took from (a). (c) mapping of A₁' intensity mode and (d) E' intensity mode, scale bar 1 μm. (e) The peak position maps of E' and (f) A₁' modes showing uniformity throughout the triangles area. (g) Photoluminescence spectra took of MoS₂. (h) PL intensity map of A exciton, scale bar 1 μm. (i) fwhm of Photoluminescence. 83
- Figure 4.13 Characterization of polycrystal. (a) AFM image of polycrystalline MoS₂. (b) Raman mapping of E' intensity mode and (c) A₁' intensity mode, scale bar 2 μm. (d) peak position maps of E' and, (e) A₁' mode (f) PL intensity map, scale bar 2 μm. 84

- Figure 4.14 Analysis of defects using Raman spectroscopy. (a) Raman spectra of single and polycrystal of MoS₂ with the fitting. (b) Normalized intensity of LA mode in the function of E' frequency. (c) Histograms of LA mode of single and polycrystals. 85
- Figure 4.15 (a) Optical image MoS₂ on glass scale bar is 10 μm. (b) AFM image of a monolayer triangle with height of ~ 1 nm scale bar is 2 μm. (c) Raman and, (d) PL spectra of the corresponding triangle. (e) Intensity map of E', (f) A₁' modes of the same triangle. (g) PL intensity map. 87
- Figure 5.1 Optical microscopy image of the as-grown (a) MoS₂ trilayer stacked with same crystal orientation between each layer scale bar is 20 μm (b) MoS₂ bilayer stacked with opposite crystal orientation to the monolayer (c) WS₂ trilayer first two triangles are stacked with same crystal orientation while the third triangle is stacked with 60° w.r.t other layers scale bar is 10 μm (d) WS₂ bilayer stacked with opposite crystal orientation (e) MoS₂/WS₂ heterostructure stacked at 0° and (f) 60°, scale bar is 10 μm. 91
- Figure 5.2 (a) Raman spectra of MoS₂ trilayer stacked with same crystal orientation between each layer shown in figure 5.1(a). (b) Log of photoluminescence intensity of the three layers, decrease in intensity refers to shifting towards indirect band gap. 93
- Figure 5.3 (a) Raman spectra of WS₂ trilayer shown in figure 5.1(c). (b) Log of photoluminescence intensity of the three layers. 93
- Figure 5.4 Band gap of 4L, 2L, and 1L of MoS₂ calculated by Splandani et al. [9]. The solid arrows indicate the lowest energy transitions. The direct excitonic transitions occur at high energies at **K** point. With reduced layer thickness, the indirect bandgap becomes larger, while the direct excitonic transition barely changes. For monolayer MoS₂, it becomes a direct bandgap semiconductor. This dramatic change of electronic structure in monolayer MoS₂ can explain the observed jump in monolayer photoluminescence efficiency. 94
- Figure 5.5 (a) Raman and (b) PL mapping images of the WS₂ trilayer shown in figure 5.1(c). 95
- Figure 5.6 Single spectra of MoS₂ flake shown in figure 5.1(a), showing second-harmonic and third-harmonic signals. 96
- Figure 5.7 Intensity dependence of the SHG signal with the polarization angle. (a) Trilayer (green) with a twisted angle of 0° between bilayer (red) and monolayer (black). (b) bilayer (red) twisted 60° from monolayer (black). 96
- Figure 5.8 Schematics of (a) Top view of the MoS₂ crystallographic orientation with respect to the incident laser polarization e_ω. (b) Orientational dependence of SHG. 97
- Figure 5.9 Polarization plot shown in figure 5.7(a), fitted with a sine wave function (black line) showing no phase difference between each layer. 98

- Figure 5.10 Schematics of relative stacking orientation of the top and bottom layers. (a) 3R(AB) phase, the metal atom is located at the center of the bottom hexagon. Thus has a no-inversion symmetry. (b) 2H(AA') phase, the metal atom of the second layer sits precisely on top of the chalcogen atom of the bottom layer, has the inversion symmetry. 99
- Figure 5.11 THG, constant intensity with θ (a) Trilayer MoS₂ shown in figure 5.1(a) (b) Bilayer MoS₂ shown in figure 5.1(b). 100
- Figure 5.12 Intensity dependence of the SHG signal with the polarization angle. (a) Trilayer (green) with twisted angle of 0° between bilayer(red) and monolayer (black). (b) bilayer (red) twisted 60° from monolayer (black). 100
- Figure 5.13 Intensity dependence of the SHG signal with the polarization angle. (a) MoS₂/WS₂ heterostructure 0°. and (b) MoS₂/WS₂ heterostructure 59°. 101
- Figure 5.14 Optical image of MoS₂/WS₂ heterostructure 60°, and its intensity dependence of the SHG signal with the polarization angle. 102
- Figure 5.15 Schematics of relative stacking orientation of the top and bottom layers. (a) MoS₂/WS₂ 0°. (b) MoS₂/WS₂ 60°, mismatch between the masses of Mo and W atoms results in SHG. 102
- Figure 5.16 Schematic for illustrating the vector superposition of the second harmonic fields. 104
- Figure 6.1 Illustration of the structure of a FET 107
- Figure 6.2 (a) Schematic representation of FET devices. (b) Optical image of a back gate FET device fabricated on SiO₂/Si, showing drain and source electrodes and channels L and W. 108
- Figure 6.3 Transport measurements. (a) Transfer curve (I_{DS} vs. V_G) with V_{DS} fixed at 1 V, for MoS₂ single crystal. (b) Output curve (I_{DS} vs. V_{DS}) at different V_G values, for single crystal. (c) Transfer curve (I_{DS} vs. V_G) with V_{DS} fixed at 1 V for MoS₂ polycrystalline film. (d) Output curve (I_{DS} vs. V_{DS}) at different V_G values, for polycrystalline film. 110
- Figure 6.4 (a) Optical image of a FET device fabricated after transferring WS₂ on SiO₂/Si substrate, scale bar is 10 μ m. (b) Transfer curve (I_{DS} vs. V_G) with V_{DS} fixed at 1.5 V for WS₂. (c) Output curve of WS₂ (I_{DS} vs. V_{DS}) for different V_G values. 111
- Figure 6.5 (a) Optical image of MoS₂/WS₂ heterostructure device on SiO₂/Si 285 nm substrate. The big triangle is the MoS₂ and on top of it flower shape is an incomplete grown WS₂ triangle. (b) Output curve of MoS₂/WS₂ (I_{DS} vs. V_{DS}) for different V_G values. 112
- Figure 6.6 Raman spectra of MoS₂/WS₂ device at different back gate voltages V_G , laser wavelength 473 nm. Red circles are experimental data points, the black lines are Lorentzian fits to the total spectrum. 114
- Figure 6.7 (a) Peak position of W-A'₁ and Mo-A'₁ as a function of V_G . (a) FWHM of W-A'₁ and Mo-A'₁ peak as a function of V_G . 115

Figure 6.8 (a) Intensity normalized with Si peak Mo-A₁' and W-A₁' as a function of V_G . (b) Normalized intensity of D peak as a function of V_G .

115

List of tables

Table 3.1	Growth parameters for different TMDs. In all synthesis powder is placed into the boat with the substrate facing down.	46
Table 5.1	Normalized SHG intensity and phase of TMD's.	103
Table 6.1	Average conductivity and mobility of TMDs.	113

Knowledge is better than wealth: Knowledge protects you, whereas you have to protect wealth. Wealth decreases with spending, whereas knowledge increases with it.

Hazrat Ali (A.S), .

List of Abbreviations

TMDs – Transition Metal Dichalcogenides
MoS₂ – Molybdenum disulfide
WS₂ – Tungsten disulfide
CVD – Chemical Vapor Deposition
2D – Two Dimension
BZ – Brillouin zone
hBN – Hexagonal boron nitride
VBM – Valence band maximum
CBM – Conduction band minimum
FWHM – Full width at half maximum
PL – Photoluminescence
AFM – Atomic Force Microscopy
XPS – X-ray Photoelectron Spectroscopy
SEM – Scanning Electron Microscopy
PL – Photoluminescence
LA – Longitudinal acoustic
TA – Transverse acoustic
IR – Infrared
DFT – Density functional theory
SHG – Second Harmonic Generation
THG – Third Harmonic Generation
 $\chi^{(1)}$ – First order nonlinearity
 $\chi^{(2)}$ – Second order nonlinearity
 $\chi^{(3)}$ – Third order nonlinearity
FET – Field Effect Transistor
MOSFETs – Metal-oxide Field Effect Transistor

1 Introduction

The discovery of graphene has opened an entirely new field of research in Material Science [1–3]. It became one of the most studied materials in the past years. Even though graphene has a unique electronic structure, exceptional strength, excellent electrical conductivity but it lacks a bandgap and consequently is not suitable for digital electronic applications. There are other layered materials that can be thinned down to monolayers [4]. One important family of layered or two-dimensional (2D) materials is the family of transition metal dichalcogenides (TMDs) [5–7]. Till now, more than 40 transition metal dichalcogenides have been discovered [8]. They have been studied for a long time in their bulk form [9, 10], but their properties when in the monolayer form differ from their bulk characteristics. In particular, molybdenum and tungsten based TMDs are atomically thin semiconductors with band gaps ranging from the visible to the near-infrared region. Bulk MoS₂ and WS₂ possess an indirect bandgap, while their monolayers have a direct bandgap [11]. So these two are more useful in all of the TMDs. This thesis does not attempt to cover all TMDs, our main interest lies in molybdenum and tungsten based semiconducting TMDs.

There are many methods for the synthesis of monolayer TMDs the simplest method is mechanical exfoliation from bulk [12, 13]. However, this method is random and not scalable. It has some limitations regarding shape, size, and problems during transfer procedure which can introduce some impurities and cracks. Also, the adhesion between the substrate and TMD layer is not good in exfoliated samples. These facts may impair the performance of TMDs based devices [14]. In contrast, the direct growth method has the advantage of providing better integration between the substrate and TMDs. This integration is essential for nanoelectronic devices.

Beyond mechanical exfoliation, chemical vapor deposition (CVD) is the second most common technique used to prepare TMDs layered materials. Usually, TMDs are synthesized at high temperatures above 800°C [15–17] on SiO₂, sapphire, and quartz substrates [18–20]. By changing the synthesis parameters e.g, temperature, precursor, atmospheric pressure, etc, we can grow different TMDs. There is no standard synthesis model which could be

followed, different growth methods are reported following different parameters by different groups around the world [21]. Hence a reliable and repeatable direct synthesis method is needed for each TMD synthesis. In this thesis, many key elements in the synthesis procedure e.g, the position of the substrate, shape of the ceramic boat, etc, generally not mentioned in the articles, but very important in growth procedure will be discussed in details. Moreover, the high temperatures synthesis of TMDs is a barrier to mass production. One route to reduce the fabrication cost is to decrease the synthesis temperature. Low-temperature synthesis of graphene, for example, became a useful addition in nanoelectronics [22–25]. These reports on graphene synthesis have shown great optical performances, avoids transfer defects, and has properties comparable to those of high temperature grown graphene [26, 27]. This encourages the researchers to move on to low temperature synthesis of TMDs. Very little is known about the synthesis of TMDs on glass because it cannot reach high-temperature. The transition temperature of flat glass is 564°C , so any recipe that works below this temperature will be useful in mass production and studying the transmission properties of TMDs. Also, tellurium assisted growth has able to decrease the synthesis temperature of TMDs [28]. Alkali metal salts are also known to be promoters in the growth of large area TMDs [29–31], but the knowledge about the low temperature synthesis using salts is limited. Recently, monolayers of MoS_2 were grown at high temperatures on soda-lime glass. The sodium from the substrate can act as a catalyst and increase the growth rate [32–34]. Based on the characteristic that sodium increases the chemical reaction's velocity, we propose a new synthesis route at low-temperature mediated by sodium at atmospheric pressure. This sodium mediated low-temperature synthesis technique has enabled us to achieve MoS_2 single crystals and polycrystals, on SiO_2 and glass substrates.

Atomically thin semiconducting TMDs (e.g MoS_2 , MoSe_2 , WS_2) have indirect bandgap in bulk form, while direct bandgap when thinned down to monolayer [35]. The transition from indirect to direct bandgap in monolayer TMDs give rise to strong photoluminescence [36,37]. Mak et al. have shown the variation of photoluminescence with the number of layers in MoS_2 sample [38]. Semiconducting TMDs show remarkable interaction with light, over a broad bandwidth ranging from infrared to ultraviolet wavelengths. Monolayer MoS_2 has an inter-band transition at the \mathbf{K} and \mathbf{K}' points in the first Brillouin zone (BZ), where strong spin-orbit interaction splits the valence band into two sub-bands [39]. This gives rise to two peaks in the optical absorption spectra of MoS_2 , identified as A (1.85 eV) and B (2 eV) excitons [11]. Considerable efforts have been made to study the absorption and transmission properties of these

materials [40–42].

Raman spectroscopy is the most powerful tool to characterize TMDs and other 2D materials, it can reveal information about the crystal and electronic structure, lattice vibrations and layer thickness. In general back-scattering Raman spectroscopy of semiconducting TMDs, exhibits two first-order Raman peaks, corresponding to the A_{1g} out-of-plane and the E_{2g} in-plane vibrational modes. Raman studies of single and few layers of MoS_2 [43, 44] and WS_2 [45] have shown that the frequency of E_{2g} mode decreases as the number of layers increases, whereas the frequency of A_{1g} mode increases. Such behaviour is due to increase in dielectric screening which reduces the long-range Coulomb interaction between the effective charges with increasing number of layers. Raman spectroscopy was also used to identify several defect-induced Raman scattering peaks in MoS_2 monolayer arising from zone-edge phonon modes [46]. The intensity of the defect peak is proportional to the density of defects, providing a practical route to quantify defects in monolayer MoS_2 using Raman spectroscopy. However, very little is known about the defects related Raman phenomena in other monolayer TMDs.

Beyond linear optics, nonlinear optical properties of TMDs, play a key role in understanding the nanoscale light-matter interactions, as well as the structure of layered TMDs [47]. Second harmonic generation (SHG) is the most studied nonlinear process in TMDs [48]. SHG of the bulk TMDs is under study for long [49]. However, soon after the discovery of 2D-TMDs the SHG in monolayer has increased drastically. The second order nonlinearity $\chi^{(2)}$ in monolayer TMDs was reported to be 10^3 times higher than the commercial nonlinear crystals (e.g, BBO, KTP, and LiNbO_3) [50–52]. This makes them more favourable for practical use in future non-linear optical devices. Monolayers of TMDs are non-centrosymmetric and, therefore, second harmonic generation (as well as a third-harmonic generation) has been observed in many TMDs [53–59]. The angular dependence of SHG in monolayer TMDs shows strong symmetry dependence on its crystal lattice structure. Hence, SHG microscopy can serve as a powerful tool to non-invasively determine the crystalline directions of TMDs monolayers. Recently, polarization-resolved SHG microscopy was used to calculate the twist angle in two stacked layers of WS_2 , by measuring the crystal orientation of each layer [60].

In the 2H phase, bilayers of TMDs present the so-called AA' interlayer stacking order, which is centrosymmetric and [61], therefore, does not allow for a second harmonic generation. In contrast, if we rotated two layers relative to each other, the centrosymmetry can be broken. Indeed, SHG in artificially stacked bilayers and heterostructures was reported before [62]. However, the

study of SHG in as-grown bilayers and heterostructures with different rotate angle is unknown. Here, we report the SHG from the CVD grown of two and three layers TMDs with different phase stacking between the top and bottom layers, i.e., 0° and 60° stacking. The second harmonic generating reveals that CVD grown bilayers could possess two types of phase stacking (i.e 2H and 3R).

Due to the direct bandgap present in monolayer TMDs, they are good candidates for digital electronic applications, which triggered the researchers to use these materials for optoelectronic devices. MoS_2 and WS_2 have proved to be a good field effect transistor with high electron mobility and charge transfer [63–72]. The highest carrier mobility yet reported is by Wei Chen et al. [33] is around $90 \text{ cm}^2\text{V}^{-1}\text{s}^{-1}$ with ON/OFF ratio of 10^7 . MoS_2 has proved to be a good photodetector from visible to infrared range with high photore-sponsivity [73–80]. The electrical performance of the device fabricated on the monolayer TMDs is directly related to the quality of the material. Hence, one can examine the quality of their grown TMDs by electrical measurements. The dependence of first-order Raman modes of MoS_2 on electron doping was also reported by B. Chakraborty et al, in the top gate field effect transistor (FET) device configuration [81]. They have shown the redshift of A_{1g} mode by applying the gate voltage in FET configuration and, simultaneously measuring the Raman spectra. Here, we have measured the dependence of Raman modes of CVD grown MoS_2/WS_2 heterostructure device with gate voltage.

This thesis is a pioneer work, on the synthesis and characterization of monolayer TMDs for our group. The main objective of this thesis was to develop reliable and repeatable methods for growing high-quality monolayer MoS_2 , WS_2 , and, their heterostructure by atmospheric pressure CVD system. We have grown MoS_2 single crystals and polycrystalline film at low temperatures. The low temperature synthesis is mediated by sodium which is the key element in relaxing the growth temperature. Secondly, exploring the optical properties of CVD grown TMDs by optical microscopy, atomic force microscopy, X-Ray photoelectron spectroscopy, Raman and Photoluminescence spectroscopies. We also report the CVD synthesis of two and three layers of MoS_2 and WS_2 with different phase stacking between the top and bottom layers, i.e., 0° and 60° stacking. The structure and stacking sequences of bi-layer TMDs was revealed by the SHG. The SHG shows 0° stacked bilayer has no inversion symmetry which refers to 3R(AB) and 60° has inversion symmetry (Centrosymmetric) and has 2H(AA') phase stacking. Finally, back gate FET devices were fabricated to investigate the electrical performances of our TMDs.

And the effect of electron doping (V_G) on the vibrational modes was studied by Raman spectroscopy.

The thesis structure is divided into six chapters. **Chapter 2** presents a brief explanation of TMDs, their crystalline and electronic structure. The stacking of two layers, Raman modes, direct and indirect bandgap in TMDs. The detailed explanations of materials, equipment, and CVD techniques used for the synthesis of TMDs. **Chapter 3** explains various techniques employed to characterize the CVD grown samples, including Raman spectroscopy, atomic force microscopy, second harmonic generation, device fabrication, and finally electrical measurements. The experimental setups of all the characterization techniques are explained in details. **Chapter 4** presents the characterizations of the CVD grown monolayer MoS_2 , WS_2 , and MoS_2/WS_2 by AFM, Raman, and PL spectroscopies are discussed. A detailed explanation of sodium mediated low temperature synthesis technique of MoS_2 monolayer triangles and films. The catalytic behavior of sodium in decreasing the synthesis temperature is explained by first principle calculations. **Chapter 5** presents the characterization of two and three layers of TMDs having different crystal orientations. Non-linear optical properties (second and third harmonic generation) of two and three layers MoS_2 , WS_2 , and MoS_2/WS_2 samples. **Chapter 6** presents the electrical measurements, transport and output curves of FETs devices fabricated on MoS_2 , WS_2 and MoS_2/WS_2 samples and the electro-Raman of MoS_2/WS_2 heterostructure device.

2

Properties of Transition Metal Dichalcogenides

This chapter includes a brief explanation of TMDs, their crystalline structure, and the stacking of two layers. Optical phonons and electronic structure of TMDs. Linear and Non-linear optical properties of TMDs. Basic concepts about Raman modes, direct and indirect bandgap.

2.1

Introduction to Transition Metal Dichalcogenides

Transition metal dichalcogenides have the chemical formula MX_2 , where M is a transition metal e.g, (Mo, W), and X is a chalcogen atom (S, Se, or Te). The transition metals have d electrons in the outermost shells which play an important role in determining their properties, as they form a covalent bond with the chalcogen atoms [82]. When the covalent bond is formed in TMDs, the transition metal shares its electron to the chalcogen atom, filling the valence shell that is responsible for the planar structure of the TMDs. The atoms in two dimensional TMDs are spacially arranged in an X—M—X structure, each transition metal atom is sandwiched between two chalcogen atoms [35]. Figure 2.1 shows a periodic table. When a transition metal atom [group IV (Ti, Zr, Hf), group V (V, Nb, Ta), or group VI (Mo, W)] forms a bond with chalcogen atoms [group XVI (S, Se, Te)] we call it transition metal dichalcogenide. Various permutations of these elements result in over 40 different compounds having different physical and chemical properties. Some of them are semiconductors, some are insulators, conductors, and superconductors also, although not all of them are layered solids [63,83,84]. The most important of them are Mo and W based dichalcogenides and its heterostructures because they are widely used in optoelectronic device applications [72].

In TMDs, a monolayer is defined as a plane of metal atoms structured hexagonally, sandwiched between two hexagonally ordered planes of chalcogen atoms, where the oxidation states of the metal and chalcogen elements are +4 and -2, respectively [85]. Layer by layer stacking of these monolayers forms the bulk. Its structure is similar to graphite and each layer has a thickness of $\sim 6 - 8 \text{ \AA}$, having strong covalent bonding within the plane and weak Van

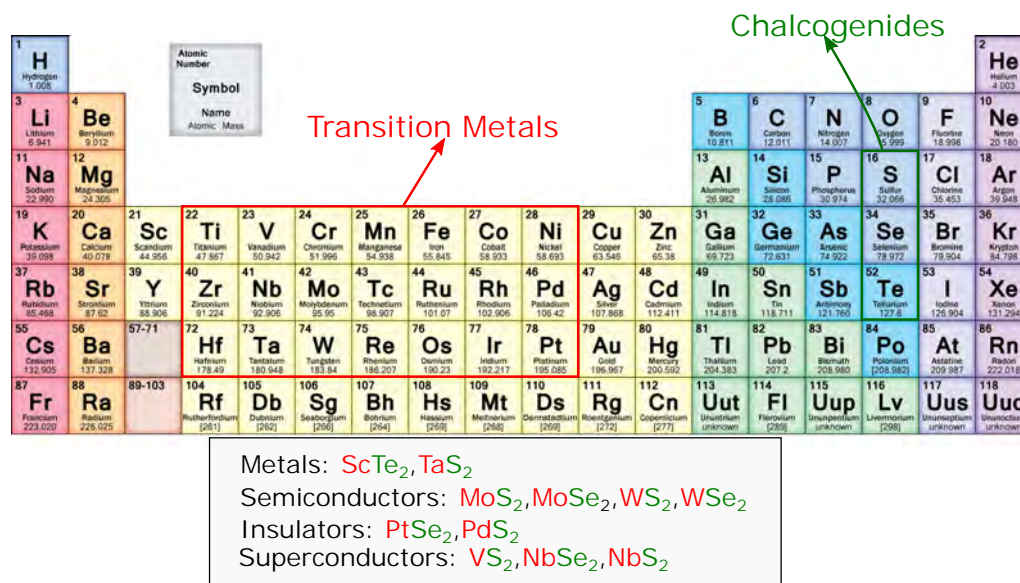


Figure 2.1: Periodic table and different TMDs.

der Waals interactions out of the plane. Bulk TMDs exhibit a wide variety of polymorphs and stacking prototypes because of the individual monolayer. The most commonly encountered polymorphs are 1T (trigonal prismatic), 2H (hexagonal), and 3R (rhombohedral), respectively, the digit indicates the number of X—M—X units in the unit cell, that is, the number of layers in the stacking sequence.

2.1.1

Structure of TMDs

Transition metal dichalcogenides (MX_2) differ significantly from classical 3-D counterparts. Individual layers of TMDs are weakly bonded to each other by Van der Waals forces, whereas within a single monolayer the metal and chalcogen atoms are covalently bonded. A monolayer in a TMD is an atomic trilayer structure, each layer of transition metal is sandwiched between two layers of chalcogen atoms (X—M—X) see figure 2.2(a). Each transition-metal atom is surrounded by six chalcogen atoms that coordinate in an octahedron or a triangular prism as shown in figure 2.2(b) [86]. TMDs like MX_2 ; (M = Ti, Zr, Hf; X = S, Se, Te) transition metal elements prefer the octahedral coordination because the strong ionic bonding results in the Coulomb repulsion between the inter-layer chalcogen atoms. On the other hand, semiconducting TMDs MX_2 ; (i.e; M = Mo, W, and X = S, Se) are generally found a in triangular prism, whose bonding has more covalent nature [87].

The three atomic layers (X—M—X) in semiconducting TMDs together

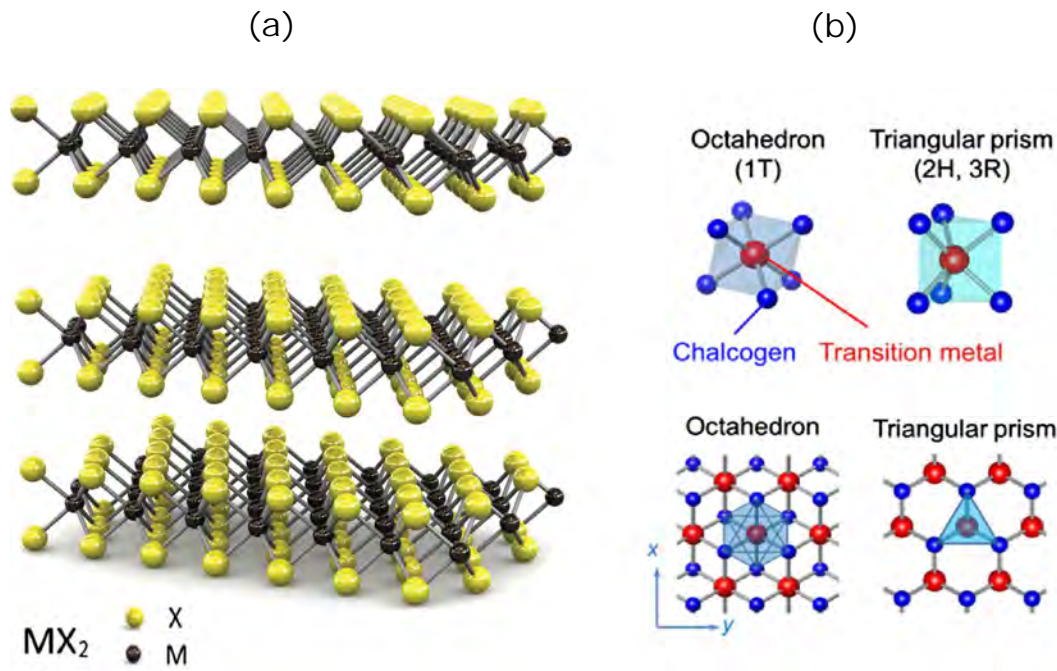


Figure 2.2: (a) 3D representation of the layered structure of transition metal dichalcogenides (TMDs). Adopted from [63]. (b) Archetypal coordination in TMDs. Octahedral coordination (left) triangular prismatic coordination (right) and top view of monolayers constructed from octahedral (left) and triangular prismatic (right) coordination. Adopted from [86].

form a 2D hexagonal lattice, with the A-sublattice being the metal atom per site and B-sublattice being the two chalcogen atoms per site. The hexagonal lattice has 3-fold symmetry or honeycomb structure like graphene and can allow inversion symmetry. For an even number of monolayers, the crystal structure has an inversion center, while for a perfect monolayer or any odd number of layers, the crystal does not have the inversion symmetry. Trigonal prism structure in 2H stacking type the unit cell contains two prisms of adjacent layers. The symmetry 2H- MX_2 belongs to the space group (D_{6h}) [88]. The space group for a single layer is (D_{3h}) due to the lack of translational symmetry along the z-axis. Similarly, for a few-layer system with even numbers of layers belong to the space group D_{6h} (with inversion symmetry), and systems with odd numbers of layers to the D_{3h} space group (without inversion symmetry) [89, 90].

2.1.2 Stacking Sequences of Two Layers

Since the two layers of a TMDs are bound together via weak Van der Waals attractions, this allows the layers to be stacked with different orienta-

tions and can break the inversion symmetry [62]. Two layers of semiconducting (Trigonal prism) TMDs can possess two types of phase stacking 2H/AA' and 3R/AB phase stacking [88,91,92]. Monolayer has an identical structure in 2H and 3R phases, the difference lies in the stacking order of the monolayers in the layered structures. The 2H phase of the bulk crystal has the hexagonal symmetry, having two monolayers per repeat unit, whereas the 3R phase has the rhombohedral symmetry, having three layers per repeat unit. First-principles calculations show that the bilayer in 2H stacking is more stable than the 3R stacking [93]. In 2H/AA' phase stacking M atom of first layer sits precisely on top of X atom of the second layer and shows inversion symmetry, while in 3R/AB phase stacking M atom is staggered a little from X atom of the other layer (no-inversion symmetry) see figure 2.3 [88,94].

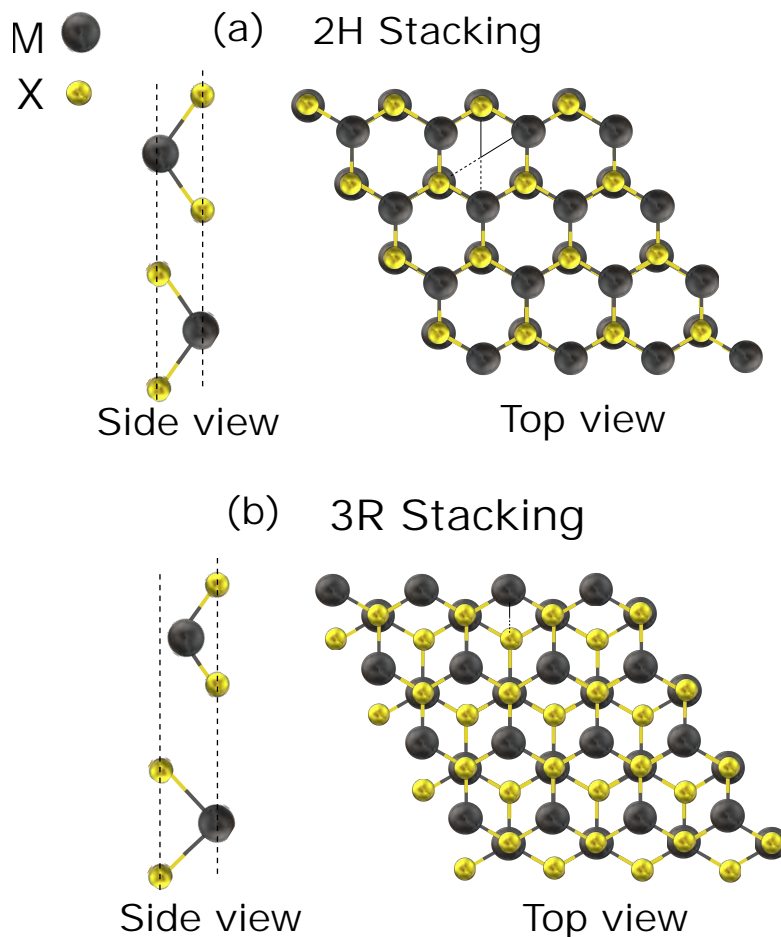


Figure 2.3: Side and top views of (a) 2H stacking pattern of bilayer MX₂, 2H is the most stable stacking pattern (also named as AA' stacking)(b) 3R (also named as AB stacking)

This stacking can also be used to control TMDs based device functionalities due to the effect of stacking on the electronic band structure, valley polarization, and nonlinear optical properties [62,93,95].

2.2 Phonon Dispersion

From solid-state physics, we know that a usual semiconductor TMDs has a parabolic energy dispersion for electron and holes, and its joint density of state near the bandgap is a step function. The phonon dispersion relations of monolayer MoS₂ and WS₂ as calculated by A.Molina, et al. by density functional theory and is shown in figure 2.4 [90]. The vibrational modes are dispersive with respect to wave vector \mathbf{q} . The phonon dispersion has three acoustic and six optical branches derived from the nine vibrational modes at the Γ point.

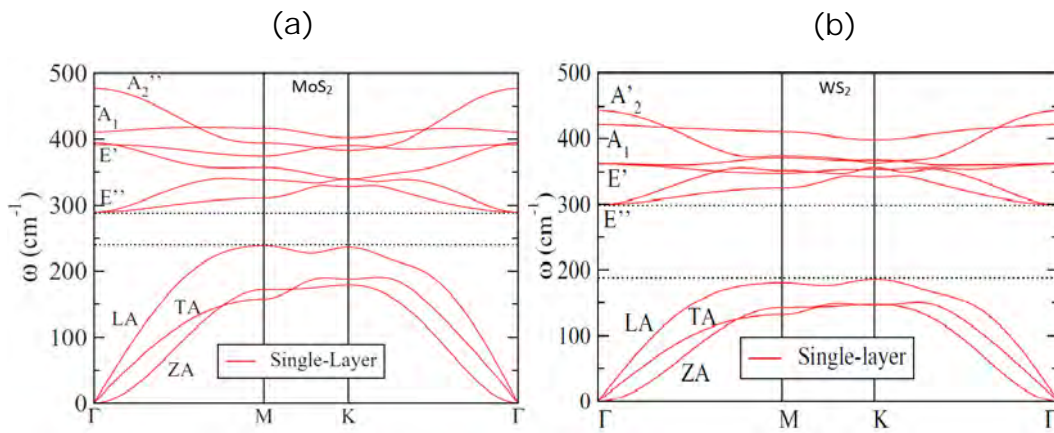


Figure 2.4: (a) Phonon dispersion curve of monolayer MoS₂ calculated by A.Molina, et al. [90]. (b) and WS₂.

The three acoustic branches are the in-plane longitudinal acoustic (LA) and transverse acoustic (TA), and the out-of-plane acoustic modes (ZA). The in-plane (LA and TA) have a linear dispersion and have higher energy than (ZA). The six optical branches are two out-of-plane transverse optical (TO₁, TO₂), two in-plane longitudinal optical (LO₁, LO₂), and two out-of-plane optical (ZO₁, ZO₂) branches. These six optical modes at the Γ point correspond to the irreducible representations E'' (LO₁ and TO₁), E' (LO₂ and TO₂), A₂' (ZO₁) and A₁' (ZO₂) see figure 2.4. Because, MX₂ compounds are slightly polar materials, certain IR-active phonon modes (e.g., E') show LO–TO splitting because of the coupling of the lattice to the macroscopic electric field created by the relative displacement of M and X atoms in the long-wavelength limit [90, 96]. There is also a bandgap between optical and acoustic branches, of $\sim 100 \text{ cm}^{-1}$ for MoS₂ and $\sim 30 \text{ cm}^{-1}$ for WS₂ [97–99].

2.3

Electronic Dispersion

Looking from the top, the crystal structure of TMDs monolayer is a honeycomb lattice (figure 2.2(b)) similar to that of the graphene. In contrast to graphene, the A and B sublattices are occupied by different atoms. This has an immediate consequence in the electronic structure, lifting the degeneracy in the electronic structure at the $\mathbf{K}(\mathbf{K}')$ point in the first BZ. Degeneracy is responsible for the Dirac cone dispersion relation in graphene. In contrast, in monolayer MoS_2 , a substantial energy gap is present. As the projection in the plane exhibits a hexagonal crystal structure similar to graphene, the edge terminations of a MoS_2 sheet can be zigzag, armchair, chiral, or a mixture of these types. The lift of the degeneracy at $\mathbf{K}(\mathbf{K}')$ points in the first BZ creates a desirable bandgap in TMDs. The electronic band structure of TMDs depends on the transition metal and chalcogen atoms, thickness, and stacking sequence of each layer [100]. Electronic structure calculations have been playing an important role in understanding the physical properties of monolayer TMDs.

The electronic structure near the bandgap has the main contribution from d_{z^2} (out-of-plane) and $d_{x^2-y^2}$ and d_{xy} (in-plane) orbitals of transition metal (M) atoms and p_z orbitals of chalcogenide (X) atoms [101]. The direct bandgap in MX_2 (TMDs) depends on the localized d-orbital of the transition metal (M) atom, which is not much affected by the inter-layer coupling due to its location in the unit cell. The indirect bandgap in MX_2 (TMDs) depends on the overlap between the d orbital of a transition metal (M) and the p_z orbital of chalcogenide atoms, which strongly depends on the interlayer coupling. Hence, as the number of layers is decreased, the intrinsic direct bandgap of the material becomes more prominent [102].

Figure 2.5(a,b) show the band structure of MoS_2 monolayer and bulk and indicates the direct and indirect bandgaps, calculated by O. Yazyev et al. using density functional theory (DFT) within the generalized gradient approximation (GGA) [103]. Schematic illustration of the band structure of MoS_2 is shown in figure 2.5(c,d). Theoretical value of the bandgap of bulk MoS_2 is 0.88 eV obtained using DFT-GGA, with the valence band maximum (VBM) at the Γ point in the Brillouin zone and the conduction band minimum (CBM) along the Γ - \mathbf{K} direction. VBM and CBM are indicated by red and blue circles in figure 2.5. The experimentally observed bandgap of bulk MoS_2 is ~ 1.3 eV [38]. As the number of layers decreases, the valence band maxima, and conduction band minima shift towards \mathbf{K} due to quantum confinement, making it a direct bandgap semiconductor at the monolayer. Also, by decreasing the number of layers, the bandgap shifts upward in energy. That is attributed to the quantum

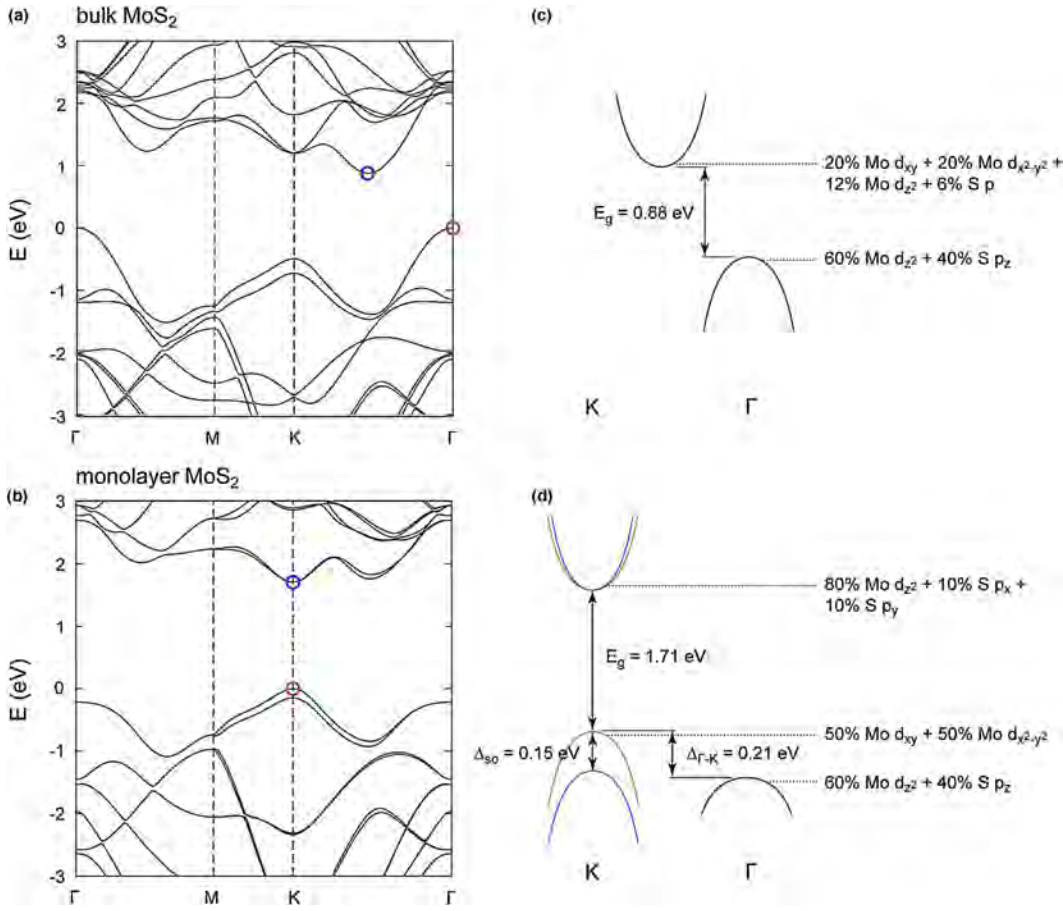


Figure 2.5: Electronic band structures of (a) bulk MoS₂ and, (b) monolayer MoS₂ calculated from first principles using DFT–GGA approach. Valence band maxima and conduction band minima are indicated by red and blue circles, respectively. Energies are given relative to the VBM. Schematic drawings of low-energy bands in (c) bulk MoS₂ and (d) monolayer MoS₂ showing the band gaps E_g , as well as the valence band spin–orbit splitting Δ_{so} and the Γ valley band offset $\Delta_{\Gamma-K}$ for the case of monolayer MoS₂. The band structure was adopted from [103].

confinement of charge carriers which is common in nanosystems [104,105]. The bandgap obtained from DFT–GGA calculations for monolayer MoS₂ is 1.71 eV, while its experimentally observed value is ~ 1.85 eV.

The transition from indirect to direct bandgap exhibits strong photoluminescence increase in order of ($\times 10^4$) as compared to bulk that is attributed to the fact that the electron is no longer passing through the intermediate state and transition occurs directly. This indirect to direct bandgap transition was confirmed by photoluminescence experiments, where the authors observed a shift of the indirect PL peak with the number of layers and enhancement of the PL signal in monolayer compared to the few-layers and bulk [11, 38].

2.4 Linear Optical Spectroscopy

The study of the interaction between electromagnetic radiation (light) and matter is known as optical spectroscopy. The standard setup for linear optical spectroscopy consists of a light source, the sample under consideration, a spectrometer to disperse the light, a detection unit and a computer to collect and plot the data. Linear optical spectroscopy includes reflection, transmission, and luminescence spectroscopy. Other techniques include photoluminescence spectroscopy and measurements of the luminescence yield or Raman spectroscopy. Simple linear methods such as linear absorption and photoluminescence spectroscopy were being practised for qualitative and quantitative analysis of TMD materials much prior to the existence of the laser.

Upon interacting with light, electrons in the TMDs can be excited from the valence band to the conduction band. In the relaxation process, the excited electrons will decay to the ground states with subsequent emission of light called photoluminescence. Monolayer TMDs (e.g MoS₂ and WS₂), are direct bandgap semiconductors with PL emission in the visible to near-infrared range. Although they are atomically thin (few nanometers), they give strong interaction with light.

Now, consider the light (photons) interacts with a TMD material if the lattice vibrations (phonons) are also involved in the optical transitions. The generated photon can have lower/higher energy than the incident photon, and the energy difference is related to a specific phonon mode. This inelastic light scattering phenomenon is known as Raman scattering. Raman scattering is very rare compared to elastic scattering (Rayleigh scattering), approximately one in a million photons have inelastic scattering and have a difference in energy. This is attributed to the energy absorption by the atoms or molecules and the energy difference is related to the chemical structure of the molecule responsible for the spread. Raman spectroscopy has become one of the most powerful tool for analyzing the electrons, phonons and their coupling in TMDs [106]. It provides us a chemical fingerprint of the substance.

2.4.1 Photoluminescence in TMDs

Figure 2.6, shows the absorption and photoluminescence spectra of different TMDs, adopted from [107]. The absorption and PL spectra of TMDs are co-related, for MoSe₂ (WSe₂), the absorption peak at a wavelength of 800 nm (750 nm) corresponds well with the PL peak at this wavelength. In contrast, for MoS₂ (WS₂), the absorption and PL peaks are shifted. This

shift in peak position is attributed to the inhomogeneity of the dielectric environment, which affects the surface interaction of monolayer MoS₂ (WS₂) and changes the binding energy of the excitons. An exciton is a hydrogen-like complex consists of a bounded electron-hole pair. Exciton is formed by the Coulomb attraction between two oppositely charged quasiparticles. It is an electrically neutral quasiparticle that exists in insulators, semiconductors, and some liquids. It is regarded as an elementary excitation of condensed matter that can transport energy without transporting the net electric charge. A monolayer of MoS₂ can absorb 10% of incident light with energy above the bandgap [108].

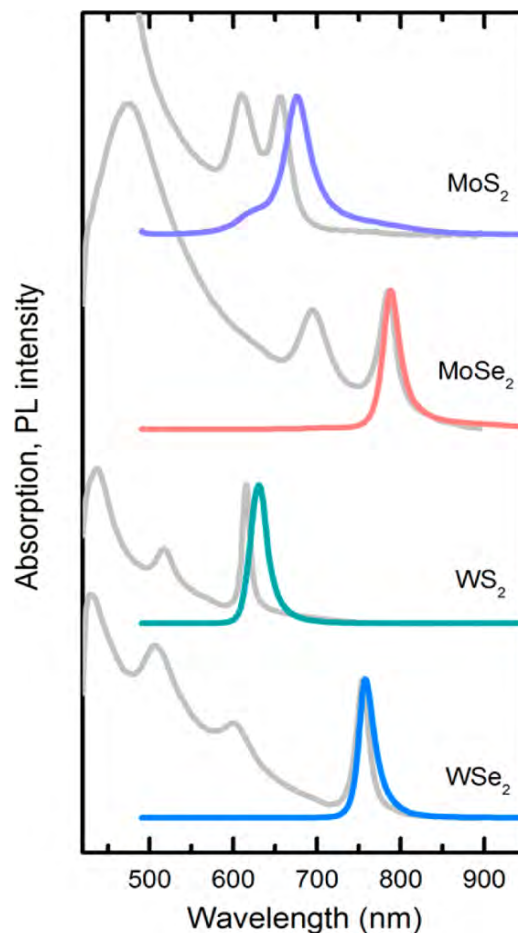


Figure 2.6: Absorption (gray lines) and PL (color lines) spectra of monolayer semiconducting TMDs crystals (MoS₂, MoSe₂, WS₂, WSe₂). Measurements were made on layers produced by mechanical exfoliation of bulk crystals. The photoluminescence peak coincides with the bandgap exciton absorption peak. Adopted from [107].

In TMDs, the PL is influenced by many factors including the number of layers, strain, and interfacial interactions such as charge transfer, photonic nanostructures, etc. As already mentioned, these materials have bandgaps

that vary depending on the number of layers [38]. The monolayers are direct bandgap semiconductors with the range of ~ 650 nm to 1750 nm. The direct transition of electrons without any change in moment makes them good candidates for light emitting devices. The PL spectrum of monolayer TMDs is characterized by two distinctive peaks, which are attributed to the excitonic transitions at the \mathbf{K} (or \mathbf{K}') valley, and are labeled A (lowest energy) and B (highest energy). In the case of MoS_2 , the experimental values found for these energy transitions are $\sim 1.8 - 1.9$ eV (A exciton) and ~ 2 eV (B exciton), as can be seen in figure 2.6. These two peaks in (figure 2.6), are due to a strong excitonic effect in these TMD materials. The separation of A and B excitons come from the spin-orbit splitting of the top of the valence band at the \mathbf{K} point from $d_{x^2-y^2}$ and d_{xy} orbitals to d_{z^2} orbital [109].

The transient absorption spectroscopy has observed intervalley bi-excitons in monolayer MoS_2 , which is the interactions between two excitons and result in the formation of bound quasiparticles [110]. In Van der Waals heterostructures and doped TMDs trions are also observed, which are formed by excitons excited in the one TMD layer and electrons transferred from the other layer [111].

The optical properties of these TMDs also vary according to the polarization. For example, Cao et al. study the absorption and PL of MoS_2 in circularly polarized light [112]. They studied the MoS_2 samples with different number of layers and showed that if PL is excited with circularly polarized light, the luminescence of the material also has substantial circular polarization. First principle calculations also showed that monolayer MoS_2 is an ideal material for valleytronics [113]. The PL spectrum is also temperature dependent [114]. At low temperatures, the excitonic features can be easily resolved from one another and their intensities are usually higher than in room temperature measurements. The PL spectrum is also influenced by electron doping [115], as demonstrated by A.K. Newaz et al. both PL intensity and absorption can be controlled by gate voltage in monolayer MoS_2 . Such behavior is due to the interaction of excitons with the charge carriers [116].

2.4.2

Raman Modes in TMDs

The general back-scattering, Raman spectroscopy of 2H-MX_2 exhibits two first-order Raman peaks, corresponding to the A_{1g} out-of-plane and the E_{2g} in-plane vibrational modes. The first-order Raman band arises from a single phonon at the center of Brillouin zone while the second-order Raman band arises from multiple two-phonon processes across the whole Brillouin zone. In

case of a monolayer of 1H-MX₂, it has three zone-centre and belongs to the space group D_{3h}. Irreducible representations of this point group shows A₁' and E' first-order Raman active modes, which corresponds to the out-of-plane A_{1g} and in-plane E_{2g} of 2H-MX₂ (space group D_{6h}) [117, 118]. In A₁' phonon mode the transition metal (M) atom does not move while chalcogenide (X) atoms vibrates in the out of plane direction. In E' phonon mode chalcogenide atoms vibrate in-phase while, the transition metal atom vibrates in-phase but in an opposite direction to chalcogenide atoms, see figure 2.7(a).

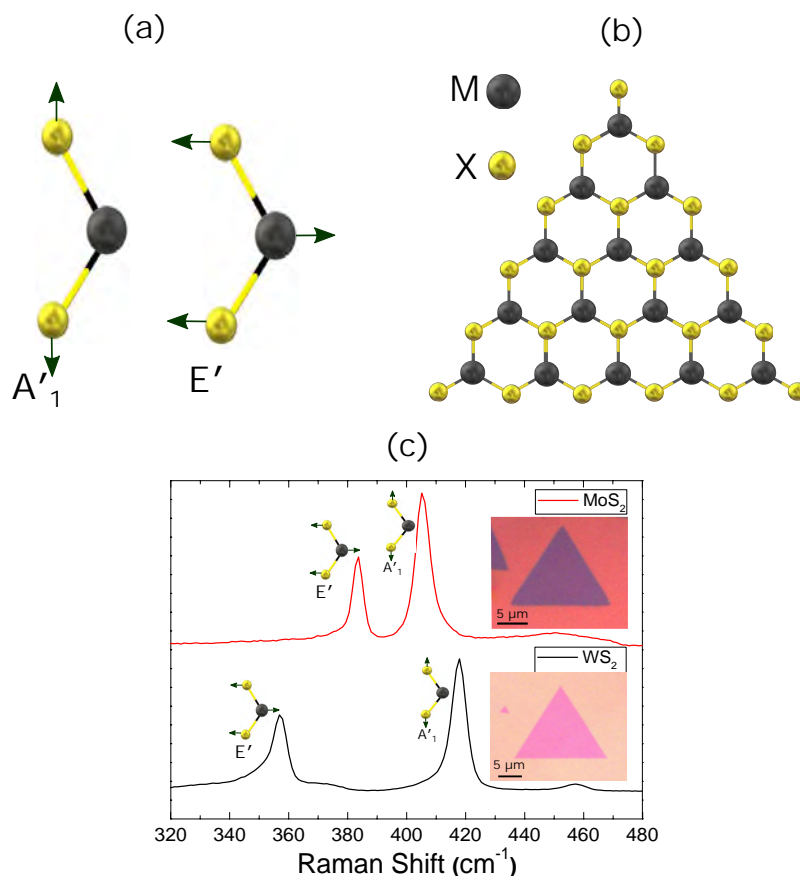


Figure 2.7: (a) Raman active modes of monolayer TMDs. (b) Schematics of triangular shape TMDs, the grey atom is a transition metal and yellow is the chalcogen. (c) Raman spectra of MoS₂ and WS₂ showing vibrational modes inset are their triangular structure.

Figure 2.7(c) shows the Raman spectra taken from WS₂ and MoS₂ monolayer using a 473 nm wavelength excitation laser. This shows only two Raman active modes corresponding to E' and A₁'. The optical images (inset) of WS₂ and MoS₂ monolayer show the triangular structure. Generally, MoS₂ and WS₂ monolayer grow in triangular shape in CVD process. As all shapes of domains start growing from a hexagonal nucleus, but in sulphur rich atmosphere it always terminates with sulphur atom [119, 120]. The schematic

of triangular shape TMD is shown in figure 2.7(b), the triangular shape is only possible with the edge atom being sulphur.

2.5 Non-Linear Optical Spectroscopy

During light-matter interaction, the presence of intense fields can cause non-linear generation of new frequencies. The nonlinear effects occurs either due to intensity dependence of refractive index of the nonlinear medium or due to inelastic-scattering phenomenon. While nonlinear medium are the medium in which the dielectric polarization (P) responds nonlinearly to the Electric field (E) of the light. The study of non-linear optical spectroscopy such as second harmonic generation and third harmonic generation (THG), has been widely reported in TMDs and other 2D materials, such as graphene, black phosphorus, hBN, etc [121]. TMDs with broken inversion symmetry can give rise to SHG (a non-linear optical effects). This phenomenon occurs due to the presence of a non-linear response in the material, it is largely used to characterize these materials. SHG is the most studied nonlinear effect in TMDs. In addition, the SHG can be used in photonic devices such as modulators, frequency converters, and in the production of new frequency lasers.

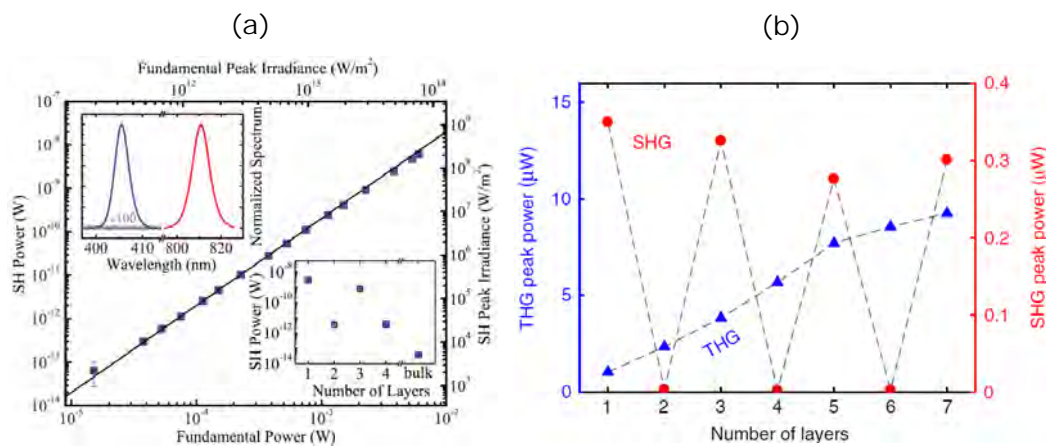


Figure 2.8: SHG characteristics from MoS₂ (a) Power dependence of SHG from a monolayer MoS₂, the upper inset shows the fundamental spectra (red) and the SHG (blue). The lower inset shows the layer-dependent intensity of the SHG. Adopted from [52]. (b) SHG and THG intensities as functions of the number of layers. Adopted from [122].

Figure 2.8(a) shows an example of SHG of an 810 nm Ti:sapphire laser pulse, from monolayer MoS₂ and its dependence on the power and layer number [52]. A. Säynätjoki et al. studied the layer-dependent SHG in exfoliated MoS₂ [122]. They observed SHG only in odd-layers and SHG vanished at even-

layers see figure 2.8(b). This is due to the fact, that the inversion symmetry is restored for even-layers of 2H-stacking TMDs.

Hsu et al. demonstrated the SHG in artificially stacked layers of TMDs with arbitrary angles [62]. They found that the SHG of artificially stacked bilayers is the coherent superposition of SHG fields of the individual monolayers, with a phase difference depending on the stacking angle. The interference mainly depends on the twisted angle but not the material constituent, which makes SHG as a sensitive method to examine the bilayer crystal orientation. Yu et al. demonstrated charge induced SHG in bilayer WSe₂ [123]. They use the back gate FET configuration, by applying gate voltage the charge was accumulated in transition metal planes within the layer. The accumulation of the charge leads to a nonuniform electric distribution due to the screening effects. As a result, the inversion symmetry was broken and SHG was enhanced.

Third harmonic generation (THG) and four-wave mixing (FWM) are other nonlinear optical processes that originated from the third-order susceptibility $\chi^{(3)}$. THG has been widely investigated in many TMDs [47, 124]. In-contrast to SHG, THG does not require the absence of the inversion symmetry and can be observed both in odd and even-layers. As can be seen in figure 2.8(b), THG signal intensity monotonically increases with the number of layers. Saturable absorption is another third-order nonlinear process and attributed to the imaginary part of $\chi^{(3)}$. TMDs are also being used as a saturable absorber. For example MoS₂ shows high transmission and low non-saturable loss making it a potential candidate for application in mode-locked solid state lasers [18].

2.6 Photoelectron Spectroscopy

Photoelectron spectroscopy is the measurement of electrons energy (emitted due to the photoelectric effect) when high energy electromagnetic radiation interacts with matter. Photoelectron spectroscopy is the most direct method of investigating electronic structure. The orbital structure of a molecule is reflected in the band structure of a photoelectron spectrum. The two main types of photoelectron spectroscopy are X-ray photoelectron spectroscopy and ultraviolet photoelectron spectroscopy. These spectroscopies depends on whether the ionization energy is provided by the X-ray photons or ultraviolet photons. Regardless of the incident photon beam, all photoelectron spectroscopies revolves around the general theme of surface analysis by measuring the ejected electrons.

The best way of measuring the stoichiometry of TMDs is by X-ray

photoelectron spectroscopy (XPS). XPS was employed to analyse the chemical compositions of the doped 2D-TMDs alloys like $\text{Mo}_{1-x}\text{W}_x\text{S}_2$ [125], $\text{WS}_{2(1-x)}\text{Se}_2$ [126], and $\text{Mo}_{1-x}\text{W}_x\text{Se}_2$ [127]. By studying the core level binding energies of S2p, Mo3d, and W4f peak intensities they have estimated the doping levels in the TMDs alloys. Just like Raman and PL spectroscopies the XPS has shown layer dependent shift in MoS_2 thin films [128]. The binding energy shifts downward ~ 0.2 eV as the film thickness increases from 3 to 10 layers. The XPS has also proved a reliable tool in studying the structural defects in CVD grown MoS_2 [129].

3 Experimental Methodology

This chapter includes a detailed explanation of atmospheric pressure chemical vapor deposition process used for the synthesis of TMDs. Various techniques employed to characterize the grown samples, including Raman spectroscopy, photoluminescence, atomic force microscopy, X-ray photoelectron spectroscopy, second harmonic generation, device fabrication, and electrical measurements. The experimental setups of all the characterization techniques are explained in detail.

3.1 Chemical Vapor Deposition

Chemical vapor deposition is a process used in the semiconductor industry for depositing high quality and high performance solid thin films on wafers substrates. In a typical CVD process, the substrate is exposed to one or more volatile precursor gasses, which form a solid layer by either reacting with or decomposing on the surface. The substrate surface is heated and chemical reaction occurs in vapor form and finally, a solid material is deposited on the substrate. By using a CVD process it is possible to deposit amorphous, polycrystalline epitaxial thin films or a single crystalline film on a wafer surface. There are many kinds of CVD processes, ranging from low pressure to atmospheric pressure to plasma-enhanced deposition.

In 2009, Xuesong Li et al. [130] reported a breakthrough in the growth of single layer graphene by CVD. In 2012, Yi-Hsien Lee et al. [17] synthesized large-area single layer MoS₂ for the first time by CVD on SiO₂/Si substrates. Nowadays CVD plays a vital role in the synthesis of Carbon nanotubes [131], Boron Nitride nanostructures [132], Graphene [130], and many 2D-TMDs [15–18,20,28]. For graphene synthesis, it requires a metallic catalytic substrate, such as Copper or Nickle with a growth process occurring at a temperature of $\sim 1100^\circ\text{C}$ [130,133]. But, for the synthesis of atomically thin semiconducting TMDs, it can be grown directly on SiO₂/Si, quartz, or sapphire substrate, at a temperature $\sim 800\text{-}900^\circ\text{C}$ [15–18,20,28,134–138].

In this thesis, we have used the atmospheric pressure chemical vapor deposition (APCVD) system to synthesize MoS₂, WS₂, and their heterostruc-

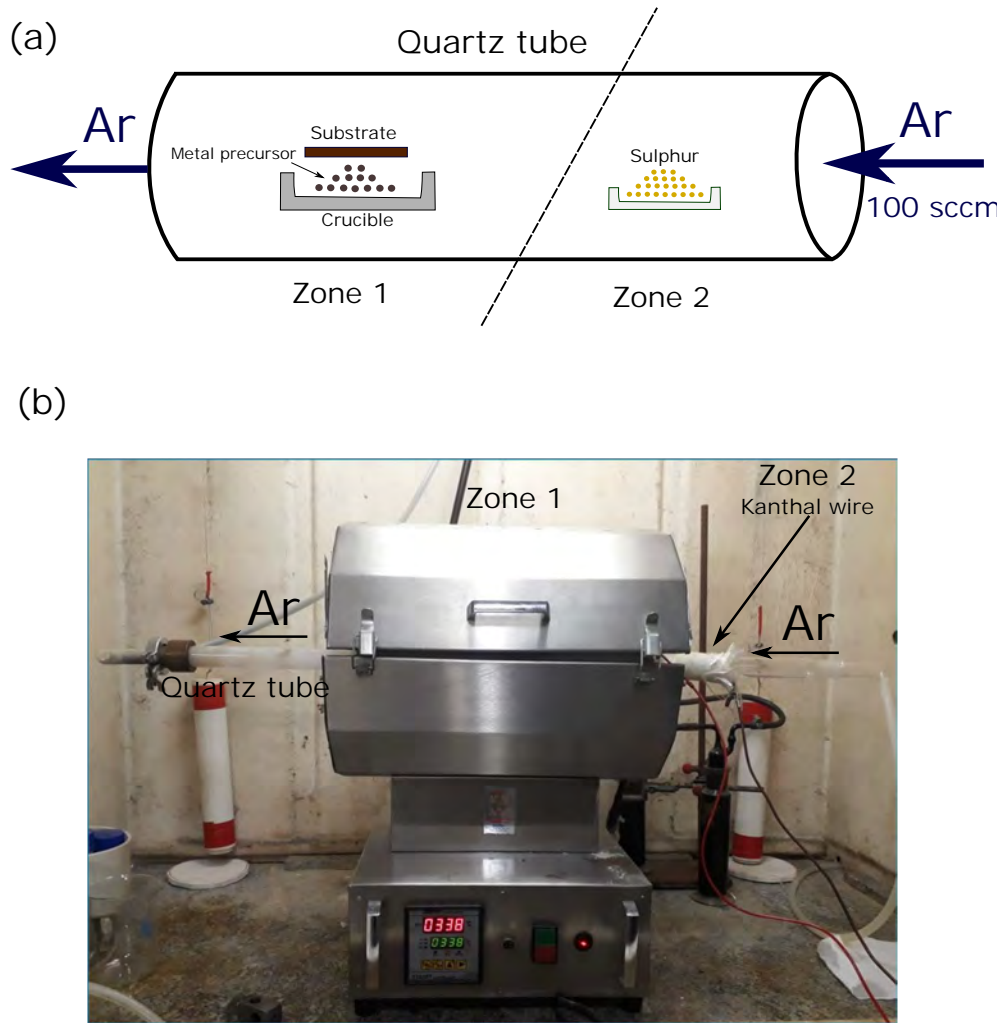


Figure 3.1: (a) Schematic diagram for the CVD synthesis of TMDs inside a quartz tube, showing the crucibles, and the substrate, two zones are heated independently at different temperatures. (b) CVD system at Protective Coatings and Nanostructured Materials Laboratory vandegraaff PUC-Rio.

tures. Figure 3.1(a) gives the schematic representation of CVD synthesis. The growth process is carried out inside a quartz tube in a dual-zone tubular furnace. Figure 3.1(b) shows a real tubular furnace (CVD), that we have at vandegraaff laboratory (PUC-Rio). However, this is not a dual zone furnace and we are manually heating zone 2 by wrapping a Kanthal wire around the quartz tube. Kanthal is an iron-chromium-aluminium alloy which is used in a wide range of resistance and high-temperature applications. By applying ~ 3.5 A current to Kanthal wire we can reach to $\sim 350^\circ\text{C}$.

3.1.1

Preparation of the Substrate

The preparation of a clean substrate is very important before the growth procedure. First of all, the substrate should be immersed in acetone and ultrasonicate for 15-20 minutes, then ultrasonicate again for 15 minutes in isopropyl alcohol. Finally, wash it with distilled water. It's better to avoid drying substrate with air blows because it will let small dirt particles stick on the substrate resulting in the growth of dirty samples. When the substrate is clean, water will automatically slip from the substrate, but if necessary use N_2 or Ar blow instead of air and avoid any stain on the substrate.

3.1.2

Precursors and Crucible

Precursor molecules are the molecules containing the element or elements which are the main source for the deposition of the film in the CVD process. In our synthesis we have used MoO_3 (Sigma-Aldrich, 99.97% pure), WO_3 (Sigma-Aldrich, 99.99 % pure), Tellurium powder (Sigma-Aldrich, 99.997 % trace metals basis), and Sulphur fine powder (99.5% pure) as precursor materials. The amount of the precursors depends on which TMD you are growing and on which substrate. The precursor's ratio, temperature, and substrate position are given in table 3.1 for every TMDs.

Crucible is a ceramic container in which metals or other substances may be melted or subjected to very high temperatures. We have used rectangular shape alumina crucible that can easily fit inside the quartz tube. Quartz crucible can also be used, but in our experience alumina crucible is more favourable, having high melting point ($\sim 2100^\circ C$). The precursor powders are loaded in the crucible and substrate is placed on the crucible. Figure 3.2(a) shows an alumina crucible and three different positions, showing how the substrate could be placed. The substrate's position is significant and depending on the TMD we are growing. For example, to grow monolayer MoS_2 the substrate is placed on top of the crucible, while for MoS_2/WS_2 heterostructure the substrate should be placed in an incline position.

3.1.3

Growth Process

Place two crucibles inside the quartz tube one loaded with the metal-oxide powder and the other with sulphur powder. Then place the quartz tube, in dual zone tubular furnace in a way that metal-oxide powder and the substrate is in zone 1 and sulphur in zone 2, see figure 3.1. The distance between

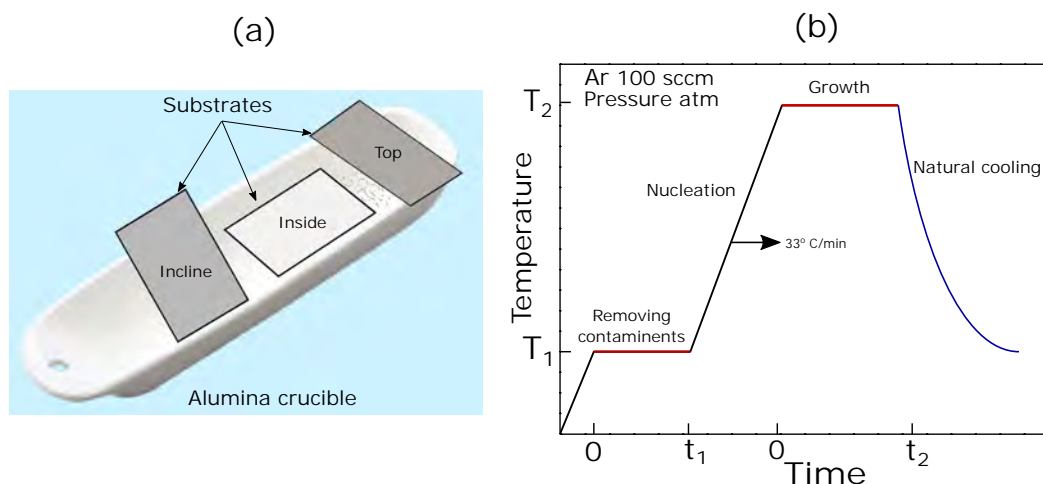


Figure 3.2: (a) Alumina crucible showing three different positions of the substrate. In every position substrate is facing downwards. (b) Temperature profile of the growth procedure, Ar flow rate is 100 sccm during the whole process.

the two crucibles is ~ 25 cm. Use the Argon flow rate at 100 sccm inside the quartz tube. During synthesis, first, heat the reaction chamber to 200°C (T_1) in an Ar environment, and leave there for 20 min (t_1). This will remove oxygen and other possible sources of contamination from the air. Now, heat the furnace independently at the rate of $33^\circ\text{C}/\text{min}$ until reaches T_2 (depending on which TMD you are growing) for zone 1, and 250°C for zone 2 (containing sulphur) at the same time. Then the materials will be kept under their respective constant temperatures for the next 15-25 min (t_2) (depending on which TMD you are growing). Finally, let the furnace to cool down naturally. The furnace will take 2-3 hr to cool down, avoid the artificial way of cooling, or opening the furnace until temperature drops to 300°C otherwise, it will result in cracked samples. The flow rate of Ar should be kept constant at 100 sccm during the whole growth process. Argon protects the system from oxygen and carries sulfur vapor from the upstream of the tube during the reaction, which causes it to react with the metal precursor and hence required samples are grown on the substrate. Figure 3.2(b) indicates the temperature profile of the growth procedure showing the ramp and two steps where the temperature should be kept constant.

Take an example of monolayer MoS_2 , we need 5-6 mg of MoO_3 as a precursor material. The precursor powder is loaded in the crucible and the substrate is placed right on top of the precursor powder facing downwards. The growth temperature (T_2) and growth time (t_2) is 850°C and 15 min.

3.1.4

Synthesis of Bilayers MoS₂, WS₂, and MoS₂/WS₂ Vertical Heterostructures

The faster rate of precursor sulfurization would increase the growth rate and results in bilayer samples. One way of increasing the growth rate is the addition of tellurium. The addition of tellurium enables the growth of extra-large MoS₂ triangles with multiple layers [28,139]. Here tellurium is a catalyst it does not change the composition of MoS₂, it is removed by the Ar. To grow bilayer MoS₂, 5 mg of MoO₃ should be mixed with 15 mg of tellurium powder. Temperature (T₂) and growth time (t₂) will be 850°C and 15 min.

To grow bilayers WS₂, relatively high amount (10-12 mg) WO₃ should be used. Here, the substrate position is significant. The substrate should be placed inside the crucible as close as possible to the powder. The growth temperature (T₂) is 900°C and growth time (t₂) is 20 min for bilayers WS₂. Controlling the bilayer is still challenging and it keeps growing multiple layers and layers with different stacking orientations. However, using the preceding steps we can achieve good bilayer crystals on the substrate.

To grow MoS₂/WS₂ vertical heterostructure the precursor powders MoO₃, WO₃, and Te should be mixed in a mortar pestle in the ratio of 1:1:3. The substrate position is inclined in this case. T₁ is 200°C for 20 min (t₁) and is the same for every synthesis, while the temperature (T₂) and growth time (t₂) is 850°C and 15 min. Figure 3.3 shows the optical images of some TMDs grown by CVD, on SiO₂/Si and quartz substrate. Table 3.1 shows a summary of the growth parameters for each TMDs. The best substrate positions are mentioned after many trials. For example if we put substrate inside the crucible while growing MoS₂ it will result in dirty sample, if we put substrate on top position while growing WS₂ growth will not happen.

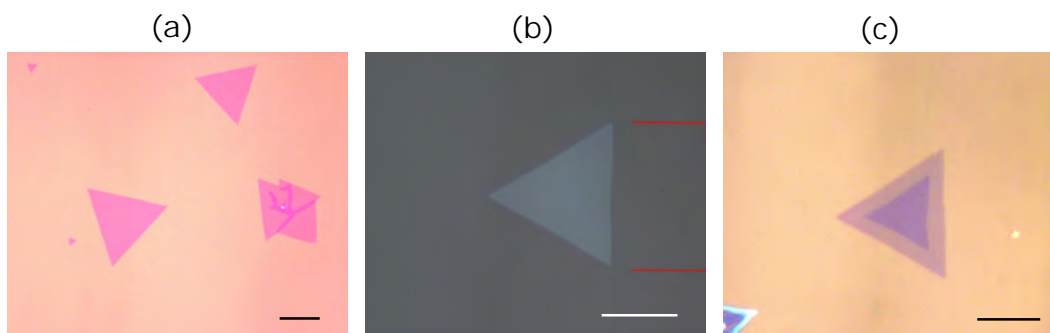


Figure 3.3: Optical images of some CVD grown TMDs. (a) WS₂ monolayer on SiO₂/Si 300 nm. (b) WS₂ monolayer on quartz. (c) Bilayer MoS₂ on SiO₂/Si 300 nm. Scale bars are 10 μm

Samples	Precursors	Ratio	Temperature (T ₂)	Time (t ₂)	Substrate position
Monolayer MoS ₂	MoO ₃	-	800-850°C	15 min	Top
Monolayer WS ₂	WO ₃	-	850°C	17 min	Incline
Bilayer MoS ₂	MoO ₃ +Te	1:3	850°C	15 min	Top
Bilayer WS ₂	WO ₃	-	900°C	20 min	Inside
MoS ₂ /WS ₂	MoO ₃ +WO ₃ +Te	1:1:3	850°C	15 min	Incline

Table 3.1: Growth parameters for different TMDs. In all synthesis powder is placed into the boat with the substrate facing down.

3.2

Optical Microscope

An optical microscope uses visible light and a combination of lenses to see the magnified images of small objects. It allows us to see the objects which are too small for naked eyes, such as cells. The working of an optical microscope is very simple, it consists of a light source and a series of lenses see figure 3.4(a). Light is focused on the specimen by condenser lens then it enters the objective lens where it is magnified to produce a real image. The real image is then magnified again by the ocular lens to produce a virtual image that can be seen by eyes.

ZEISS Axio Scope. A1 (figure 3.4(b)) was used to see the magnified images of our samples. It composes of a movable stage that can move in x, y, and z direction. This model has five objective lenses (5×, 10×, 20×, 50× and 100×) and an ocular lens. The image can be seen on the computer by transferring the real image produced by the objective lens towards the camera which is connected to the computer. Some optical images taken from this microscope with a 100× lens are shown in figure 3.3. The visibility of TMDs on a substrate is the result of the difference between the reflectance of visible light from TMDs and the underlying substrate.

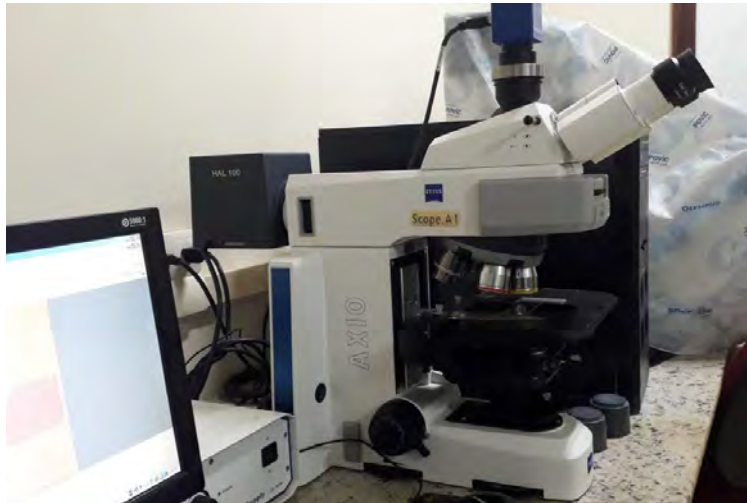
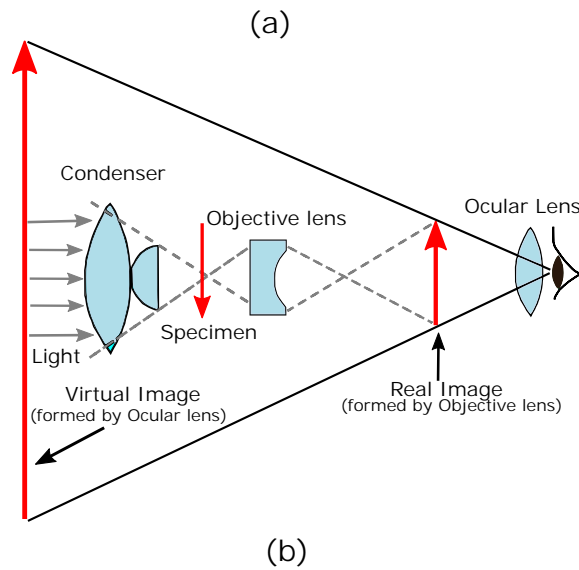


Figure 3.4: (a) Schematic of an optical microscope image formation. (b) ZEISS Axio Scope. A1 at Protective Coatings and Nanostructured Materials Laboratory Vandegraff PUC-Rio.

3.3 Scanning Electron Microscope

Scanning electron microscope (SEM) is a type of microscope that creates the image of a sample by scanning it at a very high energy beam of electrons. The electrons are continuously interacting with the atoms and produce, signals that contain information about the sample surface and bulk, composition, and electrical conductivity. The electron beam is usually, scan in a raster scan pattern, and the position of the beam is combined with the detected signal to produce an image. It gives us the opportunity to see the objects up to few nanometers. Specimens can be observed in high vacuum, in low vacuum, in wet conditions, and at a wide range of cryogenic or elevated temperatures. SEM is

useful in understanding the surface of the sample.

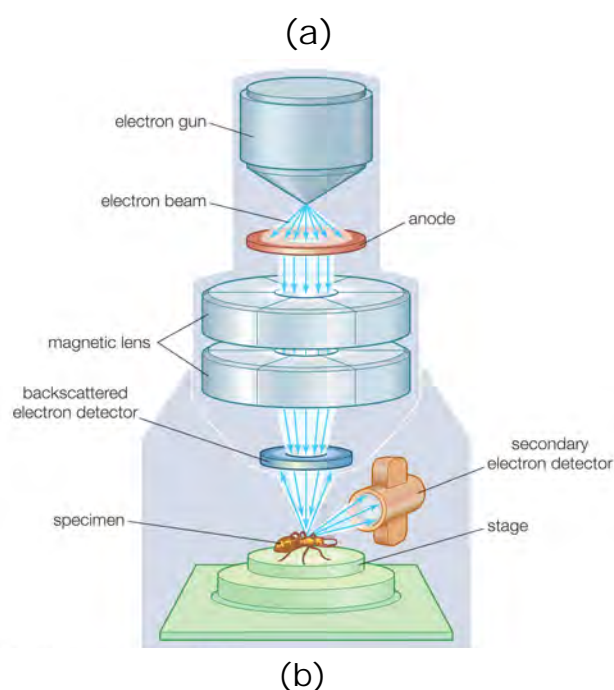


Figure 3.5: (a) Schematic of a SEM image formation. Adopted from [140]. (b) JEOL JSM-7610F Field Emission SEM at vandegraaff PUC-Rio.

In a typical SEM, an electron beam is emitted from an electron gun fitted with a filament cathode made up of tungsten. Tungsten is normally used because it has a very high melting point and lowest vapor pressure in all metals, hence allowing it to be heated for electron emission. The electron beam, which has an energy of 0.2 - 40 keV, is focused by two magnetic lenses to a spot of 0.4 - 5 nm in diameter, see figure 3.5(a) [140]. The beam passes through pairs of scanning coils or pairs of deflector plates in the electron column, typically in the final lens, which deflects the beam in the x and y axes so that it scans

in a raster fashion over a rectangular area of the sample surface.

Now when the primary electron beam interacts with the sample, the electrons lose energy by repeated random scattering and absorption within a teardrop-shaped volume of the specimen known as the interaction volume, which extends from less than 100 nm to approximately 5 μm into the surface. The energy exchange between the electron beam and the sample results in the reflection of high-energy electrons by elastic scattering, emission of secondary electrons by inelastic scattering, and the emission of electromagnetic radiation, each of which can be detected by specialized detectors. The beam current absorbed by the specimen can also be detected and used to create images of the distribution of specimen current. Electronic amplifiers of various types are used to amplify these signals, which are displayed as variations in brightness on a computer monitor. Each pixel of computer video memory is matched with the position of the beam on the specimen in the microscope, and the resulting image is, therefore, a distribution map of the intensity of the signal being emitted from the scanned area of the specimen. Finally, machine image is saved to a computer's data storage. The JEOL JSM-7610F Field Emission SEM was used in our work (figure 3.5(b)), which offers magnification with 0.8 nm resolution at 15 kV (1.0 nm at 1 kV) and unmatched beam stability, making it possible to observe the fine surface morphology of our samples.

3.4

Raman Spectroscopy

Before we discuss the Raman spectroscopy it is important to understand the phenomena behind the Raman scattering.

3.4.1

Raman Effect

Whenever the light (photons) interacts with a medium different processes may occur, such as transmission, reflection, absorption, or luminescence. However, a small fraction of incident light (photons) is scattered because of inhomogeneities inside the medium. The phenomenon of scattering of light from the medium is known as Raman effect first discovered by Sir C.V.Raman in 1928 which earned him the Nobel Prize in 1931 [141]. He has observed when light (photons) are scattered from an atom or a molecule, most of them are elastically scattered which is called Rayleigh scattering, such that the scattered photons have the same energy (frequency and wavelength) as the incident photons. A small fraction of scattered photons, about one in a million, has a difference in energy. This is attributed to the energy absorption by atoms

or molecules and the energy difference was related to the chemical structure of the molecule responsible for the spread. Later on, the Raman effect has become an important tool for analyzing the chemical composition of solids, liquids, and gases. Raman spectrum provides a chemical “fingerprint” of the substance. Using Raman spectroscopy technique one can distinguish between a metallic carbon nanotube, semiconductor, doped graphene samples, disorder in the structure, type of edge (zig - zag and armchair), deformation and tension in the crystal, oxidation, amorphization, number of layers and coupling between layers [142]. So, the Raman process is the starting point for understanding any type of change in the peaks (or band) of the Raman spectrum of the samples.

3.4.2

Theory of Raman Scattering

Consider a photon of energy $h\nu$ collides with a molecule having energy E_i . Photons scatter after colliding with the molecule with frequency ν_o and energy $h\nu_o$, while the molecule will have the final energy as E_f . The change in velocity of a photon before and after the collision is negligible, thus by the law of conservation of energy:

$$E_i + h\nu = E_f + h\nu_o \quad (3-1)$$

$$\implies \nu_o = \nu + (E_i - E_f)/h \quad (3-2)$$

From this equation can have three cases.

- If $E_i = E_f$ then $\nu_o = \nu$, which means that photon is simply deflected from the molecule without losing or gaining energy from it (Elastic collision). This corresponds to Rayleigh scattering.
- If $E_i < E_f$ then $\nu_o < \nu$, which means photon gives its energy to the molecule and hence the scattered photon have less energy than the incident photon. This corresponds to stokes lines.
- If $E_i > E_f$ then $\nu_o > \nu$, which means the molecule was already in excited state and photon absorbs energy from the molecule and resulting in high frequency scattered photon. This corresponds to anti-stokes lines.

From 3-2 we get

$$\nu_o = \nu + \delta E/h \quad (3-3)$$

$$\implies \nu_o - \nu = \delta\nu \quad (3-4)$$

Hence in Raman scattering, the frequency difference of the scattered photon corresponds to the characteristic frequency $\delta\nu$ of the molecule. The stokes and

anti-stokes lines should be equidistant from the Rayleigh line on either side. The process is illustrated in figure 3.6.

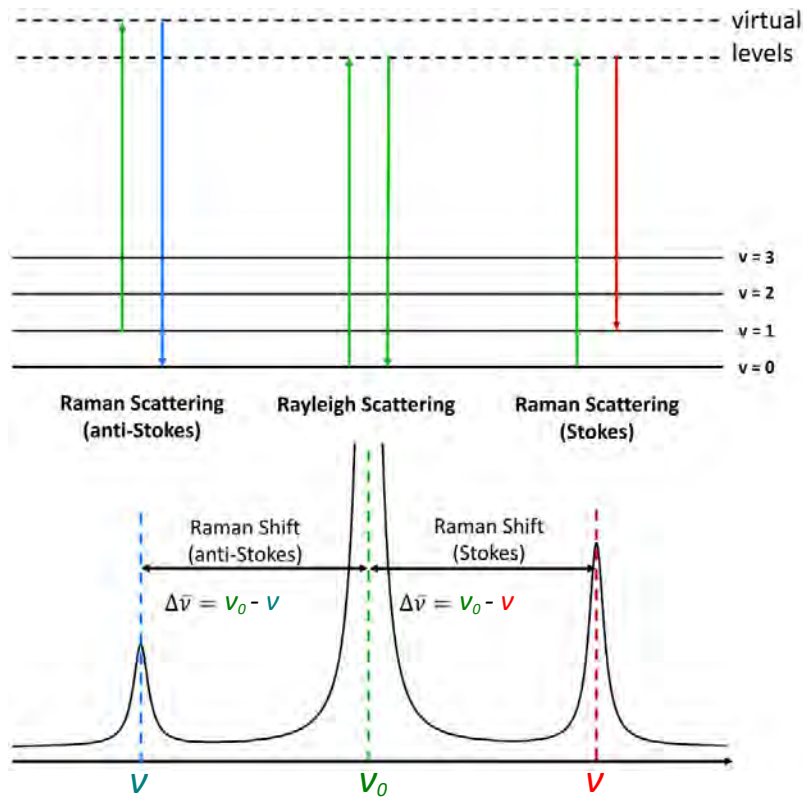


Figure 3.6: Stokes and anti-Stokes Raman scattering.

3.4.3 Raman Spectrometer

Raman spectroscopy is a non-destructive characterization tool and is applicable both in the laboratory and in industrial scale. Raman spectroscopy has become one of the most popular techniques for characterizing 2D materials [143]. It works on the principle of Raman scattering after scattering from the sample Raman spectra is obtained. Raman spectra is a measure of the Stokes process, plotting the intensity of the scattered light as a function of the Raman shift. Raman shift is the difference between the energy of the incident photon and the scattered photon. The units of this displacement are cm^{-1} ($1 \text{ meV} = 8.0655447 \text{ cm}^{-1}$). Figure 3.7(a) shows the schematic of a Raman spectrometer, here we discuss briefly each component and its function step by step.

Laser Laser produces a high power monochromatic light, one can use different wavelength lasers. The laser is incident on the sample under consideration, to activate its vibrational modes.

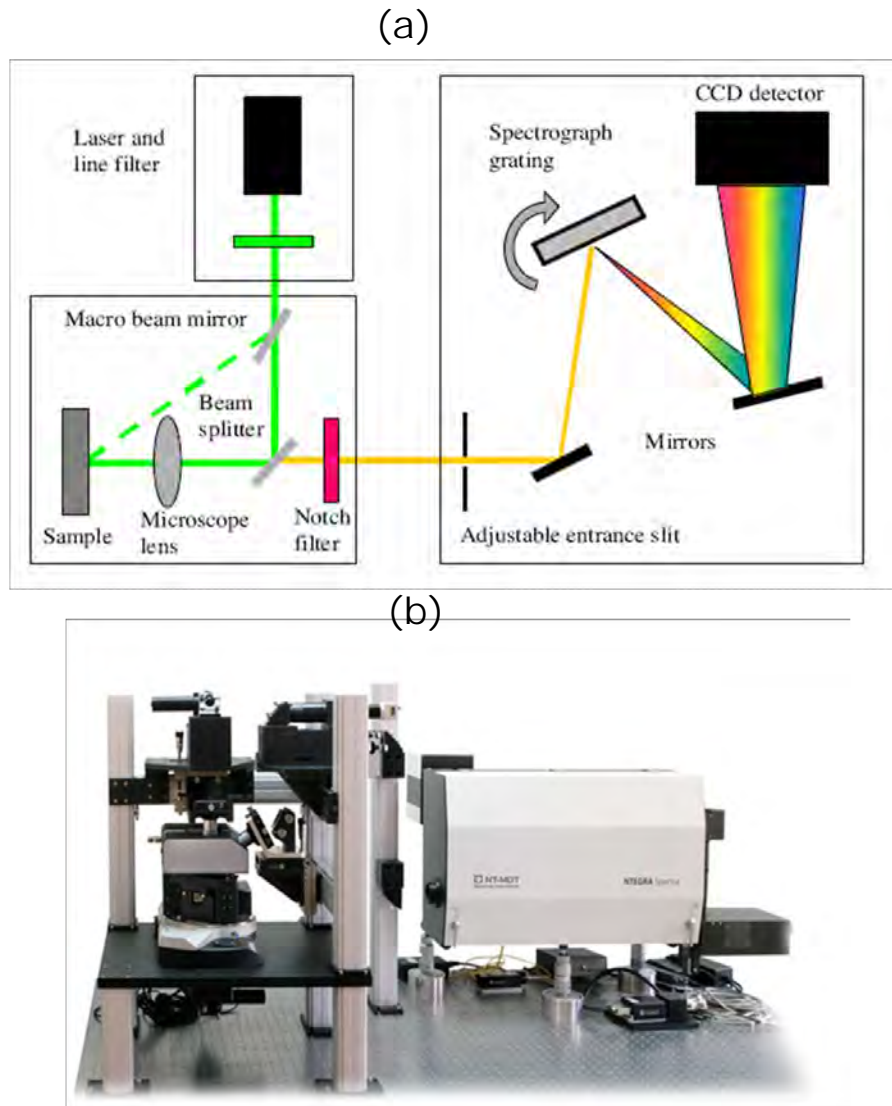


Figure 3.7: (a) Schematics of Raman spectrometer. (b) NT-MDT, NTEGRA Spectrometer at Protective Coatings and Nanostructured Materials Laboratory Vandegraaff PUC-Rio.

Lens It is used to focus the incident laser beam on the sample.

Notch filter A notch filter is a band-stop filter with a narrow stop-band. It passes most frequencies without any change through it but attenuates those in a specific range to a very low level. Scattered laser at the wavelength corresponding to the incident laser line (Rayleigh scattering) is filtered out by notch filter, while the rest of the collected light is dispersed onto a detector.

Grating Grating is the most important component in the Raman spectrometer. It disperses the signal coming from the sample onto the CCD detector by deflecting each wavelength at a different angle. It is made up of many closely

spaced parallel lines (grooves) which permit diffraction gratings to disperse the components of light into separate wavelengths. The number of grooves/mm determines the dispersion characteristics. A high number of grooves/mm results in a high dispersion and thus a high resolution, by distributing the signal over a larger number of CCD pixels. Generally, Raman spectrometer has different grating with different ranges which can be changed according to the sample under consideration.

CCD (charged-coupled device) The CCD camera is the last element in the detection beam path. It converts the photons that reach the chip into electronic signals that can be used to draw the spectra on a computer. This is an important component of a Raman spectrometer and choosing the correct CCD strongly affects the performance of the instrument. The Raman spectra we obtained on the computer shows some peaks at different frequencies, which is a chemical “fingerprint” of the sample and contains the structural information about the substance.

We have performed Raman spectroscopy using a micro-Raman spectrometer (NT-MDT, NTEGRA SPECTRA) equipped with a CCD detector and a solid state laser, with a wavelength of 473 nm (2.62 eV) shown in figure 3.7(b). We performed the experiments using a 100× magnification objective, giving a laser spot of the order of $\sim 1 \mu\text{m}^2$ diameter and a numerical aperture of 0.7. The spectrometer is equipped with a piezoelectric ceramic with all the electronics of a microscope, it allows to make Raman maps over an area of $30 \times 30 \mu\text{m}^2$, with a step size of 1.0 μm . To study the defects XploRA Confocal Raman Microscope - HORIBA equipped with three internal lasers (532, 638 and 785 nm) was used. 532 and 638 nm laser was used to study the second order Raman peaks. The single spectra were acquired with the 100× objective lens which produces a laser spot of $0.9 \mu\text{m}^2$ using a 1800-line/mm grating.

3.5 Photoluminescence Spectroscopy

Photoluminescence spectroscopy is a common technique used to characterize the optoelectronic properties of semiconductors and other materials. Consider a sample absorbs a photon of the incoming light to promote an electron from the ground state in a molecule or (valence band in a solid) to the first excited molecular electronic state or (conduction band in a solid), respectively. After the electron is in the excited state (conduction band), it returns to the ground state (valence band), as a result, a photon can be emitted in the form of electromagnetic radiation. This emission process is called photoluminescence.

The experimental setup of photoluminescence spectroscopy is very simple, a laser tuned to a wavelength close to the bandgap energy of the sample is directed onto the sample. When the laser beam is incident on the sample, photoluminescence occurs and light (photons) is emitted from the sample at wavelengths dependent on the sample composition. The emitted light is directed on the detector and passed into a fiber optic cable and then into a spectrometer. Since the incident laser light is also collected and it usually has a significantly higher intensity, a filter is placed in front of the fiber input to remove the incident laser light. Inside the spectrometer, a diffraction grating diffracts different wavelengths in different directions towards an array of photodetectors that measure the intensity of each wavelength component. This wavelength is then passed to CCD which converts the photons that reach the chip into an electronic signal. The digital information is interpreted by the computer, which can display a PL spectrum. The spectrum indicates the relative intensities of light of different wavelengths entering the detector. Figure 3.8 shows the schematic diagram of the PL experimental setup.

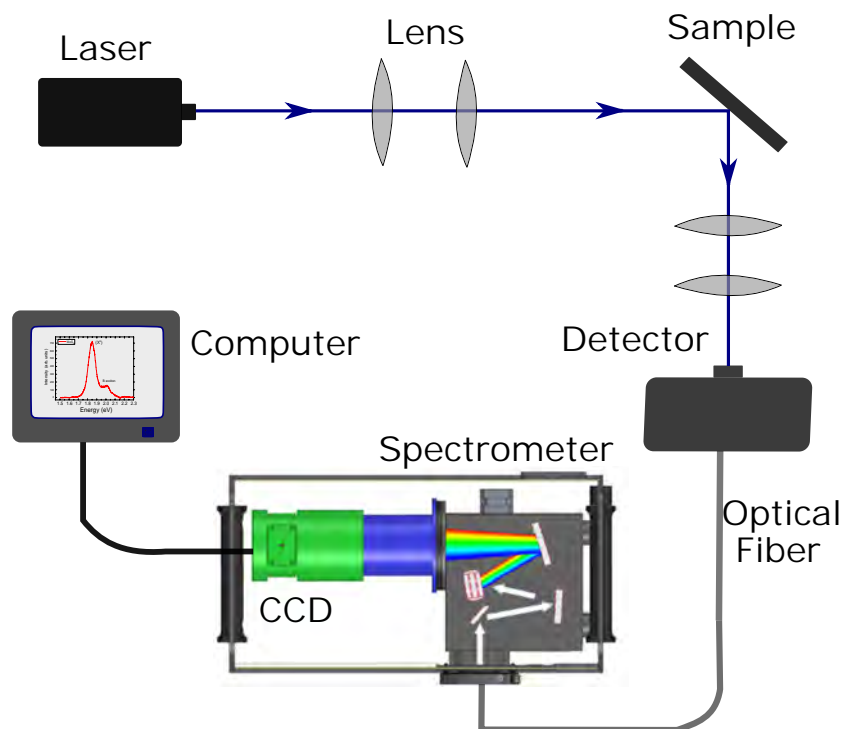


Figure 3.8: Schematic diagram of the PL experimental setup.

Mostly in TMDs compared to PL, Raman scattering is a weak phenomenon and that is sometimes the reason for being unable to acquire a Raman spectrum. Raman spectrometer is ideal for performing laser-excited photoluminescence [144]. We performed the photoluminescence spectroscopy using the

same NT-MDT Raman equipment (figure 3.7(b)). The PL can be measured by changing the grating to 150/600 grooves/mm.

3.6

Atomic Force Microscopy

Atomic force microscopy (AFM) is a technique used to generate images at extremely high resolution and examine features at the atomic level. This makes AFM a perfect technique to characterize TMDs layers. AFM image gives us the surface morphology of a sample, which can be used to measure the exact thickness of a sample. Moreover, this high-resolution AFM image can also give the thickness variation and the distribution of contaminants across the entire surface. AFM is based on the interaction between a tip and the sample surface. This interaction allows us to obtain information about the topography of the sample surface. The interaction force between the tip and the surface is like Van der Waals force. When the distance between the tip and the surface is very small, the electronic orbitals of the surface and tip atoms start repelling each other. AFM can be used for imaging any conducting or non-conducting surface.

The AFM microscope consists of a sharp tip which runs on the sample surface. The interaction force between the atoms of the surface and tip is measured by deflecting a cantilever where the tip is fixed. A diode laser is focused at the end of the cantilever, the laser beam is reflected on a position sensitive photodetector. As the tip moves up and down due to the surface, the cantilever deflects and the intensity changes in the position of four quadrants photodetector. These changes in the position of the tip are recorded by the detector. Using software from the equipment itself, it converts this data into an image based on the position of the cantilever [145]. Generally, cantilever tips are made up of Si_3N_4 or silicon.

Figure 3.9 shows a cantilever deflection detection scheme and a laser beam. Another important aspect of the AFM microscope's operation is the position how the sample is moved since very precise control over this displacement is needed. For this, a piezoelectric ceramic scanner is used which moves the sample in the x, y, and z directions. When an electrical voltage is applied the piezoelectric scanner undergoes a variation in its dimensions, thus controlling the displacement of the sample [146].

In this thesis, we have characterized our samples by contact mode AFM using the same NT-MDT equipment and a $10 \times 10 \mu\text{m}^2$ piezo electric stage. Our NT-MDT is a multifunctional equipment and can be used to generate high quality AFM images [147]. The measurements were taken in contact mode with

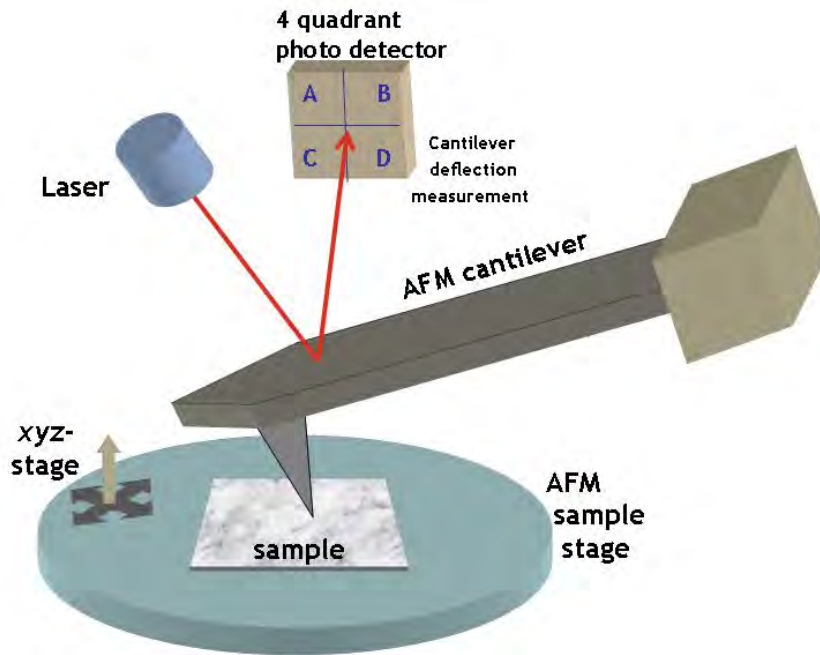


Figure 3.9: Cantilever deflection detection scheme by means of a beam of laser. Adopted from [146].

the silicon tip with gold on top of the cantilever .

3.7 X-ray Photoelectron Spectroscopy

The X-ray photoelectron spectroscopy (XPS) is a surface analysis technique widely used in the study of the composition of an element or a compound. XPS enables us to detect all elements in the periodic table except Hydrogen and Helium, due to the absence of core electrons [148]. This technique was developed by Kai Siegbahn in 1960s and is based on the application of the photoelectric effect. In photoelectric effect when high power electromagnetic radiation, hits a material, if the incident radiation energy is sufficient, an atom absorbing it will result in exciting an electron from the material [149]. The electrons emitted in this manner are called photoelectrons.



Here X is the atom in its fundamental state (containing n electrons), $h\nu$ is the excitation energy, X^+ is the atom in its excited state after being photoionized (containing $n-1$ electrons) and e^- is the emitted photoelectron. Similarly, when an X-ray beam is focused on the surface of the sample, the photoelectric effect occurs and photoelectrons are emitted from the sample. By analyzing the energy of the ejected photoelectrons one can determine the elements present in it. The energy of the photoelectron depends on the element from which it is

originated and the orbital of the ground state in which the electron was found. The energies associated with this excitation, described by the photoelectric effect, can be represented as:

$$h\nu = K.E + B.E + \phi_o \quad (3-6)$$

Where $h\nu$ is the X-ray energy absorbed, K.E is the kinetic energy of the photoelectron after being ejected by the atom, B.E is the electron binding energy, and ϕ_o is the work function of the surface (i.e the minimum energy required to remove an electron of the material, $\phi_o = E_{vacuum} - E_{Fermi}$) [150,151].

In an XPS experiment, the samples are placed in an ultra-high vacuum chamber and are irradiated by an X-ray beam. When the incident beam energy ($h\nu$) is greater or equal to the binding energy (B.E) of an electron at the core level of an atom, these electrons are emitted from the sample surface. These emitted photoelectrons are subsequently separated according to their kinetic energy and counted with the help of an electrostatic analyzer and collected by a detector. The schematic of an XPS setup is shown in figure 3.10 [152].

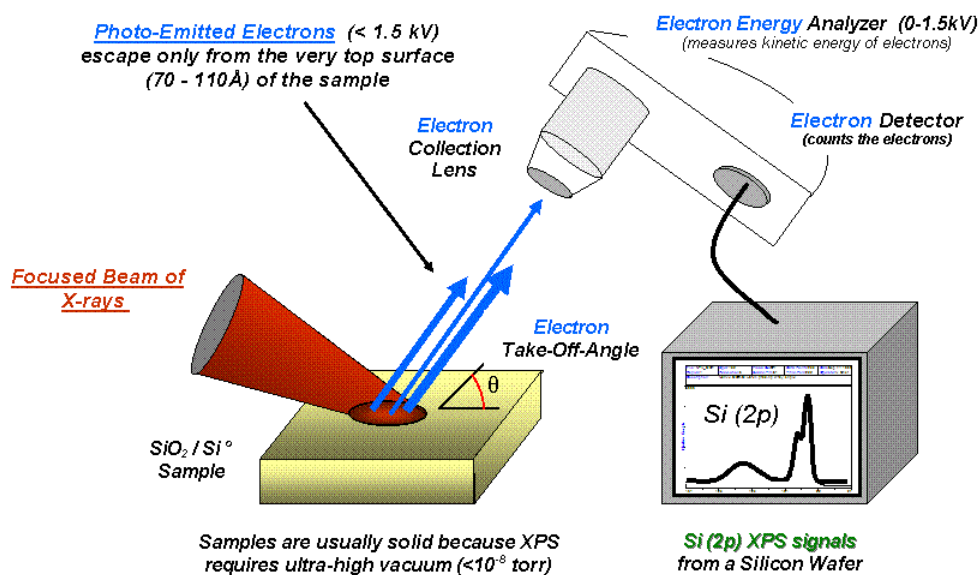


Figure 3.10: Experimental setup for XPS. Adopted from [152].

The XPS setup in vandegraaff laboratory (PUC-Rio) was used in this thesis work, the photoelectrons are filtered in energy with a VG Thermo Alpha 110 hemispherical analyser, later detected by 7 “channeltron” detectors that transform the electrons into an amplified current pulse so that they can be amplified. Finally, the spectrum is recorded as intensity (counts per second) vs. kinetic energy of photoelectrons or their binding energy. The X-rays source used to generate the photoelectrons in the sample was Al-K α (1486.6 eV).

The measurements were performed with the analyser positioned normal to the surface of the sample. Data analysis was performed using the CasaXPS software (from Casa Software Ltd.), taking as a reference for the binding energies the peak of 1s carbon at 284.6 eV. The XPS on our samples was performed by Prof. Marcelo da Costa.

3.8 Introduction to Second Harmonic Generation

Second harmonic generation is a nonlinear optical process in which two photons having the same frequency interact with a nonlinear material, giving rise to a new photon with twice the frequency of the initial photons. The second harmonic generation can occur in non-centrosymmetric materials or at the surface of a material with any symmetry group. However, It is forbidden in centrosymmetric materials. It was first demonstrated in crystalline quartz by P. Franken et al. in 1961 [153].

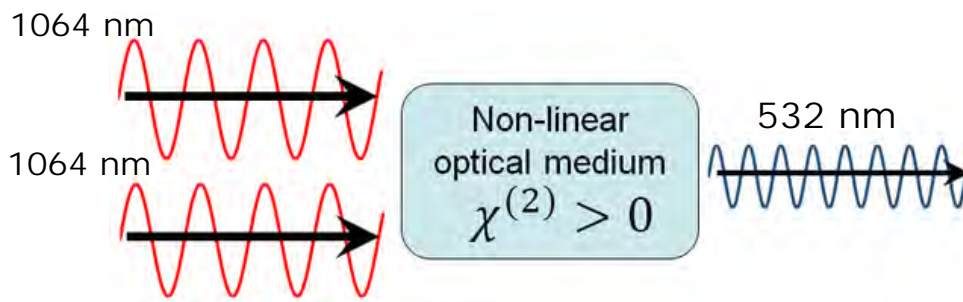


Figure 3.11: General second harmonic generation phenomena.

Figure 3.11 shows when two photons of higher wavelength pass through a nonlinear medium it gives a single photon of half of the wavelength of the initial photon. Second harmonic generation has many practical applications e.g. changing the colour of the laser is possible. Typical green laser (532 nm) is actually the SHG of Nd:YAG laser (1064 nm). Applying a non linear optical crystal KTP, it turns invisible Nd:YAG infrared laser into highly visible green laser. The radiated optical field in SHG is directly proportional to the nonlinear component of the electric polarization of the material, i.e:

$$E_o(\omega) \propto P_o(\omega) \quad (3-7)$$

Microscopically, the nonlinear process can be described by the light-induced polarization expressed as:

$$P_o(\omega) = \epsilon_o \chi^{(1)} E_o(\omega) \quad (3-8)$$

here $\chi^{(1)}$ is the electrical susceptibility of the first order of the material, with the superscript index indicating linear treatment. In isotropic medium susceptibility is a scalar quantity. But due to the anisotropic nature of some materials, it is necessary to analyze susceptibility in tensorial form. In a system with a significantly intense optical field, to intra-atomic fields, polarization can be written as a series of powers of the electric field [154]:

$$P_o(\omega) = \epsilon_o[\chi^{(1)}E_o(\omega) + \chi^{(2)}E_o(\omega)^2 + \chi^{(3)}E_o(\omega)^3 + \dots] \quad (3-9)$$

where $\chi^{(2)}$ and $\chi^{(3)}$ are the second and third order susceptibilities, respectively. The absence of second harmonic generation in centrosymmetric materials is due to the presence of inversion symmetry, the $\chi^{(2)}$ tensor is zero. For SHG to occur we need an even response of the polarization P to the electric field E, i.e. the polarization will have the same direction for a certain electric field E. Obviously for symmetry reasons this is not possible if your lattice is centrosymmetric. The SHG is a fast and non-destructive method to characterize layered TMDs.

Similar way third harmonic generation (THG) is a process that generates light with one-third the wavelength. In THG three photons are destroyed, creating a single photon at three times the frequency. This process can be applied in signal processing, ultrafast laser production, and imaging. This process is generated by the third order non-linear response of the material, it can be used in the characterization of the third order response, regardless of the material will be centro symmetric or not. The THG process can be observed using the same experimental apparatus than the one used for SHG.

3.8.1

Second Harmonic Generation Measurements

We have characterized our samples with second and third harmonic measurements. We have collaborated with Prof. Christiano's group at Mackenzie Presbyterian University, Sao Paulo. The experimental setup for second harmonic generation at Mackgraph, Mackenzie Presbyterian University, SP is shown in figure 3.12. The experimental setup for the analysis can be divided into two branches. The first corresponds to the part responsible for the excitation and collection of the SHG signal. This setup branch contains a 1560 nm Erbium-doped fiber laser, with repetition rate of 89 MHz and pulse duration of 150 fs. The beam is focused on the sample with normal incidence through a 20× objective lens, reaching a beam diameter of $\sim 3 \mu\text{m}$ in the focused region.

The second harmonic is generated on a sample with the wavelength of 780 nm. Then, we collected the signal in reflection. It is separated from the laser pump when passing through a low pass filter (dichroic mirror, Thorlabs,

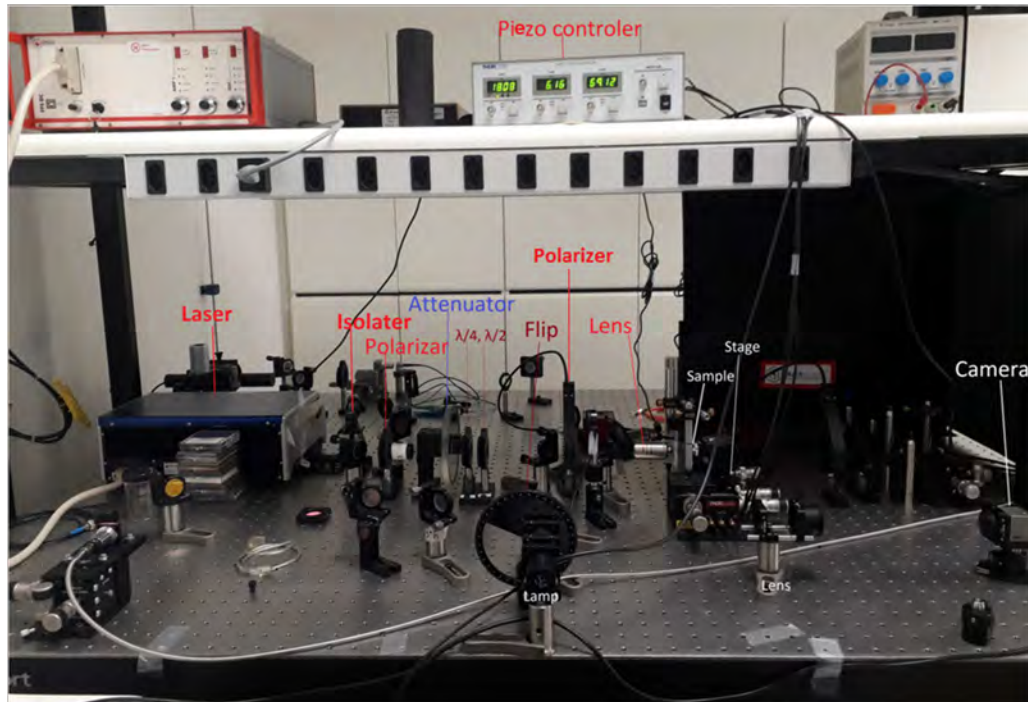
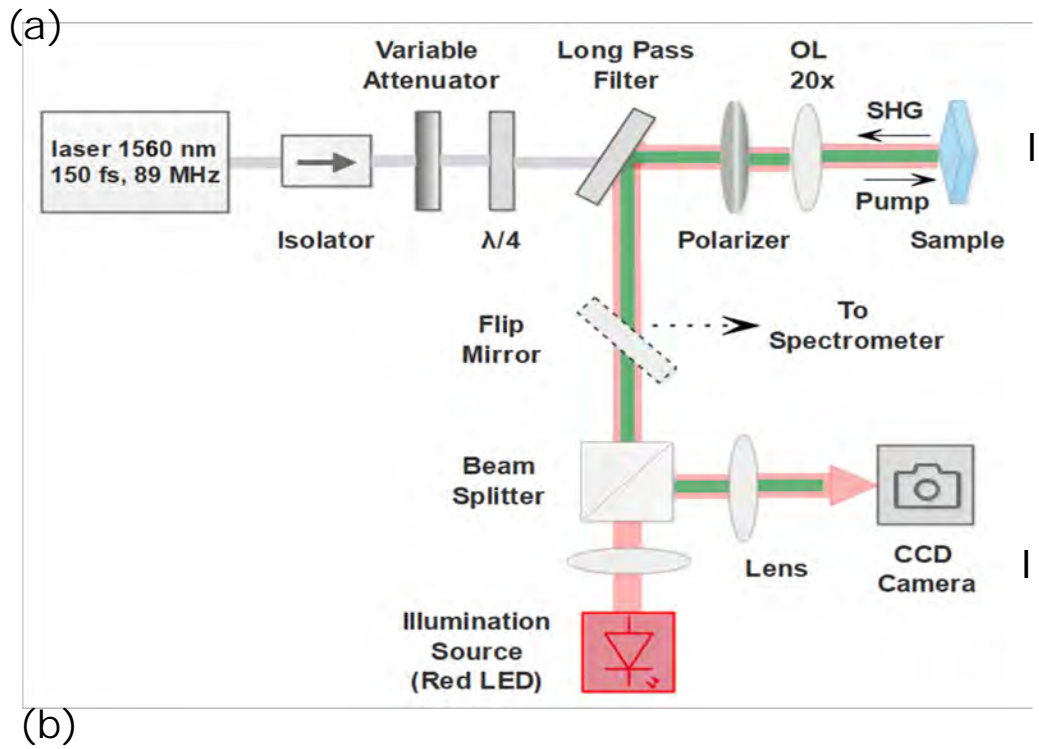


Figure 3.12: (a) Schematic diagram of harmonic generation (SHG and THG) microscopy system. (b) Experimental setup for harmonic generation measurements at Mackgraphe, Mackenzie Presbyterian University, SP.

50% T/R at 950nm, DMLP950) being reflected in a moving mirror and then goes to the spectrometer (Andor Kymera spectrometer coupled to an iDus 416 Silicon CCD camera). A variable optical attenuator was used to control the average input power at 10mW (measured after the linear polarizer). The power limitation is due to the integrity of the sample since higher powers could damage the 2D crystals. The second branch contains a microscope setup, which uses a red LED illumination source, a CCD camera, and other optical components, allowing the samples' real-time imaging.

THG signal (at 520 nm) was also produced simultaneous with SHG signals, it accompanied of microscope setup was used to place the laser pump in the desired region onto the sample, and the collection of both by the spectrometer was performed separately due to the need to select the spectral region of interest before the collection.

For polarization dependence measurements, a quarter-wave plate and a linear polarizer in a rotation stage were used to rotate the light, leading to minimal intensity changes (less than 2% of variation in average power). The linear polarizer also operated as an analyzer. We used an electric piezo stage to ensure that all analyzed regions of the samples were in the same conditions. The optical axis was scanned to obtain the highest SHG intensity.

3.9

Device Fabrication

After a series of materials characterizations, high-quality samples are chosen to fabricate optoelectronic devices. To do it so, device fabrication process is followed. This device fabrication process was done in LabNano at the Brazilian Center of Physical Research (CBPF - Centro Brasileiro de Pesquisas Físicas). To fabricate a device the following steps are defined.

- resist coating
- lithography
- development
- metal deposition
- lift off

3.9.1 Resist Coating

The first step is to clean the surface of the sample to remove all contaminants in order to perform the lithography process. Use alcohol, water, and nitrogen blow to clean the surface. Avoid cleaning with acetone if you are fabricating device on the as-grown samples, acetone can destroy the thin TMD layer on the substrate. Spin coater shown in figure 3.13(a) is used to cover the sample with a thin polymer layer. The polymer resist might be different depending on the lithography we use. There are two main types of resists the positive and the negative resists. The suitable resist can be chosen by dose test. Drop a few drops of the polymer resist on the sample, in our case we choose AZ-1505 positive resist. Spin coat the resist at 4000 rpm for 60 sec this will give us the $\sim 1 \mu\text{m}$ thick polymer layer. The thickness of the polymer layer can be controlled either by the spinning velocity or the viscosity of the resist. The polymer is then hardened by baking it at 105°C for 50 sec on a hot plate see figure 3.13(b). This polymer layer monomerizes when exposing to light.

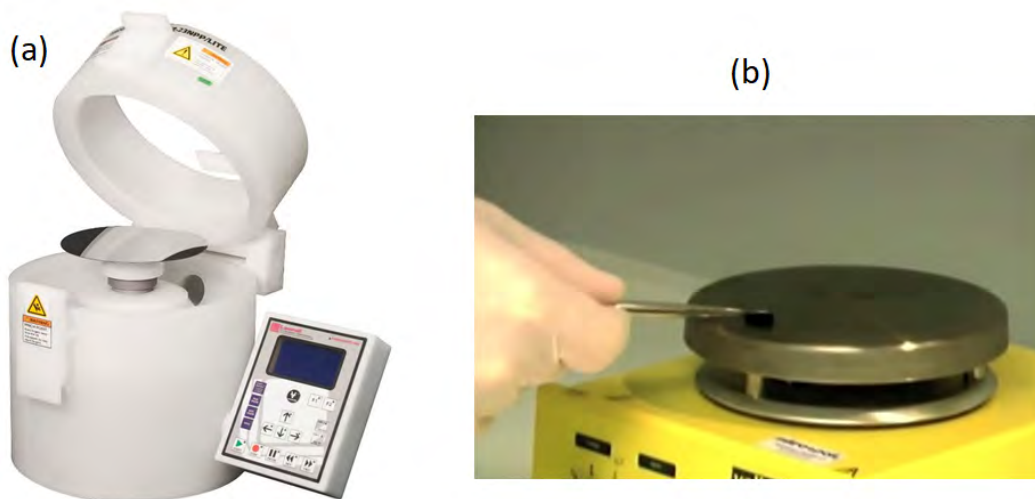


Figure 3.13: (a) Spin coater (model WS-650Hzb-23NPPB-UD-3, at labnano CBPF) was used to cover our sample with a resist. (b) Heating the sample coated with resist on a hot plate.

3.9.2 Lithography

Lithography is a technique of scanning a focused and controlled beam of electrons/Laser to draw a custom pattern on desired sample locations. There are two main types of lithography electron beam and photo-lithography. Both e-beam and photo-lithography have the same process steps in the flow. They

have some differences in the specific photoresists, developers, and facilities. The e-beam lithography can draw patterns up to 4-10 nm [155] however, in photo-lithography we cannot go to this range. In our TMDs samples, we needed two/four-probe devices with minimum contact width of 10-20 μm so photo-lithography was enough for us. We have used the Laser writer (Heidelberg μPG 101 Laser pattern generator) to draw the device circuit see figure 3.14. This Laser writer uses a focused high power laser (633 nm) to draw contact pattern on the surface of a substrate and has a critical dimension resolution of $\sim 3 \mu\text{m}$. The designing procedure takes place in atmospheric pressure and humidity less than 60%. The design pattern is controlled by LibreCAD software. A design pattern on LibreCAD is shown in figure 3.15(a), the LW simply copies the design pattern on the targeted area.

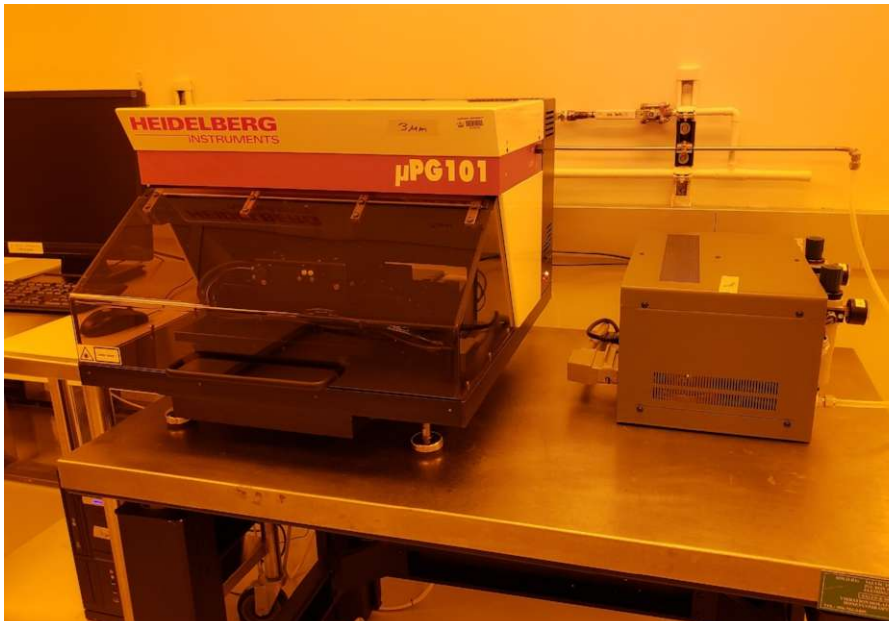
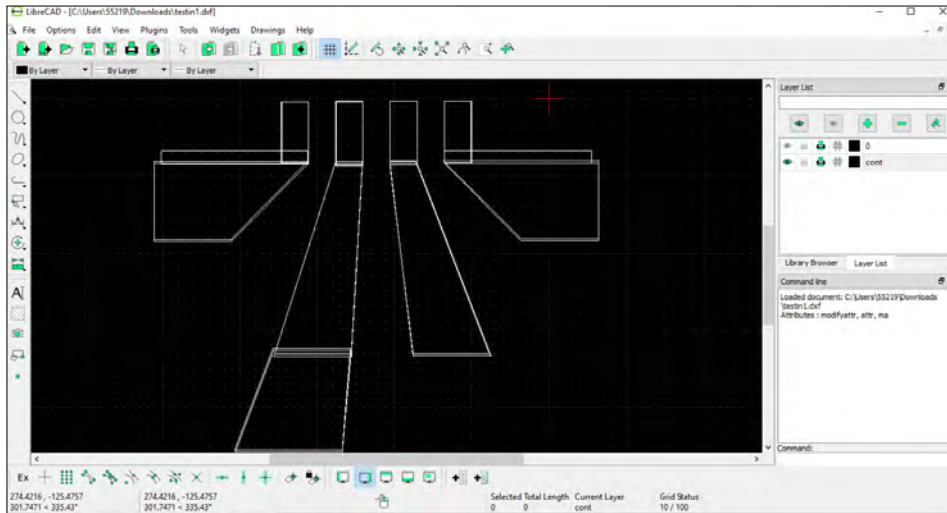


Figure 3.14: Laser writer lithography system model Heidelberg μPG 101 Laser writer at lab nano CBPF.

We need to fabricate the device on a TMD triangle located at a specific area on the substrate. Hence, before the lithography process, the exact distance was calculated from the substrate corners to the triangle with the optical microscope. Which made it easy to reach the targeted area in the Laser writer, optical system. Now, suitable laser power (dose) must be chosen to expose the photoresist from the targeted area. If the device is to be made on transferred samples on SiO_2/Si substrate, normal dose followed for Si substrate i.e. 5mW 70% is good enough. But for the as grown samples, the dose is different and depends on the temperature and time of growth of the sample. A dose test is recommended for every sample, otherwise, the laser will not completely remove

the photoresist from the sample. The best way is to cut a piece from the sample and expose it with different doses. For example, a dose test performed on a sample is shown in figure 3.15(b), showing 5mW 85% is the best dose for this sample.

(a)



(b)

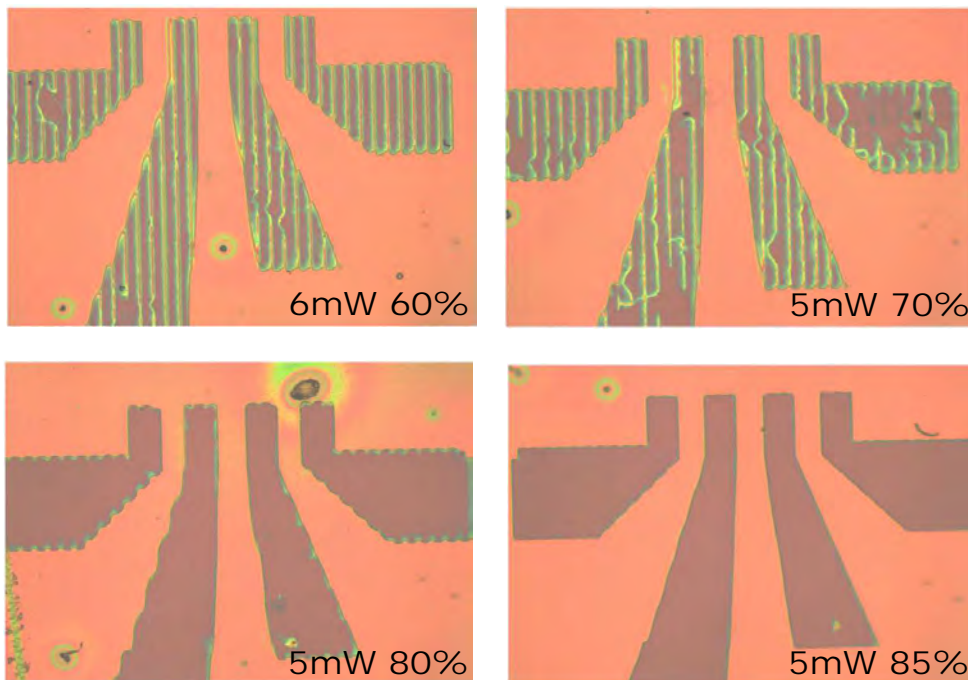


Figure 3.15: (a) Design on a LibreCAD program. (b) Optical images of a sample after development on which dose test was performed with different laser powers.

3.9.3 Development

After lithography, the exposed sample is taken to the development stage. During development, a specific chemical solution (depending on the resist we have used before) is applied to the surface causing photoresist reaction. The molecules in the resist which are not subjected to the laser are strongly bonded together in long chains, while the area which is exposed by the laser is monomerized. After the development process, the non-polymerized parts of the resist decompose leaving the polymerized resist only. In our case we are using AZ-1505 photoresist then we need AZ 300 MIF developer. The sample should be immediately taken out from the LW after the exposure. Hold the sample in your hand dip it in the developer and move it slowly in the liquid for 60 sec. After 60 sec suddenly dip the sample in distilled H₂O and do the same for 60 sec in H₂O, finally dry your sample with air blow. This will dissolve the photoresist which was exposed to laser beam while on the other area resist will be hardened by the developer.

3.9.4 Metal deposition

The next step is the deposition of metal over a design pattern. The metal can be deposited by a sputtering or evaporator system. We have used Edwards thermal evaporator equipment to deposit copper on our sample. First, the sample was placed inside the chamber and vacuum was created to $\sim 2 \times 10^{-6}$ torr. The copper metal is placed in a molybdenum boat through which ~ 12 A current is passed. Then the metal particles are ejected by thermally heating of copper target. That deposits metal over the surface of our sample. On the part where the circuit pattern was drawn, metal can stick directly to the exposed sample. While everywhere else there is still photoresist between the metal and the sample surface. The deposited metal film thickness was determined by a 6 MHz quartz crystal micro-balance assisted by the FTM6 Edwards control unit. Figure 3.16 shows thermal evaporator equipment.

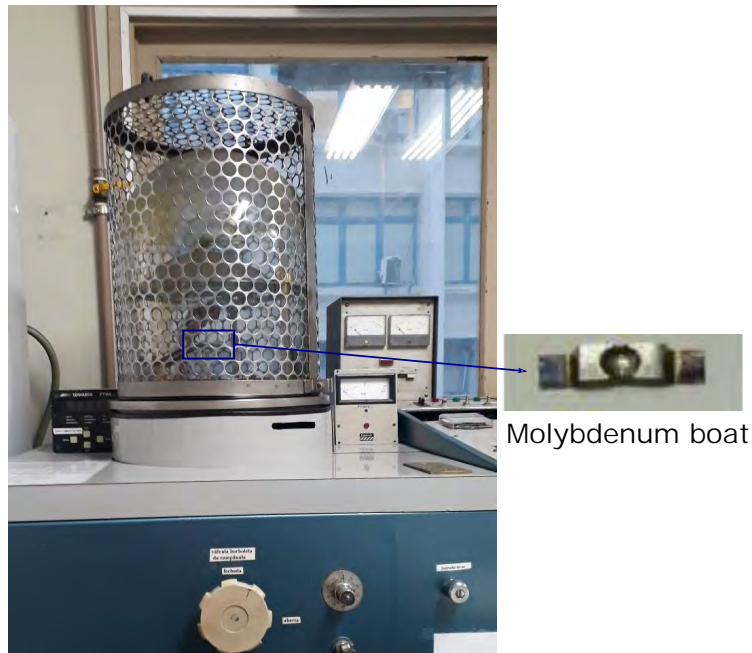


Figure 3.16: Edwards thermal evaporator equipment at Vandegriff PUC-Rio.

3.9.5

Lift off

The final step is the removal of the photoresist and unwanted metal. Silicon substrates are usually treated by plasma etching after the step of photolithography to remove the photoresist residual and clean the Si surface for good device performance. However, if plasma etching is used to treat and clean the surface of a TMDs, they will be damaged severely or etched away completely because of their atomically thin layered structure. An alternative and feasible processing method is to dissolve the photoresist in acetone. This process has to be carried out very carefully and slowly, to avoid damaging circuit pattern or sample during lift off. In my personal experience, this process should be done under an optical microscope. Put your sample in a glass container, focus microscope on the contacts. Now put acetone in the glass container, acetone quickly starts dissolving the photoresist and metal on the resist will also start peeling off. When you see the metal is completely removed especially at the area where contact pattern was drawn on a TMD triangle. Take out the sample immediately and wash it with distilled H_2O . Normally this will take 2-3 min but also depends on the thickness of the deposited metal and photoresist. Dissolving sample for long in acetone will result in damaging the TMD triangle, and dissolving for less time the metal may not be removed completely and we have a short circuit in the device. That's why this process should be done under a microscope. Flow chart of the whole process is shown in figure 3.17. After metal lift-off, a bottom-gated FET device is ready.

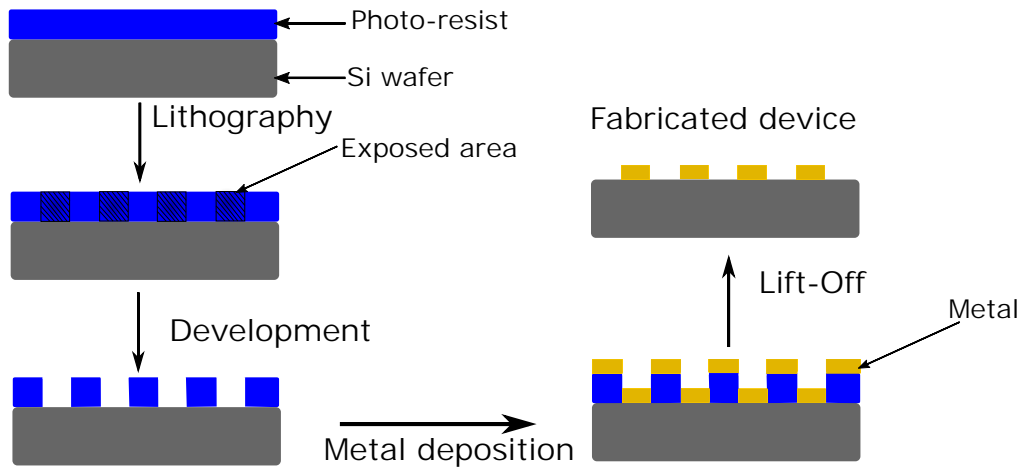


Figure 3.17: General device fabrication procedure.

3.10 Electrical Measurements

After fabricating the devices, the electrical performance of the device was measured at room temperature under ambient conditions. The output curve (I_{DS} vs. V_{DS}) was measured by applying drain-source voltage from Keithley SMU 2400 (with a current source and integrated digital multi-meter). The (I_{DS} vs. V_{DS}) graphs were plotted using a Kickstart 2.1.1 software. The transfer curve was measured by manually applying back gate voltage from p-doped silicon substrate. Figure 3.18 shows the instrumentation used in the experiments.

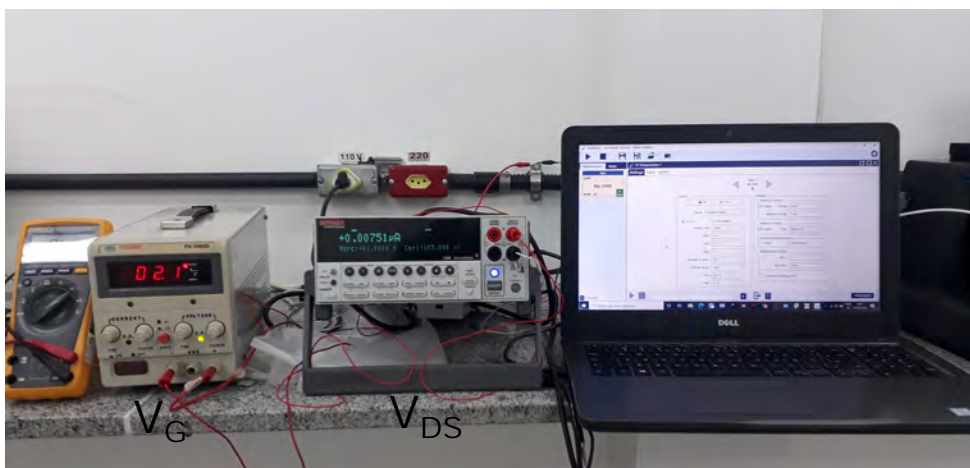


Figure 3.18: Experimental setup for transport measurements.

3.10.1 Electro-Raman

The electro-Raman measurements were performed by applying voltage to our device and at the same time taking Raman spectra. Figure 3.19 shows a schematic of the experimental setup of the spectroscopy measurement with electronics. A confocal Raman spectroscopy system (NT-MDT, NTEGRA spectrometer) was used with the excitation laser of 473 nm. The devices were on a Si substrate, which was mounted on a homemade electronic board. A gate voltage is applied by a voltage source. This is actually a combination of two setups see figure 3.19, a Raman spectrometer working separately, and voltage is applied to the sample only.

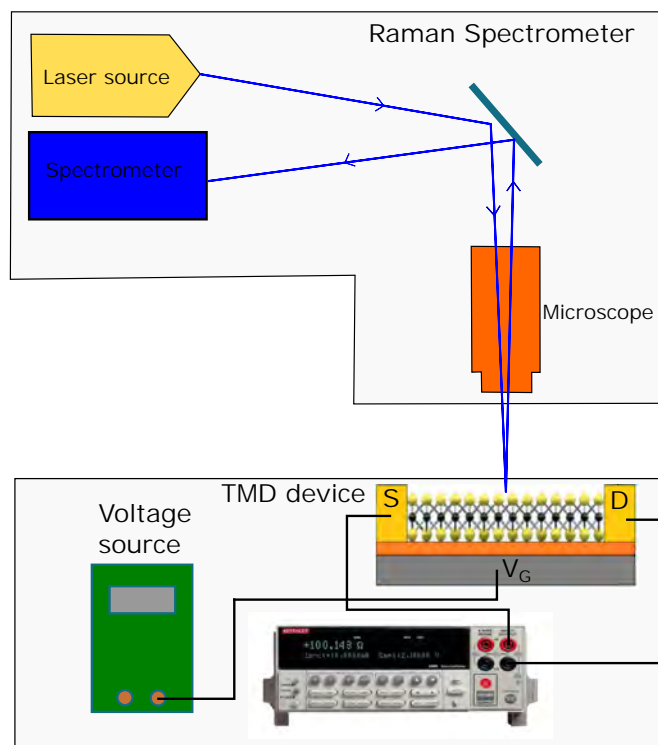


Figure 3.19: Schematic of the experimental setup.

4

CVD Grown MoS₂, WS₂ Monolayer, and their Vertical Heterostructure

In this chapter, the results of the CVD grown monolayer MoS₂, WS₂, and their vertical heterostructure are presented. Their characterizations by atomic force microscopy, Raman and PL spectroscopies are discussed. Detailed explanation of sodium mediated low temperature synthesis of monolayer molybdenum disulfide single crystal triangles and polycrystalline film. The catalytic behavior of sodium in decreasing the synthesis temperature is explained by DFT calculations.

4.1

Introduction

TMDs monolayers have been successfully synthesized by atmospheric pressure chemical vapor deposition (APCVD) on SiO₂/Si substrate. The APCVD process is explained in detail (see chapter 3, section 3.1). After the successful growth of TMDs, several characterization techniques were used to examine the surface morphology, thickness, and optical quality of our samples. The most straightforward technique is the optical microscopy. Layers of the TMDs can be distinguished by colour contrast on SiO₂ substrate arising from the effect of light interference [156–158]. Thus, optical microscopy is usually first used to inspect the TMDs, to get a rough idea of the sample morphology and size before more accurate and higher resolution techniques are conducted. The monolayer thickness and sample quality were also confirmed by three more characterizations AFM, Raman, and PL spectroscopies.

4.2

MoS₂ and WS₂ Monolayer

Typical images acquired by optical microscopy of MoS₂ and WS₂ monolayers grown on SiO₂/Si substrates at high temperature are shown in figure 4.1(a,b). The difference in colour contrast arises due to the different thicknesses of the oxide layer on the Si substrate. The surfaces are covered with an abundance of randomly oriented equilateral triangles typical of growth on the SiO₂/Si substrate [15,159]. Furthermore, the grain-boundaries can be observed

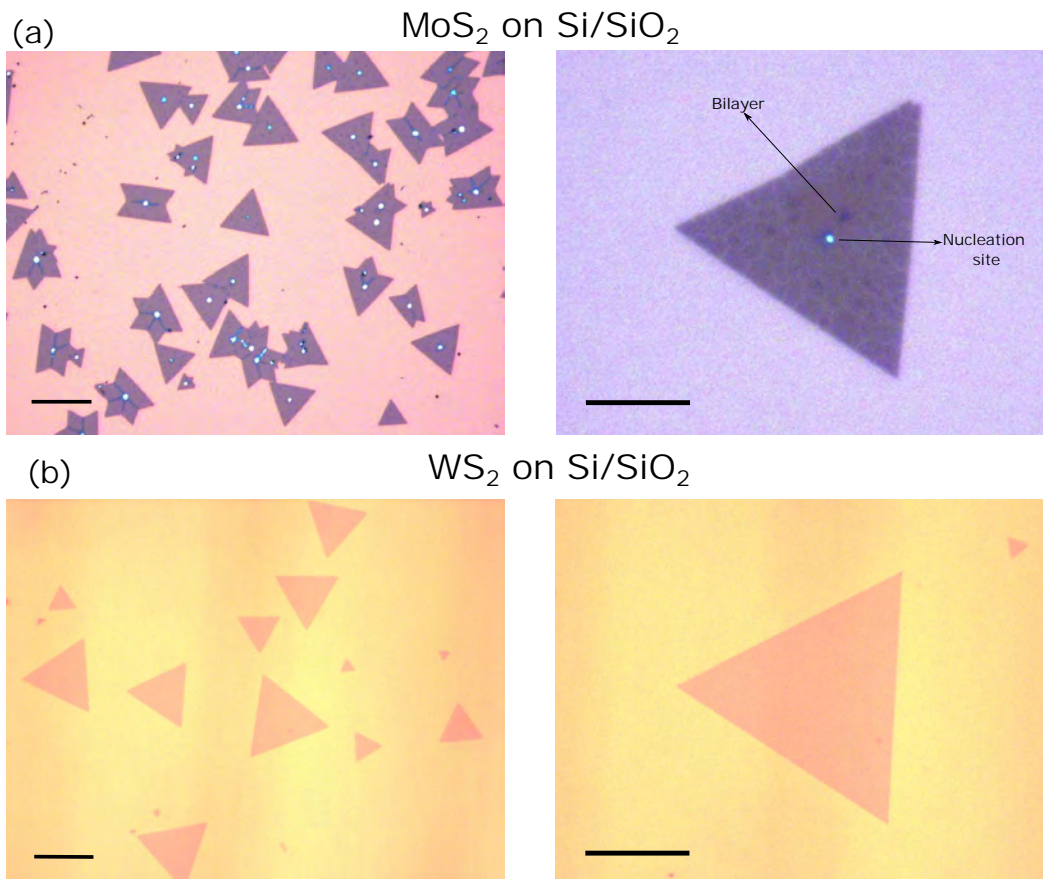


Figure 4.1: (a) Optical microscopy images of MoS_2 grown on SiO_2/Si 285 nm, scale bars are 50 μm and 20 μm . (b) Optical images of WS_2 grown on SiO_2/Si 400 nm.

caused by the coalition of adjacent triangles which is inevitable in CVD grown TMDs [67]. The size of the triangles ranges 20 - 40 μm . A small dot at the centre of the MoS_2 triangles is the nucleation sites and the dark spots are bilayer areas on MoS_2 triangles. The growth occurs at a single nucleation point leading to a monolayer triangular island that grows outward. However, the WS_2 triangles are very clean and in perfect shape showing no dirt or bilayer region on the entire triangular crystallite see figure 4.1(b). Just as our observation, WS_2 was reported to be grown much cleaner and in perfect shaped in CVD synthesis compared to MoS_2 [34, 160], because in sulphur rich atmosphere it common to have an extra layer of S over MoS_2 layer. It can be noted that the colour contrast of all the WS_2 triangles regardless of their size is uniform, which indicates they all are monolayer [157].

To identify the height topography of these triangular islands, atomic force microscopy measurements were carried out. The AFM image of one MoS_2 triangle is shown in figure 4.2(a). In the image we can see the colour contrast between the substrate and the triangle, the line profile inset is showing the

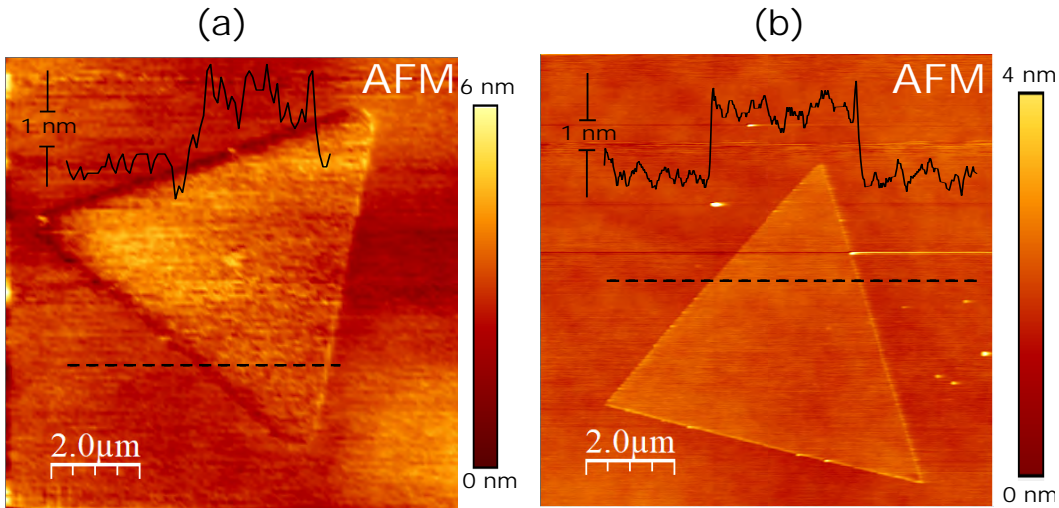


Figure 4.2: (a) AFM topography, profile of MoS₂ flake, inset the line profile shows the step of 1 nm. (b) AFM image of WS₂ flake.

height which is ~ 1 nm. Figure 4.2(b) shows the AFM image of a WS₂ triangle. The height profile in the inset is ~ 0.9 nm which confirms the monolayer thickness [160]. The homogeneous colour contrast in WS₂ crystal shows, it is much cleaner and has smoother surface compared to MoS₂ which can also be noticed in the optical images.

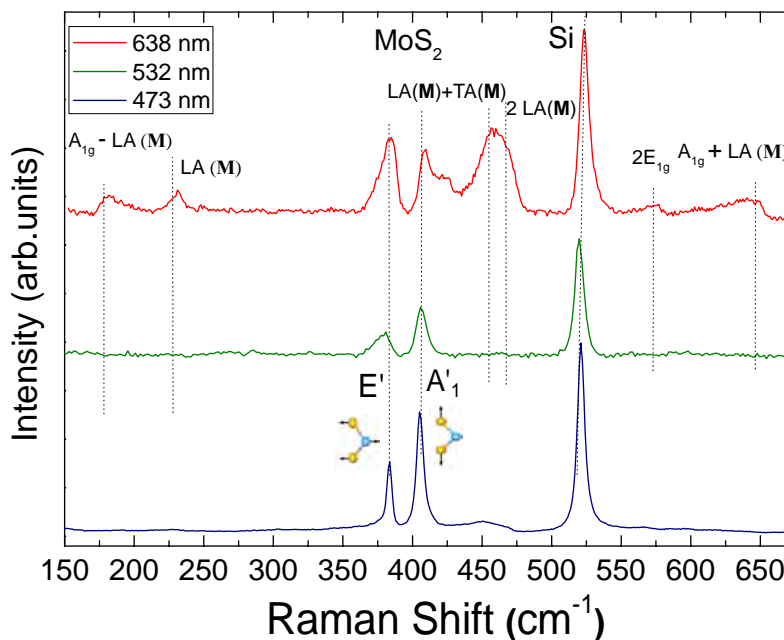


Figure 4.3: Raman spectra of MoS₂ at different excitation wavelengths.

To study the vibrational modes of our samples Raman spectroscopy was used at room temperature under ambient conditions. Raman spectra also provide additional confirmation of the monolayer nature and an indication of

sample quality. Representative Raman spectra obtained from three different excitation wavelengths (473, 532, 638 nm) for monolayer MoS₂ triangle is shown in figure 4.3. For 638 nm laser, we observe many peaks because this wavelength is in resonance with the A exciton of MoS₂. Except the two peaks associated to first-order E' and A'₁ modes, all the other features are contributions from different resonant Raman process.

Here we observe an A_{1g}-LA(M) mode at 179 cm⁻¹ which is assigned as two-phonon difference combination mode [161]. Another peak at 228 cm⁻¹ is LA mode near M point at Brillouin zone, and therefore, it is not a first-order Raman peak. The LA(M) mode is originated from a double resonance process involving one inelastic phonon scattering and one elastic defect scattering. This mode can only be active due to defects in the crystal lattice [46, 162]. The intensity of LA(M) mode is directly proportional to the average of interdefect distance [46]. A prominent appearance of this mode indicates the structural defects in the crystal [163, 164]. The peak at 423 cm⁻¹ is referred to LA(M)+TA(M) [165]. Here we get 2LA band 460 cm⁻¹ which is the strongest feature in the second-order spectrum. The high energy component of the peak at 465 cm⁻¹ was usually related to 2LA at the M point of the MoS₂ Brillouin zone. In high wavenumber region, we observe two prominent peaks at 572 cm⁻¹ and 641 cm⁻¹ which we referred to 2E_{1g} and A_{1g}+LA(M) modes [99]. The most prominent modes in all the spectra are the first order in-plane phonon mode E' and the out-of-plane A'₁ mode. These modes were observed at 383.7 cm⁻¹, 403.8 cm⁻¹. The difference in peak position between these modes is 20.1 cm⁻¹ correspondent to monolayer [166].

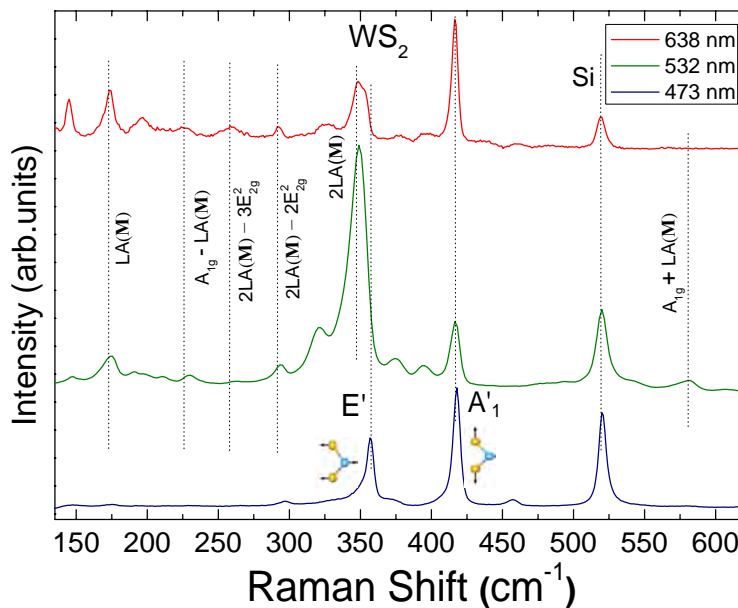


Figure 4.4: Raman spectra of WS₂ at different excitation wavelengths.

The Raman spectra from excitation wavelengths (473, 532, 638 nm) of WS₂ sample are shown in figure 4.4. The 532 nm laser excitation generates a double-resonant Raman process involving the LA(M) mode. The peak at 145 cm⁻¹ is related to out-of-plane acoustic phonons from the border of the BZ, namely ZA(M) [167]. Peak 176 cm⁻¹ can be attributed to a longitudinal acoustic mode from the M point of the BZ, LA(M). All the other second order peaks were assigned in accordance to references [45,168,169]. The first order E' mode is usually overlapped by the 2LA(M) mode in the Raman spectra under resonant condition. To get the exact information about E' and A₁' modes, the 473 nm excitation is used to obtain the non-resonant Raman signal of the WS₂ sample. We found the first order in plane E' mode at 358.8 cm⁻¹ and out of plane A₁' mode at 419.9 cm⁻¹. The difference between these two peaks is 61.1 cm⁻¹ which corresponds to monolayer [45].

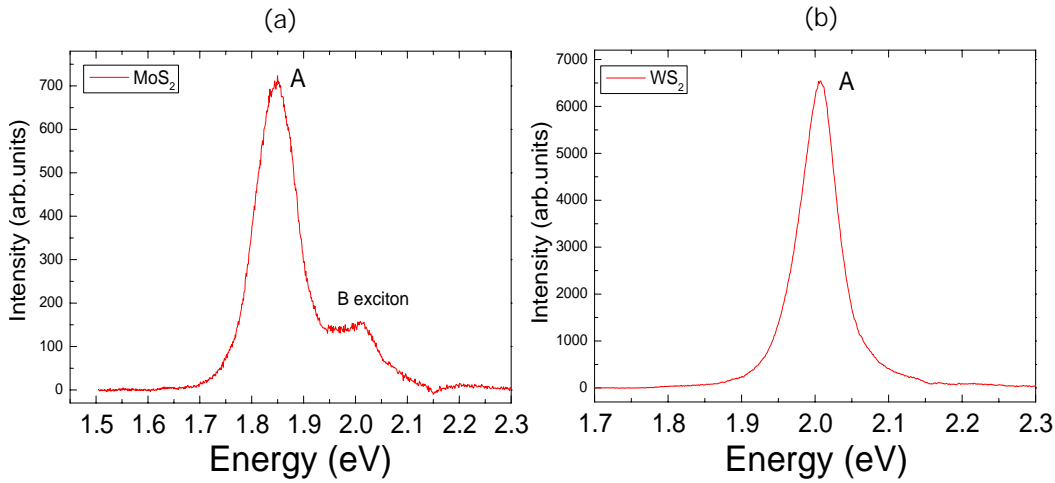


Figure 4.5: (a) Photoluminescence spectra of monolayer MoS₂. (b) Photoluminescence spectra of monolayer WS₂.

Figure 4.5(a) shows the PL spectrum of MoS₂ triangle on SiO₂/Si substrate, exhibited peaks located at 1.83 eV and 2 eV. The two peaks in the PL spectrum are known as A and B excitons, are due to a strong excitonic effect in MoS₂ [11,38]. The separation of (~ 0.17 eV) between A and B excitons come from the spin-orbit splitting at the top of the valence band at the **K** point of the BZ, from $d_{x^2-y^2}$ and d_{xy} states to d_{z^2} type states [109,170,171].

The PL spectra of WS₂ is given in figure 4.5(b). The PL shows an intense peak at 2.05 eV [172]. Both MoS₂ and WS₂ show a sharp, and intense peak in a PL spectrum which indicates the direct bandgap normally observed in monolayer [11,102,173]. The PL emission efficiency of WS₂ monolayer is more than 10 times higher than MoS₂ monolayer. The difference between the valence band and conduction band energy of WS₂ is higher than that of MoS₂ [174].

Hence, is the bandgap energy and PL too, so WS_2 is superior for device applications.

4.3 MoS_2/WS_2 Vertical Heterostructure

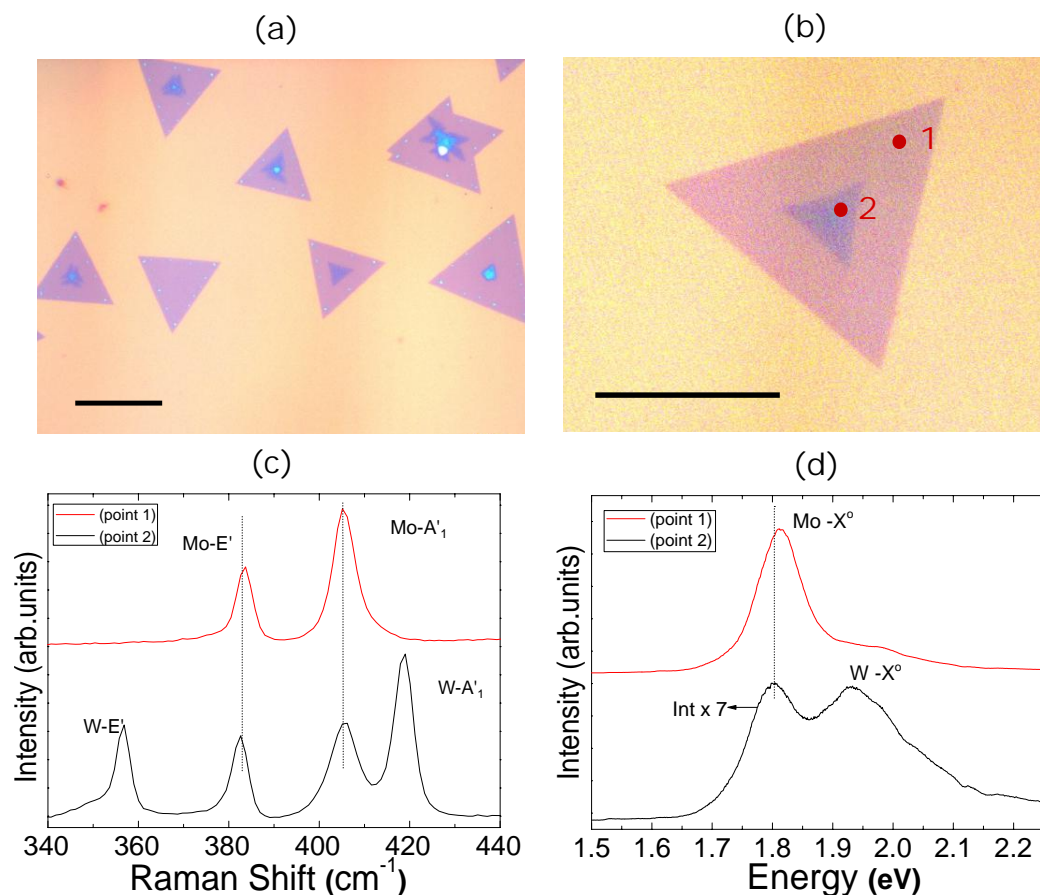


Figure 4.6: (a,b) Optical images of MoS_2/WS_2 vertical heterostructure scale bar is $20 \mu\text{m}$. (c) Raman spectra of MoS_2/WS_2 heterostructure taken at point 1 and 2 as shown in figure 4.6(b). (d) Photoluminescence of the same triangle at point 1 and 2.

We have grown MoS_2/WS_2 vertical heterostructures by APCVD. In these samples, we have a monolayer of MoS_2 and right on top, a WS_2 layer. The optical images of MoS_2/WS_2 heterostructure triangles are shown in figure 4.6(a,b). Not all the triangles are perfectly bilayer heterostructures, some have incomplete growth of the top layer, some have multiple layers on top see figure 4.6(a). The Raman spectra of MoS_2/WS_2 flake shown in figure 4.6(c), was taken at point 1 and 2 marked in figure 4.6(b). It is clear that we have only MoS_2 at the corner of the triangle (point 1) and at the centre at (point 2) we observe four sharp peaks, the first order in-plane and out of plane vibrational

modes from WS₂ and MoS₂ layers. The PL at these two points is also shown in figure 4.6(d). In the heterostructure region we saw two peaks corresponding to the excitonic transition energies of 1.81 eV and 1.93 eV. The peaks can be attributed to MoS₂ bottom and WS₂ top layers. The PL intensity at (point 2) is multiplied by 7 to be compared with the top graph.

4.4

Sodium Mediated Low Temperature Synthesis of Monolayers of Molybdenum Disulfide

We have discussed the high temperature (i.e $\geq 850^{\circ}\text{C}$) synthesis of TMDs. The high temperatures of synthesis is a barrier to mass and low-cost production of monolayers TMDs. One route to reduce the fabrication cost is to decrease the synthesis temperature. Here, we report the CVD synthesis of MoS₂ monolayer on SiO₂/Si substrates at a low temperature $\sim 550^{\circ}\text{C}$ by adding the catalyst sodium nitrate (NaNO₃), as sodium precursor. By using this technique, we can grow single and polycrystals of MoS₂ controlling the synthesis parameters: precursor's ratio and growth time.

We have used the atmospheric pressure chemical vapor deposition system to synthesize the monolayer MoS₂ single crystals and polycrystals. We obtained the crystals by the sulfurization of molybdenum oxide. We used the thermal decomposition of sodium nitrate as a source of sodium [175]. The growth process is carried out inside a quartz tube in a dual-zone tubular furnace (figure 3.1). First, we cleaned the substrate following the same procedure as explained in chapter 3, section 3.1.1. Then a small amount (6 mg) of MoO₃ (Sigma-Aldrich, 99.97% pure) powder along with 2 mg sodium nitrate (Sigma-Aldrich, 99.0% pure) was put in a mortar pestle and ground for 15 min. We loaded the mixed powder in an alumina crucible. The substrate was placed right on top of the powder mixture. The substrate's position is significant in the growth process. If the substrate is placed high from the powder as usually followed in high-temperature synthesis, the growth will not happen. Still, if the substrate is touching the dust, it will eventually result in the growth of bulk instead of a monolayer. We should place the substrate inside the crucible facing downward, but make sure it is a millimetre high from the powder. Then 300-350 mg of sulfur fine powder (99.5% pure) is loaded in another aluminium crucible and then both placed inside the quartz tube. The distance between the two cauldrons is ~ 25 cm. We use the Argon flow rate at 100 sccm inside the quartz tube. During synthesis, the reaction chamber was first heated to 200°C in an Ar atmosphere and left there for 20 min to remove oxygen and other possible sources of contamination from the air. Then, the furnace was

heated independently with the rate of $33^\circ\text{C}/\text{min}$ until it reaches $\sim 550^\circ\text{C}$ for $\text{MoO}_3+\text{NaNO}_3$ powder and 250°C for sulfur powder. Keeping the materials under the respective constant temperatures for the next 12 min, then let it cool down naturally. The flow rate of Ar was kept constant at 100 sccm during the whole growth process.

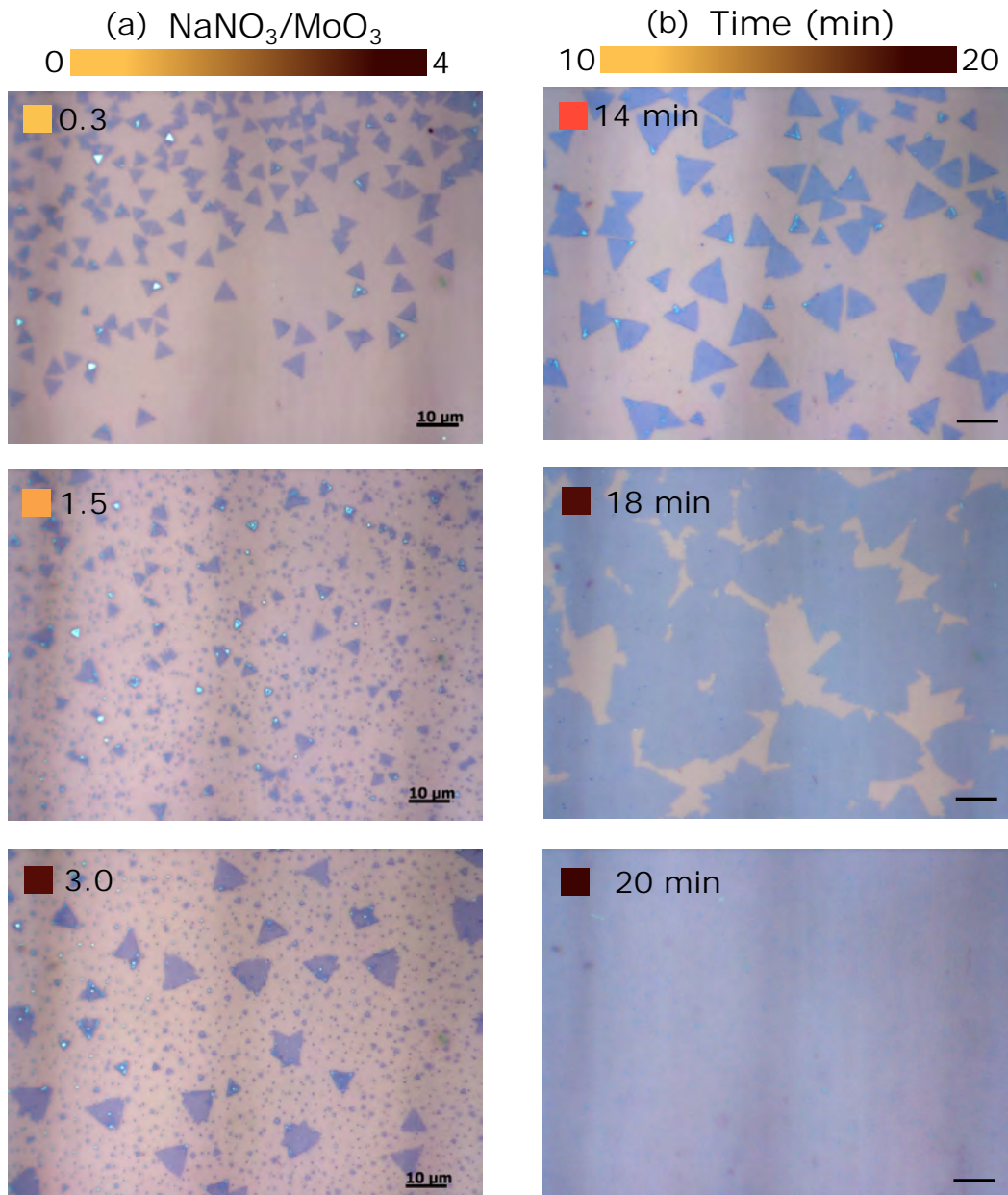


Figure 4.7: Dependence of synthesis parameters in the growth process. (a) Optical images of single-crystalline MoS_2 changing the precursor's ratio $\text{NaNO}_3/\text{MoO}_3$ from 0.3 to 3.0. (b) Optical images show the island coalescence and form the polycrystal MoS_2 by increasing the time from 14 to 20 min, scale bar $10\ \mu\text{m}$.

Finally, MoS_2 single and polycrystals were grown on SiO_2/Si substrates

at $\sim 550^\circ\text{C}$. The synthesis parameters: NaNO₃/MoO₃ precursor's ratio and growth time play an important role in the synthesis process. Figure 4.7(a) shows three optical images of MoS₂ grown using different ratios between NaNO₃ and MoO₃ precursors at a fixed 12 min growth time. We observed that for ratios > 1 , a large number of nucleation sites (small dots in the second and third images) did not have an ideal grown process, and some of the triangles have multiple layers at the corners. However, for ratio 0.3, we can find monolayers in perfect triangular shape. The average size of a triangle is approximately $5\ \mu\text{m}$. Two scanning electron micrograph images, see figure 4.8, confirm the morphology of MoS₂ samples. Optical images in figure 4.7(b) shows the MoS₂ grown at different growth times by keeping the ratio equal to 0.3. By increasing the growth time from 14 min to 20 min, the size of the triangles keeps on growing and eventually merge to form a uniform polycrystalline MoS₂ film. From these experiments, we have found that the ideal growth parameters are precursor ratio 0.3 with growth time 12 min to single crystals and 20 min to polycrystalline films at temperature $\sim 550^\circ\text{C}$.

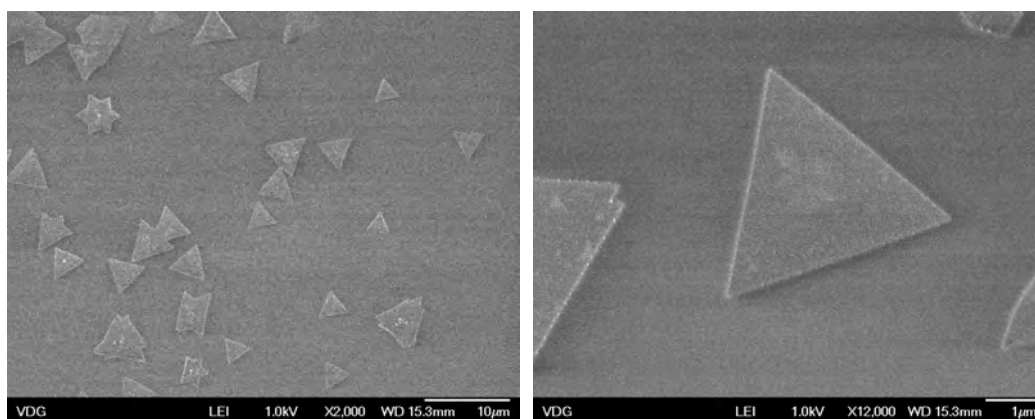


Figure 4.8: SEM images of MoS₂ single crystals.

We acquired X-ray photoelectron spectroscopy (XPS) spectra to examine the presence of sodium after the grown process. Figure 4.9(a) shows the XPS spectra of MoS₂ film. The detailed XPS spectra and fits for Mo and S peaks are shown in figure 4.9(c,d). The characteristic peaks at 229.4 and 232.5 eV corresponds to molybdenum 3d^{5/2} and 3d^{3/2} and peaks at 162.6 eV and 163.8 eV are in line with sulfur 2p^{3/2} and 2p^{1/2}, respectively. The peaks positions agree with the previous report [176]. We found a small amount of sodium by observing the peak at 1073 eV. To clarify the origin of sodium, we did a water bath to our crystals for 2 hr and retook the XPS. After the bath, we do not observed the sodium on the XPS spectrum, see figure 4.9(b). This evidence

clarifies that sodium is only acting as a mediator in the growth process and can not found on the crystalline lattice of MoS_2 . Besides that, the synthesis does not occur at $\sim 550^\circ\text{C}$ without sodium. Hence, the sodium promotes a catalytic chemical reaction and the reduction of synthesis temperature.

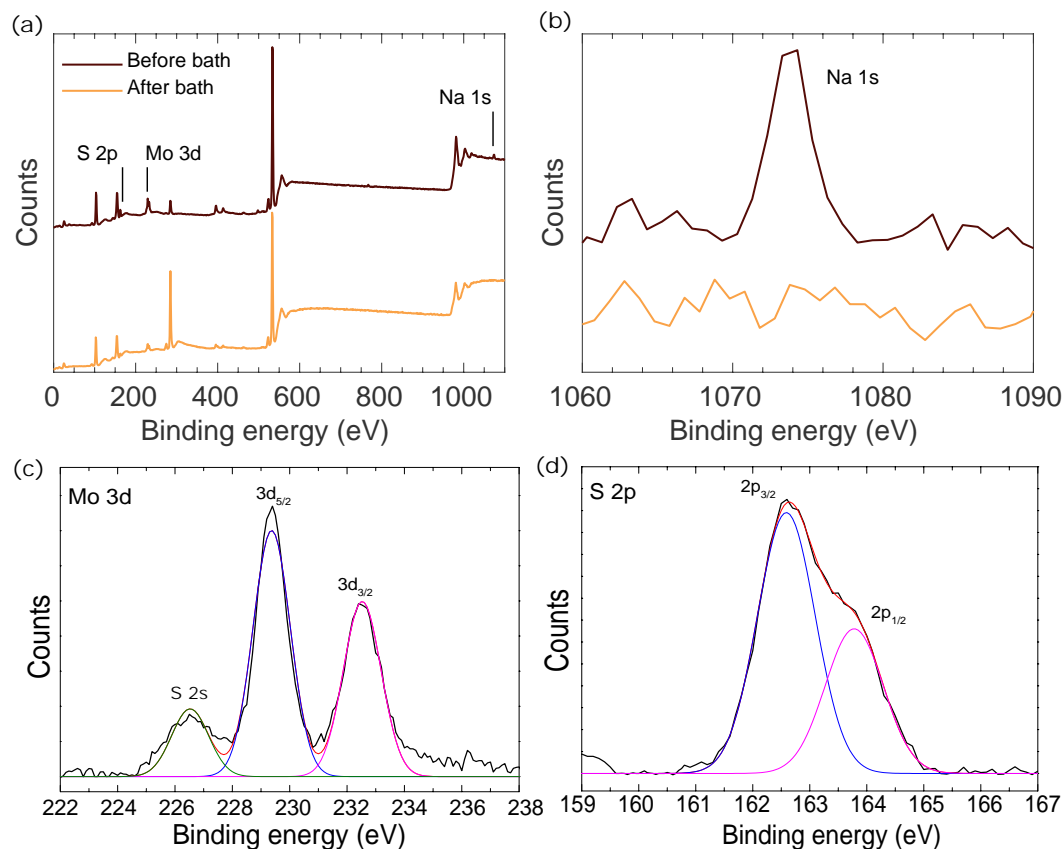


Figure 4.9: XPS experiments. (a) XPS spectra of the grown sample before and after water bath for 2 hr. (b) Detailed XPS spectra of Na 1s peak before and after water bath. Detailed XPS spectra and fitting of Mo and S peaks. (c) Molybdenum 3d spectrum of MoS_2 grown on SiO_2/Si substrate. (d) S 2p spectrum of the same sample.

4.4.1 Catalytic Behaviour of Na Explained by DFT Calculations

In order to understand the role of the Na atoms on the growth of the MoS₂ structures, we perform a DFT calculation of the formation energy, as function of the sodium concentration. A 3×3 MoS₂ supercell crystal structure is built, and the Na atoms are initially placed parallel to the Mo plane, in the direction of the center of hexagons. We relax the whole structure minimizing the energy and the forces keeping the supercell size fixed and, after that, we compute the total energy of the final structures of sodium atoms and the MoS₂ supercell constrained by the Na in a separately way. The formation energy is given by $E_{\text{form}} = [E(\text{MoS}_2 + \text{Na})] - [E(\text{MoS}_2) + E(\text{Na})]$, and for all concentrations of Na/MoS₂ we find that $E_{\text{form}} < 0$, which confirms that the presence of the Na is favorable for the formation of MoS₂.

In our model, the Na atoms form a hexagonal lattice that provides nucleation sites to the formation of MoS₂. The theoretical lattice parameter of the MoS₂ is $a_{\text{MoS}_2} = 3.237 \text{ \AA}$, while for the hexagonal lattice of Na atoms the optimal distance that minimizes the energy is $a_{\text{Na}} = 3.655 \text{ \AA}$. This value is close to the separation between Na atoms in the (111) plane of the Face Centered Cubic (FCC) crystal cell of NaCl ($\approx 4 \text{ \AA}$) and is also close, but a slight large, then the MoS₂ lattice parameter. In this way, a large concentration of Na provides more nucleation sites, but the S atoms close to the Na will be more constrained. On the other hand, large supercells of the MoS₂ are very unlikely to be produced in the low concentration regime because the Na atoms tend to be close to each other.

Figures 4.10(a-f) show structures after the energy minimization. For the 0.1 ratio in figure 4.10(a) the single Na atom is exactly in the direction of the center of one of the hexagons, and it is $3a_{\text{MoS}_2}$ away to the next neighbor (not shown in the figure). In the real synthesis procedure, MoO₃ and NaNO₃ ratio can be controlled, but not the position of Na sites after the reaction, which means that sparse distributions like in figure 4.7(a) in large systems is very unlikely (with minimal entropy), and only small supercells can be grown in this concentration. In figure 4.10(b) the two Na atoms are close one to each other. However, it is not exactly in the direction of the center of the hexagons. The relative position change from 3.237 \AA to 3.543 \AA in the energy minimization process, while the changes in the position of the Mo and S atoms are around 0.1%. The change in the relative position between atoms in the MoS₂ is also small for the 0.3 ratios shown in figure 4.10(c) and the average distance between Na atoms is 3.578 \AA , while between the closest Mo and S atoms are 3.216 \AA and 3.245 \AA , respectively. For the other concentrations in figures 4.10(a-f), the

change in the Mo and S position are considerably large, and this effect can be seen in figure 4.10(g).

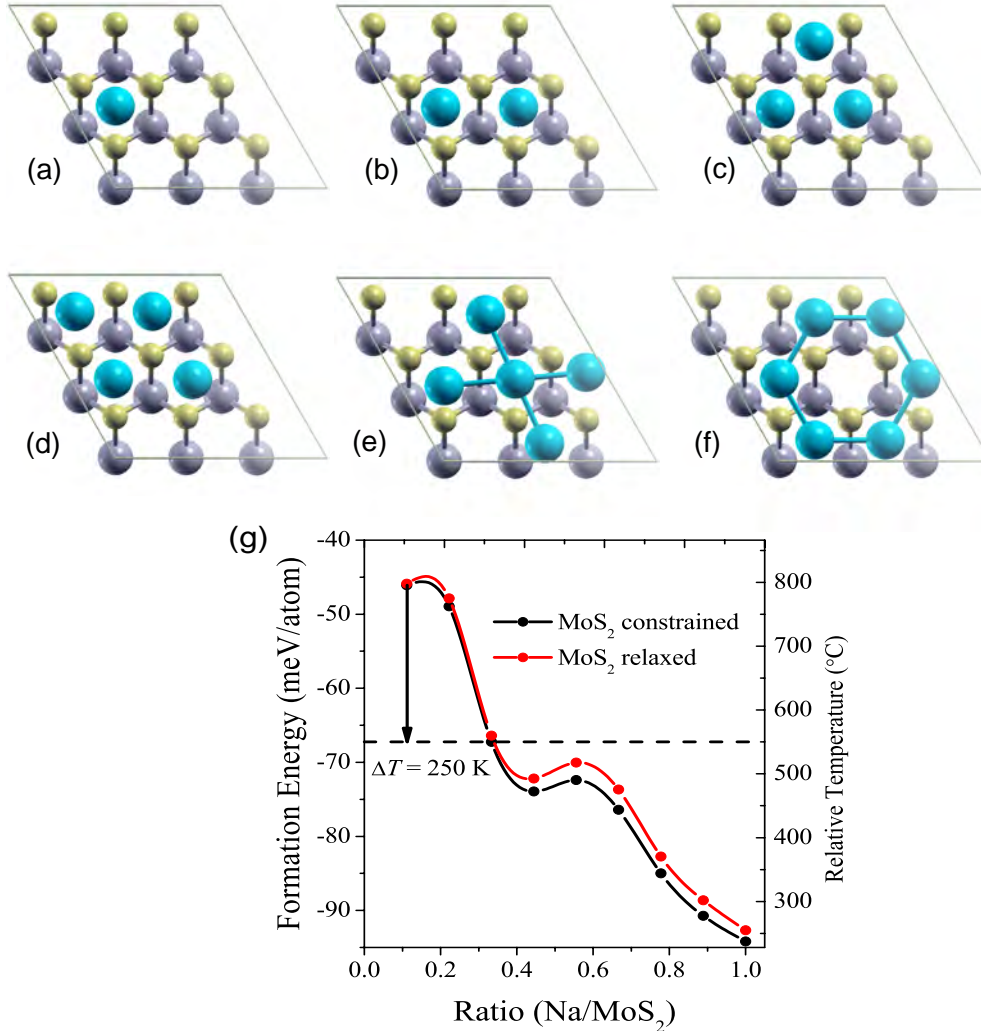


Figure 4.10: DFT calculations of the formation energy. (a-f) Atomic positions after minimization of the energy and forces in a 3×3 fixed size supercell of MoS_2 in the presence of Na atoms. The light blue, dark grey and dark yellow balls represent the Na, Mo, and S atoms, respectively. (g) Formation energy per atom computed with the MoS_2 constrained by the presence of the Na after the minimization (black circles) and fully relaxed (red circles). The full black and red lines are guides to the eyes. The vertical axis on the right side is a conversion of energy to temperature.

We plot the formation energy per atom for different ratios of Na and MoS_2 in figure 4.10(g). In this Figure, the black circle is the formation energy computed when the presence of the Na still constrains the MoS_2 system, and the red circles are computed using the fully relaxed MoS_2 lattice. We see that the difference in energy between the relaxed and constrained systems increases

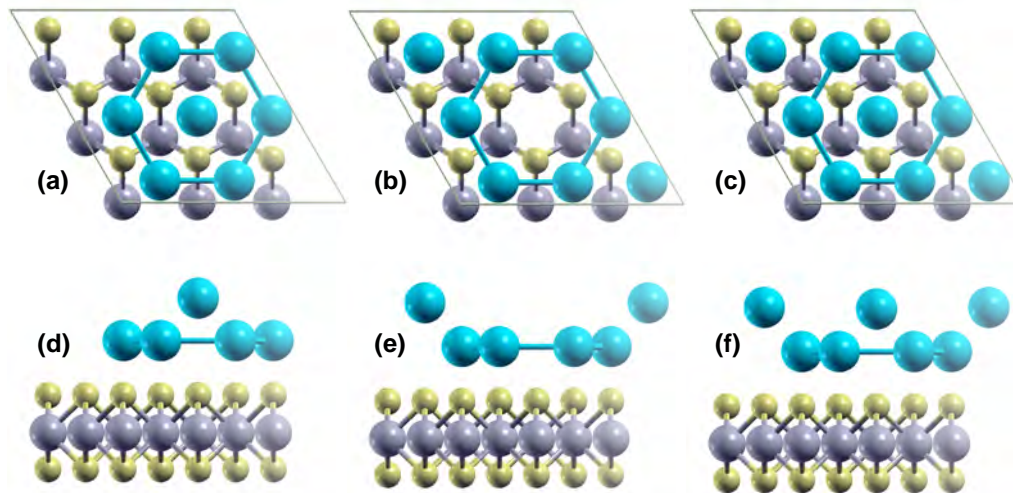


Figure 4.11: Final structures for large concentrations of Na in MoS_2 . (a-c) top view of the 3×3 MoS_2 supercell with 7, 8, and 9 Na atoms, respectively. (d-f) side view of the same structures in (a-c), respectively. The average distance between Na atoms and the plane with Mo are approximately 4.0 \AA (first layer) and 5.8 \AA (second layer). For the low concentration regimes (i.e. < 0.45) the average distance varies approximately linearly between 3.7 \AA and 4.0 \AA with the number of the Na atoms in the supercell.

with the Na concentration indicating that the lattice is more distorted in this regime. Figure 4.10(g) also shows that the formation energy decreases drastically, as expected when more Na sites are present. At the ratio 0.3, the MoS_2 lattice is almost unchanged, with a decrease in the formation energy of the same order of the decrease in temperature ($\Delta T = 250^\circ\text{C}$) which fully agree with the experimental ideal growth parameters discussed before. For concentrations larger than 0.7, our calculations indicate that some Na are not on the same plane as the others, and due to the repulsion between a large number of atoms in a small confinement space (see figure 4.11), the minimal energy configuration starts to have two layers of sodium. Although these configurations present smaller formation energies, the Na atoms located in the extra layer does not play a fundamental role in the formation of large MoS_2 cells because they are far away from the molybdenum and sulfur atoms.

(The DFT calculations for our system was done by Prof. Marcus V. O. Moutinho from UFRJ. DFT calculations were performed in the generalized gradient approximation of the exchange-correlation effect. The QUANTUMESPRESSO package [177] was used with ultrasoft Perdew–Burke–Ernzerhof pseudopotentials and plane-wave cutoff energy of 60 Ry).

4.4.2 Chemical Equations Explaining the Growth

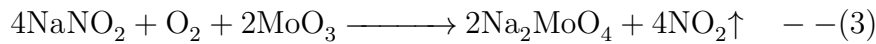
Within the subject process (1), some parallel reactions occur, as follows:



At the temperatures higher than 380°C, in parallel with the main reaction (1), sodium nitrate undergoes decomposition (2) and free oxygen forms nitrogen(IV) oxide (gas).



In parallel, solid MoO₃ reacts with sodium nitrite, whereas water-soluble sodium molybdate is formed. The gaseous products (NO₂ and SO₂) are removed with Ar flow.



This Na₂MoO₄ is now present as contamination on the substrate which is evident in XPS, Na₂MoO₄ is soluble in water by giving water bath to the sample we can remove Na⁺.

4.4.3 Characterization of Na Mediated Synthesized Samples

We turn our attention to investigate the structural and optical properties of MoS₂ single crystals. Figure 4.12(a) shows the AFM image of a triangle, the line profile inset is uniform and has a height of 1.0 nm, which confirms the monolayer thickness [11,15,28]. Figure 4.12(b) shows one representative Raman spectrum (473 nm) obtained from the same MoS₂ monolayer. The recorded Raman spectrum exhibited the in-plane phonon mode E' at 379.7 cm⁻¹ and the out-of-plane A₁' mode at 399.7 cm⁻¹ [96]. The difference in peak position between these modes is 20 cm⁻¹, which corresponds to monolayer [166]. The FWHM of E' peak has a value of 3.4 cm⁻¹, indicating high crystalline quality with no amorphous phase [99]. We performed a Raman mapping over the same triangle. Figures 4.12(c) and (d) present the peak intensity map of A₁' and E'

modes, respectively. The maps show a uniform intensity distribution inside the triangle, while at the corners, the intensity is lower, most likely due to the edge defects [178,179]. The peak position maps of these modes are shown in figure 4.12(e,f), showing uniformity throughout the area of the triangles. These maps are evidence of the uniform structural quality of the crystal.

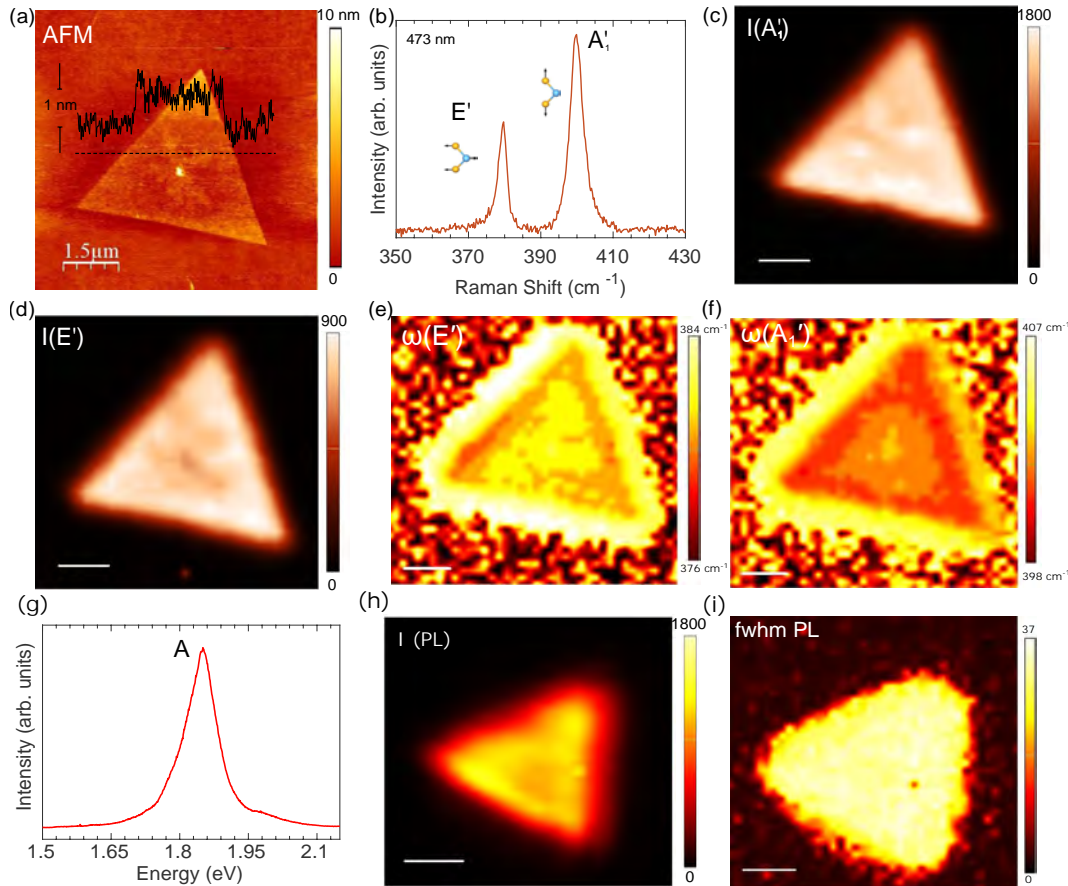


Figure 4.12: Characterization of single crystal. (a) AFM image of a monolayer of MoS_2 , inset the line profile shows the step of 1 nm. (b) Raman spectra of MoS_2 monolayer from 473 nm laser line taken from (a). (c) mapping of A_1' intensity mode and (d) E' intensity mode, scale bar $1 \mu\text{m}$. (e) The peak position maps of E' and (f) A_1' modes showing uniformity throughout the triangles area. (g) Photoluminescence spectra taken of MoS_2 . (h) PL intensity map of A exciton, scale bar $1 \mu\text{m}$. (i) fwhm of Photoluminescence.

Figure 4.12(g) shows the photoluminescence spectra of the MoS_2 triangle exhibiting a A exciton peak at 670 nm (1.85 eV). The intense photoluminescence is a result of the direct bandgap present in monolayer [11, 102, 173]. A single, sharp, and intense peak in the PL spectrum indicates our sample's high optical quality. Furthermore, the PL mapping of the corresponding triangle also indicates uniformity at PL emission see figure 4.12(i). The uniform in-

tensity overall triangle is an indicator of the identical thickness. All the maps demonstrate that this entire MoS_2 crystal is an equal monolayer triangle.

Further, we investigated the polycrystalline monolayer MoS_2 formed by the coalescence of triangles shown in figure 4.7(b). The Raman and Photoluminescence spectra of the film, indicates the crystalline structure and confirm the monolayer thickness. We have selected different areas on the MoS_2 film and did AFM, Raman, and PL mappings. The AFM shows a uniformly flat surface over the crystal, see figure 4.13(a). The small holes appearing on the image could result from the not perfect matching between triangles during the coalescence.

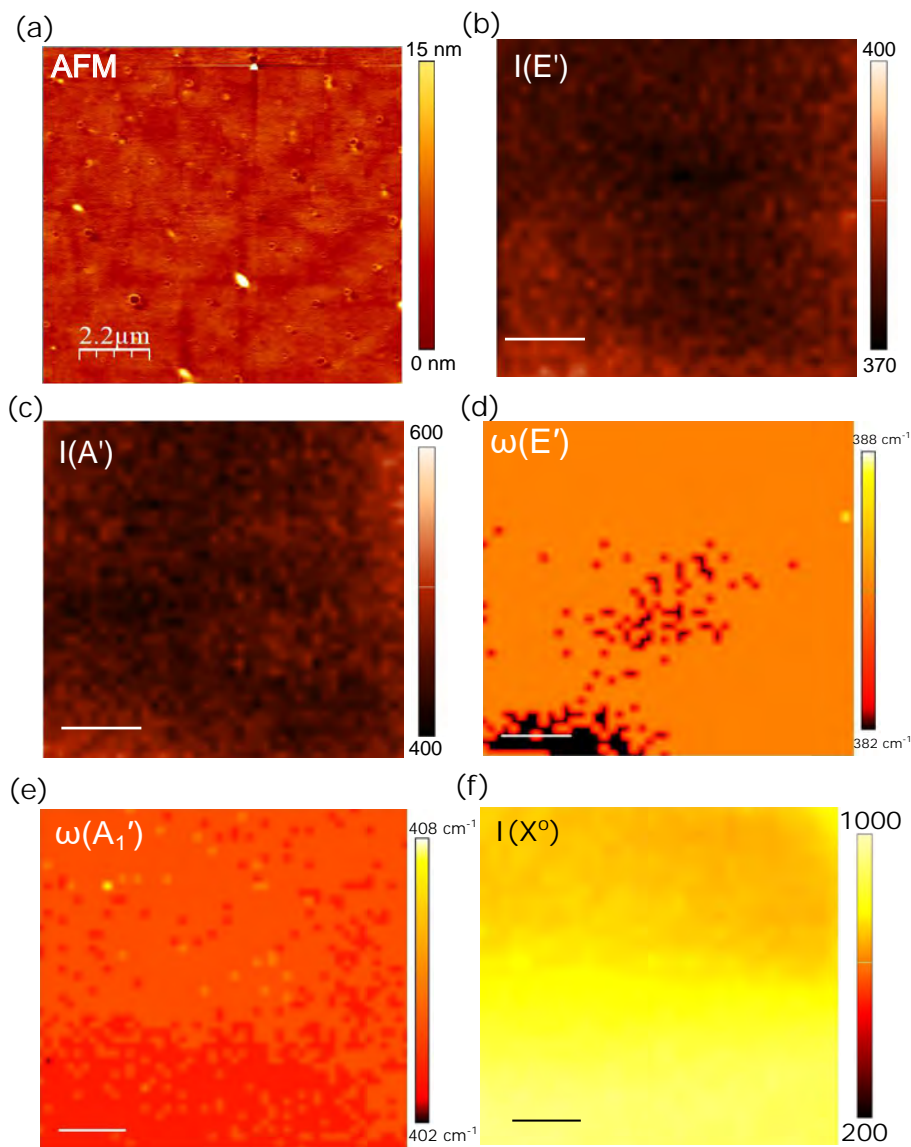


Figure 4.13: Characterization of polycrystal. (a) AFM image of polycrystalline MoS_2 . (b) Raman mapping of E' intensity mode and (c) A_1' intensity mode, scale bar $2 \mu\text{m}$. (d) peak position maps of E' and, (e) A_1' mode (f) PL intensity map, scale bar $2 \mu\text{m}$.

Moreover, Raman mapping on the intensity of E' and A₁' modes and peak position maps of the corresponding sample E' and A₁' modes shows uniform color contrast see figures 4.13(b-e), which demonstrates its perfect thickness uniformity and crystallinity over a large scale. The PL intensity map is shown in figure 4.13(f). The results show that increasing the growth time, it will possibly achieve a uniform monolayer MoS₂ film.

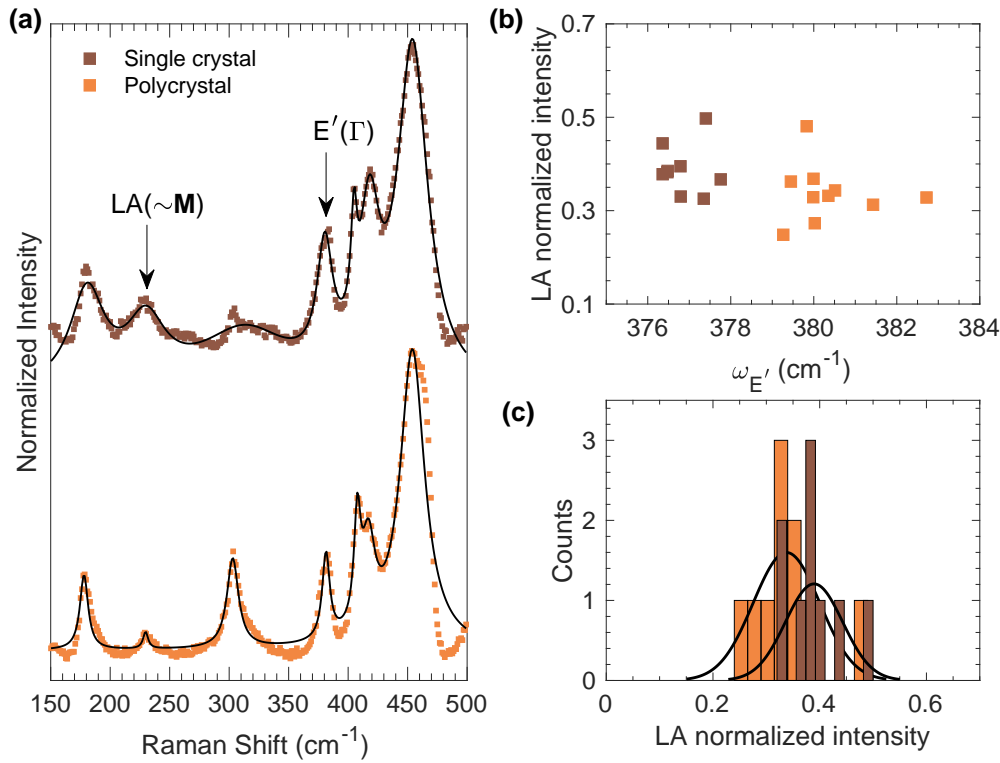


Figure 4.14: Analysis of defects using Raman spectroscopy. (a) Raman spectra of single and polycrystal of MoS₂ with the fitting. (b) Normalized intensity of LA mode in the function of E' frequency. (c) Histograms of LA mode of single and polycrystals.

We acquired Raman spectra using the 638 nm laser line to study the defects on our as-grown single and polycrystals. Figure 4.14(a) presents the representative Raman spectra of single crystal and polycrystal. The mode at $\sim 379 \text{ cm}^{-1}$ corresponds to E'. The peak at 228 cm^{-1} is defect related LA mode near **M** point at Brillouin zone. We took Raman spectra of ten different single crystal and ten from areas at a polycrystalline film to quantify the structural defects. We use a Lorentzian function to adjust the Raman spectra, and the disorder-activated LA(**M**) mode was normalized with the corresponding first-order E' mode. In figure 4.14(b), we plotted the normalized intensity of LA peak, as a function of E' frequency. We observe two distinct sets of data. The $\sim 3 \text{ cm}^{-1}$ blueshift of E' mode of polycrystal when compare

to single crystals indicate the presence of strain [180]. Probably, the strain comes from the coalescence of triangles during the grown process, showing in figure 4.14(b). The histograms in figure 4.14(c) shows the distribution of LA normalized intensity for both sets of samples. We found the average intensity ratio for single crystal 0.39 while for polycrystal 0.34. Hence, the LA mode intensity points out a similar number of defects between single crystals and polycrystals.

We also investigated the electrical properties of our crystals using the two probe devices fabricated on the as-grown sample, the detailed results are given in chapter 6. Our devices show high electrical performance and the mobility is estimated as $9.8 \pm 0.7 \text{ cm}^2\text{V}^{-1}\text{s}^{-1}$ for single crystal and $2.7 \pm 0.5 \text{ cm}^2\text{V}^{-1}\text{s}^{-1}$ for polycrystal which is comparable with the previous reports [28, 32, 69, 181]. The relatively low electron mobility of the film is likely due to the presence of domain boundaries in the polycrystals, which could trap electrons and affect the charge transfer. Typically, in high-temperature synthesis, it is common to observe gate voltage leakage through pinholes caused by the destruction of a thin SiO₂ layer. Another advantage of low-temperature synthesis is the possibility to direct fabrication of the device, avoiding the transfer procedure.

4.5 Synthesis of MoS₂ on Glass

We have discussed so far, sodium assisted growth which enables us to decrease the synthesis temperature. This encouraged us to move on to the direct and low temperature synthesis on the glass. The transition temperature of ordinary glass is 564°C, so a recipe that works below this temperature is needed. We synthesized MoS₂ triangular monolayer on glass at low temperature $\sim 520^\circ\text{C}$, by direct sulfurization of MoO₃ powder. By keeping in mind the catalytic behaviour of Na we have chosen borosilicate glass (composed of, 80 % silica, 13% boric oxide, 4% sodium oxide, and 3% aluminium oxide) as a substrate. The synthesis process is the same for glass as explained in Na mediated synthesis process except adding NaNO₃, because glass itself has Na which can act as nucleation sites and helps in low temperature synthesis.

First of all the grown sample was analyzed by optical microscopy. An optical image of MoS₂ glass sample is shown in figure 4.15(a) showing most of the triangles have multiple layers with very few monolayer triangles. As explained earlier by DFT calculations large amount of sodium although helps in decreasing the synthesis temperature, but starts growing multiple layers instead of single layer triangular islands. The higher density of multiple layers present in our sample is a result of higher sodium concentration in borosilicate

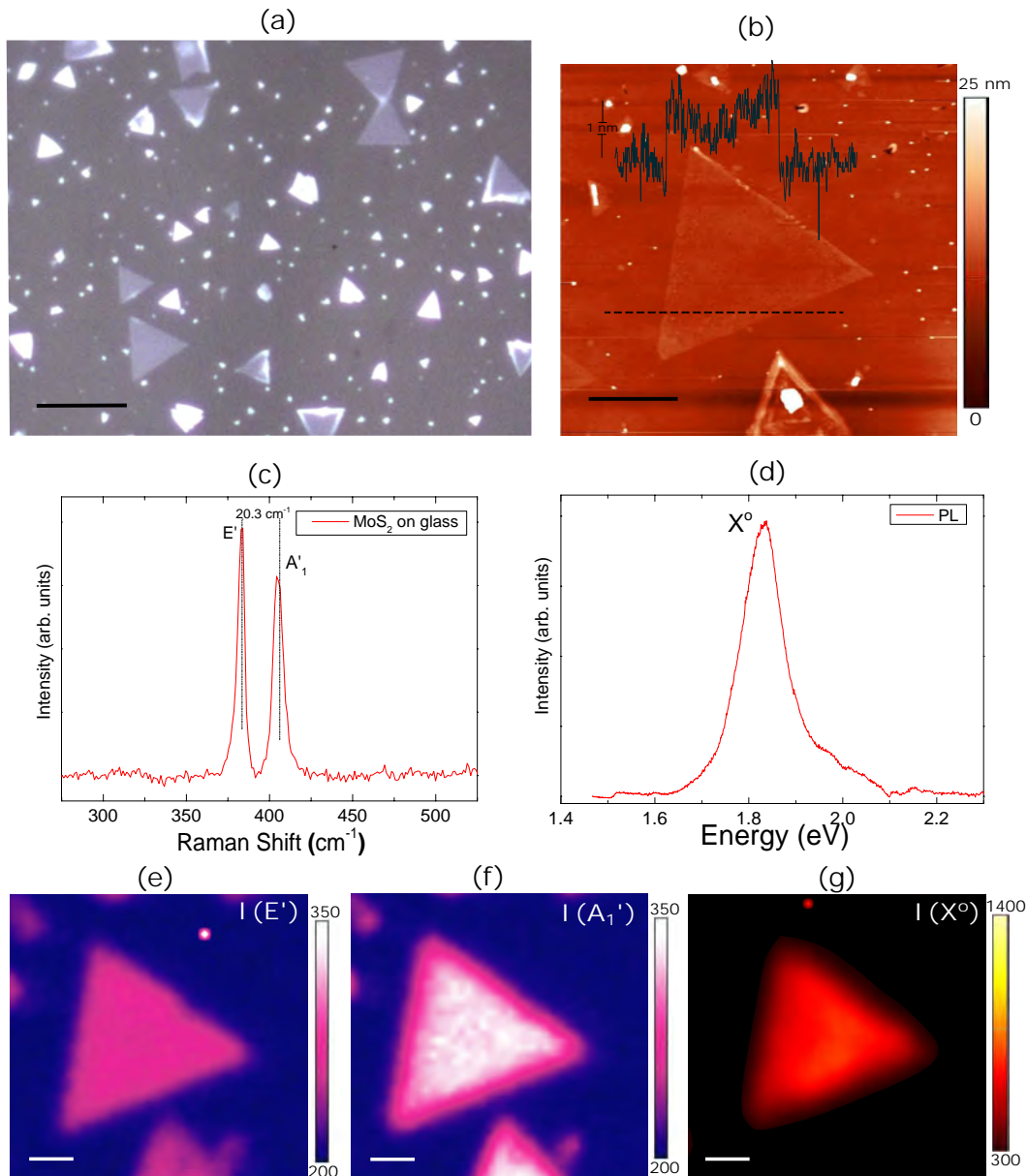


Figure 4.15: (a) Optical image MoS₂ on glass scale bar is 10 μm. (b) AFM image of a monolayer triangle with height of ~ 1 nm scale bar is 2 μm. (c) Raman and, (d) PL spectra of the corresponding triangle. (e) Intensity map of E', (f) A₁' modes of the same triangle. (g) PL intensity map.

glass. Monolayer triangles can be easily identified because of larger in size and lighter color contrast compared to its counterpart. The triangles were further confirmed as monolayer by AFM, Raman, and PL spectroscopy. The AFM image of the corresponding triangle is shown in figure 4.15(b) showing a uniform surface with average height is estimated to be around ~ 1 nm which corresponds to monolayer. A small variation in height of about 3 Å is likely due to the roughness of glass because glass is not as smooth as SiO₂ substrate. Representative Raman spectrum obtained from the same monolayer MoS₂

triangle is shown in figure 4.15(c). The recorded raman spectrum exhibited the characteristic in-plane phonon mode E' and the out-of-plane A₁' modes at 386.3 cm⁻¹ and 406.6 cm⁻¹. The difference in peak position between these modes is 20.3 cm⁻¹. The Raman mapping of the same triangle is also recorded by scanning all over the triangle. The peak intensity map of E' and A₁' modes is shown in figure 4.15(e,f). The E' mode has uniform intensity throughout the triangle. The A₁' mode shows a brighter color at the center, while at the corners the intensity is lower which is most likely due to the edge effect [179]. The tensile strain in the outer region is stronger than that of the inner region hence effecting the intensity. These maps are evidence of uniform structural quality of the crystal.

Figure 4.15(d) shows the PL spectrum of MoS₂ triangle on glass substrate, which exhibits a single sharp peak located at 1.85 eV confirming the direct band. Furthermore, the PL mapping of the corresponding triangle also indicates uniformity at PL emission see figure 4.15(g). The uniform colour intensity overall triangle is an indicator of the uniform thickness. All the maps clearly demonstrate that this entire MoS₂ crystallite is a uniform monolayer triangle. More studies are needed on glass synthesis to achieve all monolayer triangles. One way is to use the glass substrate with low Na concentration so that the rate of growing multilayer could be decreased.

4.6 Partial Conclusion

Reliable direct synthesis atmospheric pressure CVD methods were proposed to grow monolayer MoS₂, WS₂, and their vertical heterostructure. A number of initial attempts were unsuccessful. The most likely reasons were the wrong positions of the substrate, mixing of the crucible, amount of precursor and temperature, etc. For each TMD separate crucible and quartz tube should be used. Initial attempts at WS₂ were done similarly to the MoS₂ procedure and there was no appreciable growth, because of very poor WO₃ evaporation. All the samples were further characterized by AFM, Raman, and photoluminescence spectroscopy showing the best crystalline quality and direct bandgap in all.

We introduced a new technique of low-temperature atmospheric pressure CVD synthesis of monolayers of MoS₂. We have grown single crystals and polycrystal films using sodium as catalytic. From DFT calculations and experiments, we found the ideal synthesis parameters of precursor ratio 0.3 and synthesis temperature of 550°C. The DFT calculation also shows that the critical element is the number of sodium in the system, which reduces the

energy formation and allows to use a reduced temperature ($\Delta T = 250^\circ\text{C}$). Single and polycrystalline monolayers can be achieved by controlling the growth time. The XPS spectra after the bath show that the sodium could not be found in the crystal lattice. The AFM, Raman, and photoluminescence spectroscopy has established it as a monolayer with a direct bandgap and has a low density of defects. The optical and electrical experiments show that the grown samples have properties comparable to those produced at a higher temperature at any arbitrary substrate. The new technique will help to synthesized directly on a transparent substrate, allowing the low-cost and high-quality synthesis of these semiconducting material. This work would serve as a reference for the low-temperature synthesis of other TMDs.

5

Second Harmonic Generation in Two and Three Layers of Transition Metal Dichalcogenides

This chapter includes the characterization of two and three layers of TMDs having different crystal orientations. The numbers of layers were confirmed by Raman and PL spectroscopies. Finally, the non-linear optical properties (second and third harmonic generation) of two and three layers MoS₂, WS₂, and MoS₂/WS₂ samples. The second harmonic shows that the layers grow with different crystal orientations (0° or 60°) have different phase stacking.

5.1

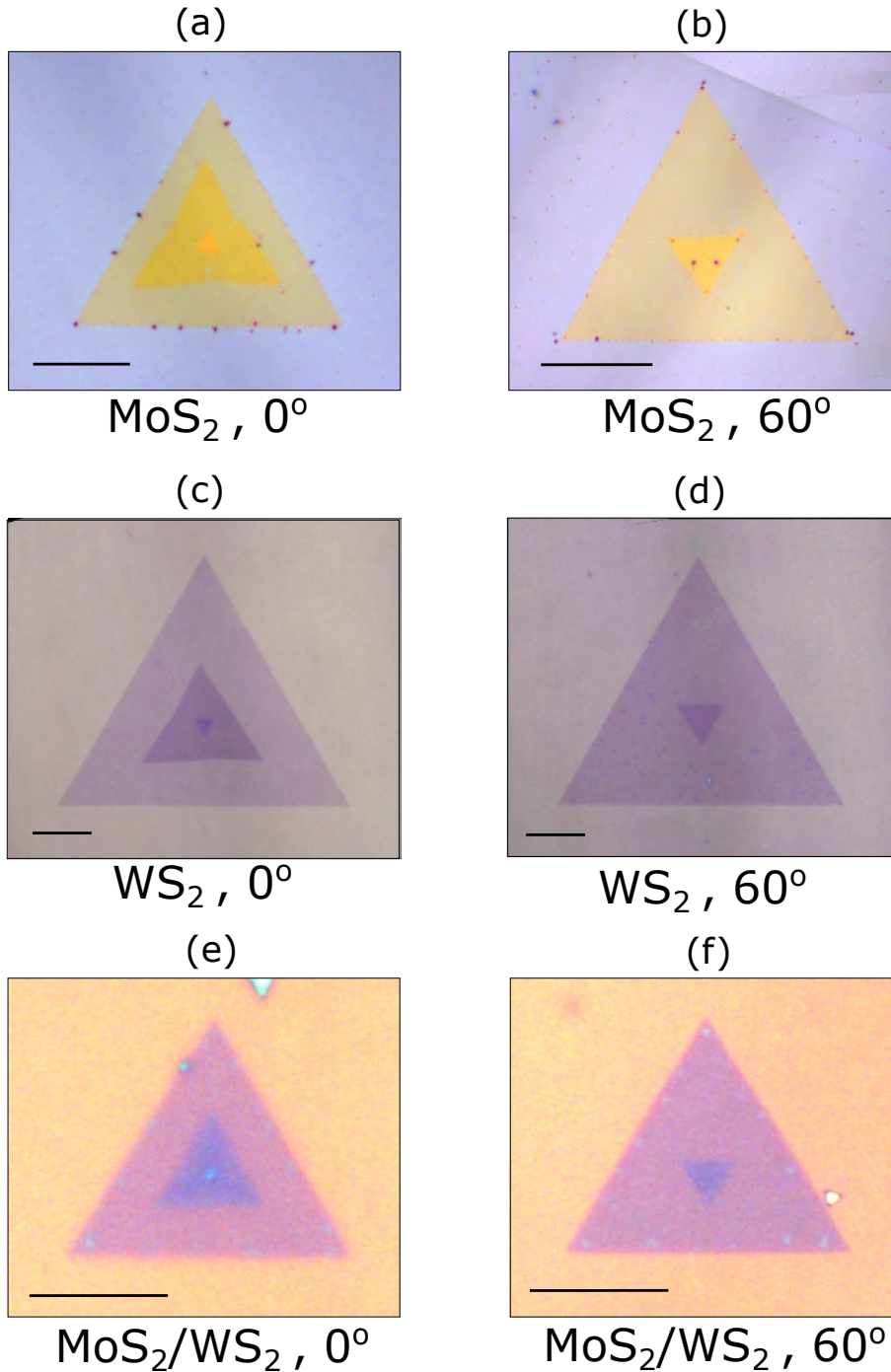
Introduction

After the consistent growth of monolayer triangular islands, the next challenging task was to grow uniform layered triangles. It can be seen in figure 4.1(a) the triangles formed had a very clear nucleation site visible in the centre of the triangle and even some with growth occurring off that nucleation site presenting the beginning of a second layer. The second layer is somehow easy to grow but difficult to control. We report the atmospheric pressure chemical vapor deposition synthesis of two and three layers of MoS₂ and WS₂. The APCVD synthesis of bilayer TMDs is explained (chapter 3 see section 3.1.4). However, controlling the growth of bilayer or multiple layers is still challenging. CVD synthesis of bilayers gives us the samples with different phase stacking between the top and bottom layers i.e 0° or 60° (see figure 5.1). The stacking sequence in TMDs can significantly impact on their electrical and optical properties due to its effect on the electronic band structure [91]. Second harmonic generation is a useful technique to study the stacking sequences [62]. We use second and third harmonic generation to characterize our bilayers and trilayers samples.

5.2

Two and Three Layers of Transition Metal Dichalcogenides

The optical images of the as-grown bilayer and trilayer MoS₂, WS₂, and their vertical heterostructures are shown in figure 5.1. In figure 5.1(a,c) we have three layers which make these samples more interesting. Figures 5.1(a,b) show



PUC-Rio - Certificação Digital N° 1622346/CA

Figure 5.1: Optical microscopy image of the as-grown (a) MoS_2 trilayer stacked with same crystal orientation between each layer scale bar is $20 \mu\text{m}$ (b) MoS_2 bilayer stacked with opposite crystal orientation to the monolayer (c) WS_2 trilayer first two triangles are stacked with same crystal orientation while the third triangle is stacked with 60° w.r.t other layers scale bar is $10 \mu\text{m}$ (d) WS_2 bilayer stacked with opposite crystal orientation (e) MoS_2/WS_2 heterostructure stacked at 0° and (f) 60° , scale bar is $10 \mu\text{m}$.

the optical images of the as-grown trilayer and bilayer MoS_2 crystals. Figure 5.1(a) shows a trilayer crystal with the 0° crystal orientation. The second and third layers are at the centre, and they are smaller than the first layer. Figure

5.1(b) present a stacked bilayer with a twisted angle of 60° , on which the larger triangle refers to the monolayer, and the triangle inside it is a bilayer region. Figures 5.1(c,d) show the optical images of WS_2 trilayer and bilayer crystals. In figure 5.1(c) shows a trilayer crystal with the first two layers have 0° crystal orientation while the second and the third layers are 60° oriented. In figure 5.1(e,f) we have as-grown MoS_2/WS_2 heterostructures with 0° and 60° orientation. The different colour contrast arises due to the difference of SiO_2 thickness on the Si substrate [182]. These samples were grown over a period of time, there is no specific reason for different substrates, the substrates were chosen randomly depending on easily available substrate in our laboratory. The SiO_2 thickness does not affect the growth process, it only contributes while the characterizations of the sample. For example, Raman intensity strongly depends on the oxide thickness so as the SHG intensity [183,184].

5.3

Raman and Photoluminescence of Trilayer Samples

Figure 5.2(a) depicts the Raman spectrum obtained from MoS_2 triangle shown in figure 5.1(a). The recorded Raman spectrum exhibited the characteristic in-plane phonon mode E_{2g}^1 and the out-of-plane A_{1g} mode. As the triangle thickness is increased the frequency of the E_{2g}^1 mode decreases (redshifts) while the A_{1g} increases (blueshifts). The difference in peak position between these modes in the largest triangle is 20 cm^{-1} corresponds to monolayer sample [166]. The frequency difference for the middle triangle is 23 cm^{-1} which corresponds to bilayer, and for the smallest triangle, it is 24.8 cm^{-1} which corresponds to trilayer [185]. This frequency-dependence shift can identify the ultrathin MoS_2 thickness for monolayer to four layers [44]. The photoluminescence of the three layers is also given in figure 5.2(b). The monolayer PL spectrum exhibits a single emission peak, with a maximum at a photon energy of $\sim 1.86 \text{ eV}$. By increasing the number of layers, the PL intensity decreases a lot, and the maximum of the PL shifts significantly to low energy.

Figure 5.3(a) presents the Raman spectra for one, two, and three-layers of WS_2 triangle shown in figure 5.1(c). The intensity ratio of $L A/A_{1g}$ and peak position difference can be used to identify the number of layers [45]. The most substantial ratio indicates the monolayer. Moreover, the first order in-plane mode E_{2g}^1 shows redshifts and the out-of-plane A_{1g} shows blueshifts while increasing the number of layers. The difference in peak position between them in the largest triangle is 61.1 cm^{-1} , for the middle triangle is 63.2 cm^{-1} , and for the smallest triangle, it is 64 cm^{-1} which is the confirmation of monolayer, bilayer and trilayer regions [45,186]. Figure 5.3(b) shows the

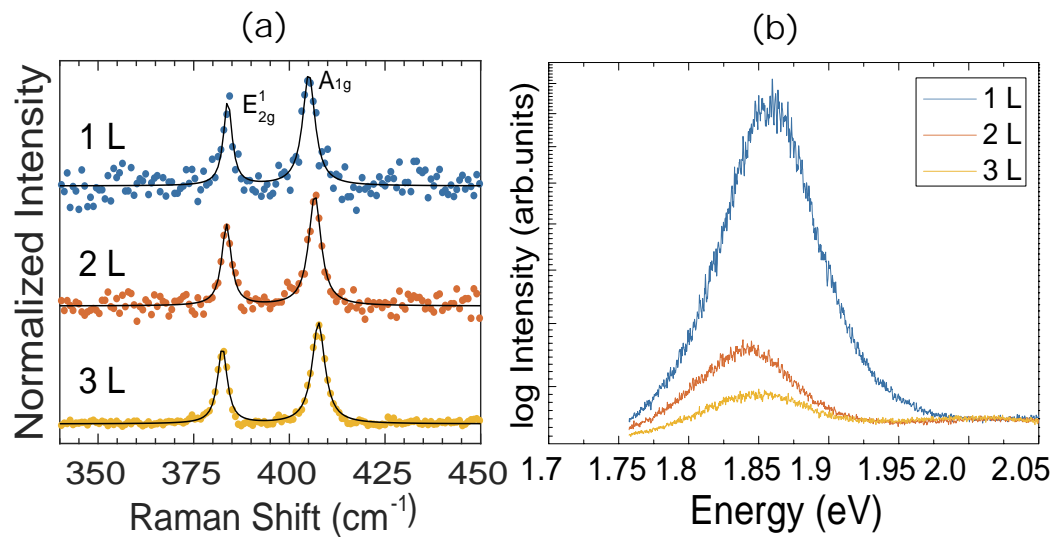


Figure 5.2: (a) Raman spectra of MoS₂ trilayer stacked with same crystal orientation between each layer shown in figure 5.1(a). (b) Log of photoluminescence intensity of the three layers, decrease in intensity refers to shifting towards indirect band gap.

photoluminescence from the three layers. The PL shows a sharp peak at ~ 2.02 eV for the biggest triangle i.e monolayer. As the number of layers increases the PL shifts to lower energies and the intensity decreases drastically [187]. This layer dependent photoluminescence in MoS₂ and WS₂ is a result of direct-to-indirect transition [105].

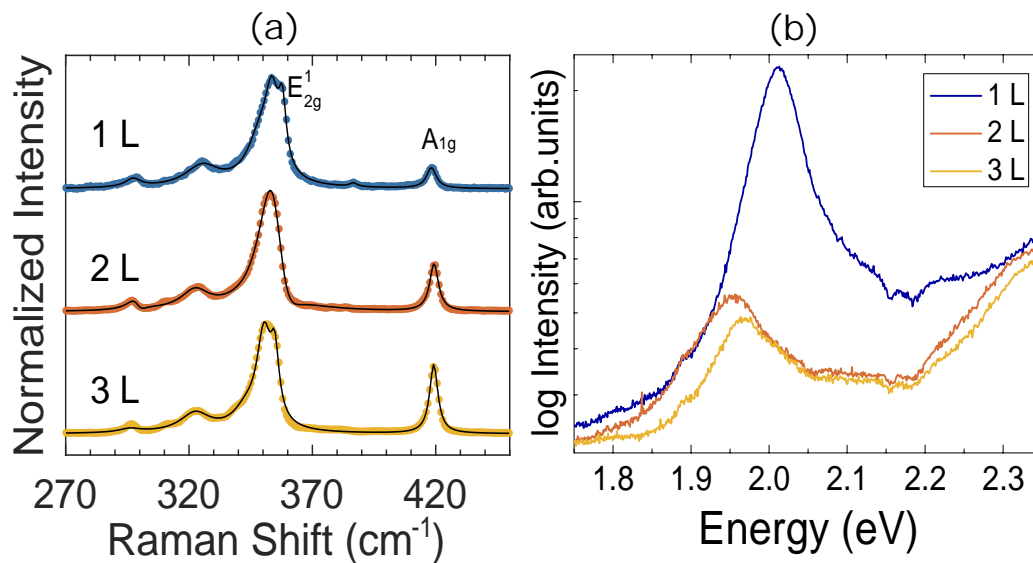


Figure 5.3: (a) Raman spectra of WS₂ trilayer shown in figure 5.1(c). (b) Log of photoluminescence intensity of the three layers.

Direct bandgap in MoS₂ and WS₂ depends on the localized d-orbital of the Mo/W atom. Which are not much affected by the inter-layer coupling due to its location in the unit cell. While indirect bandgap in these materials depends on the overlap of d-orbital of the Mo/W atom and p_z orbital of the S atoms which strongly depends on inter layer coupling. Thus, as the number of layers is decreased the intrinsic direct bandgap of the material becomes more pronounced. While the band gap broadening in the monolayer is attributed to quantum confinement of charge carriers, common in nanosystems [104].

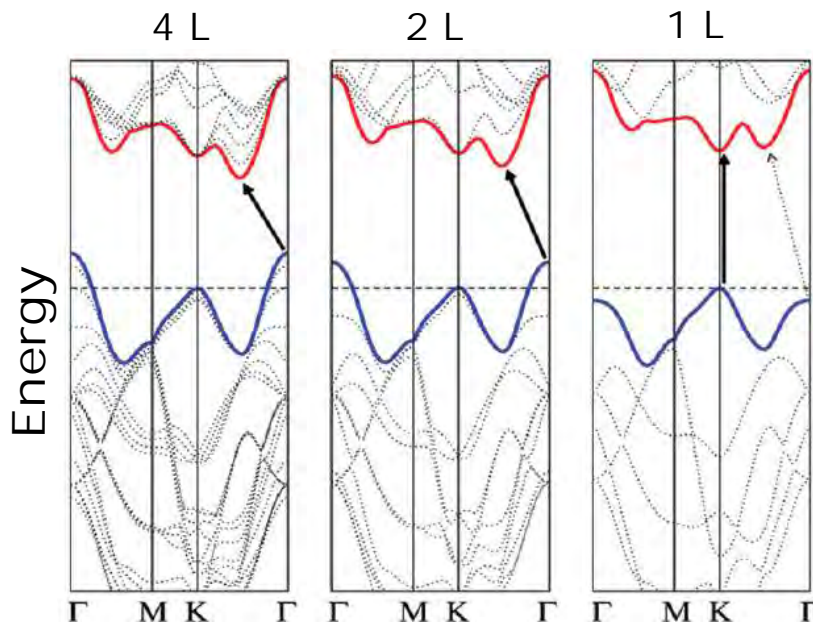


Figure 5.4: Band gap of 4L, 2L, and 1L of MoS₂ calculated by Splandani et al. [9]. The solid arrows indicate the lowest energy transitions. The direct excitonic transitions occur at high energies at **K** point in the Brillouin zone. With reduced layer thickness, the indirect bandgap becomes larger, while the direct excitonic transition barely changes. For monolayer MoS₂, it becomes a direct bandgap semiconductor. This dramatic change of electronic structure in monolayer MoS₂ can explain the observed jump in monolayer photoluminescence efficiency.

This transition bandgap behaviour was explained by Splandani et al. [11]. They did the DFT calculations for few layers MoS₂ see figure 5.4. It can be seen that the direct excitonic transition energy at **K** point in the Brillouin zone hardly changes with layer number. But the indirect bandgap see increasing in energy as the number of layers decreases. The indirect transition energy becomes so high in monolayer MoS₂ and it eventually becomes a 2-D direct bandgap semiconductor. With the increase of the indirect bandgap in thinner MoS₂, the intraband relaxation rate from the excitonic states decreases, and the photoluminescence becomes stronger.

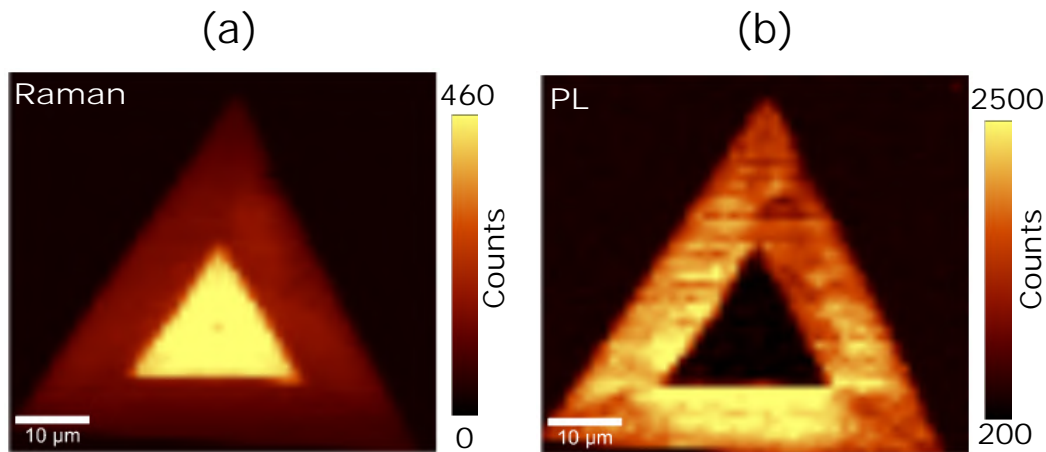


Figure 5.5: (a) Raman and (b) PL mapping images of the WS_2 trilayer shown in figure 5.1(c).

The Raman and PL maps of the WS_2 triangular flake (shown in figure 5.1(c)) are also given in figure 5.5(a). It can be seen the Raman intensity is uniform over the area and in the bilayer region the intensity increases, while there is a minor change in the intensity of bilayer and trilayer regions. The PL intensity map of the same triangle is given in figure 5.5(b). The PL intensity decreases at the bilayer, compared to monolayer as expected. The Raman and PL of MoS_2/WS_2 heterostructure has already been discussed in chapter 4 (see section 4.3).

5.4

Second Harmonic Generation in Two and Three Layers of MoS_2 , WS_2 with Different Stacking Orientation

Three sets of bi-layer samples MoS_2 0° and 60° , WS_2 0° and 60° and MoS_2/WS_2 0° and 60° (see figure 5.1) were chosen for nonlinear optical characterization (SHG and THG). The 1560 nm Erbium-doped fiber laser with a pulse duration of 150 fs was used as an incident laser, experimental setup has been discussed in chapter 3 (see section 3.8).

Figure 5.6 shows spectra from MoS_2 flake in figure 5.1(a) which depicts prominent peaks at ~ 780 nm, which represents the exact frequency doubling signal (SHG) from the 1560 nm (Erbium-doped fiber laser). This indicates that the signals are generated through a second-order nonlinear process in MoS_2 flake. Similarly, peaks at ~ 520 nm indicate third-harmonic signals are observed from MoS_2 flake in figure 5.1(a). The second harmonic generated signals from the three regions of MoS_2 flake show the monolayer has the lowest intensity and trilayer has the highest intensity. The SHG signal from the monolayer area

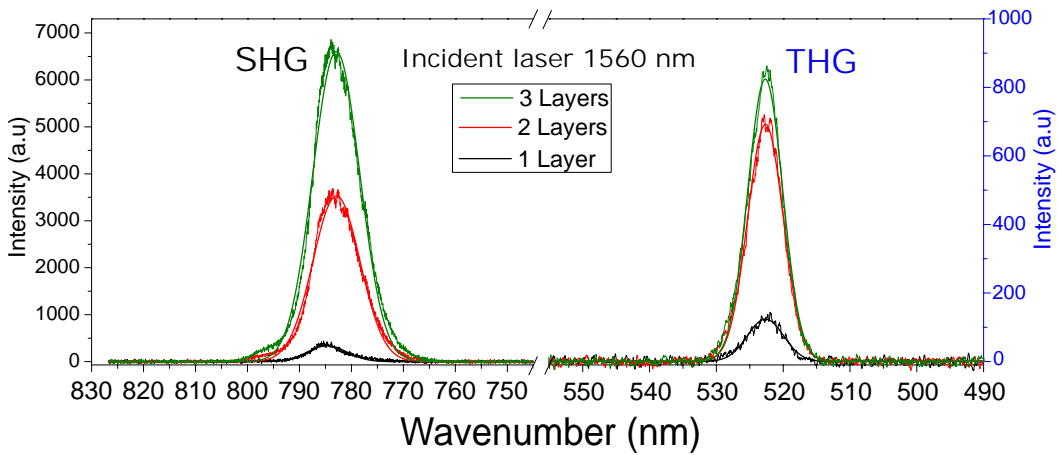


Figure 5.6: Single spectra of MoS₂ flake shown in figure 5.1(a), showing second-harmonic and third-harmonic signals.

of 60° sample (figure 5.1(b)) is equal monolayer area of 0° sample. However, the SHG is not observed in bilayer area of 60° sample. Similar trend is followed by the third harmonic generation by trilayer sample but the THG signal is very weak as compared to SHG. However, THG is observed in bilayer area of 60° sample.

The polarization dependence of the SHG signals was also studied. Polarization angle θ is defined as the angle of the electric field direction of the incident laser with respect to the long axis of the sample. SHG is very sensitive to the crystal symmetry. Hence, polarization resolved SHG measurements provide important crystallographic information of TMDs atomic layers [188].

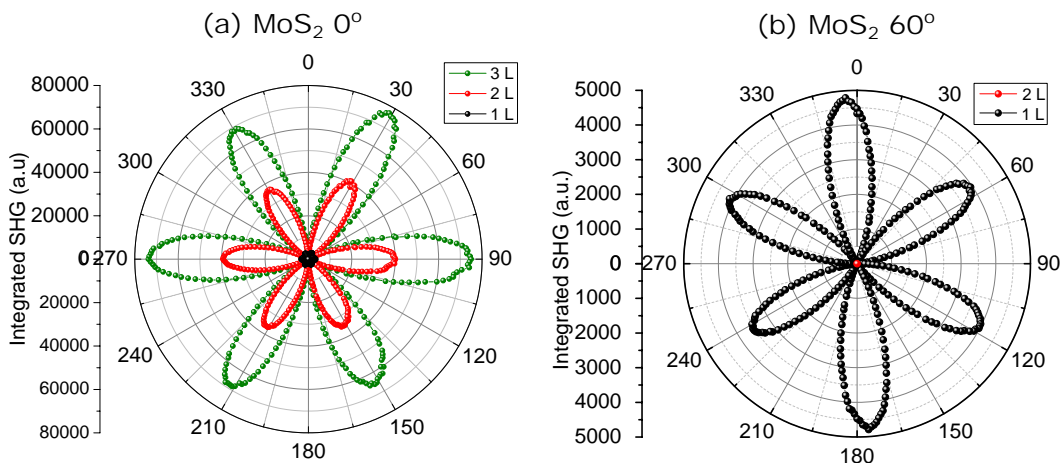


Figure 5.7: Intensity dependence of the SHG signal with the polarization angle. (a) Trilayer (green) with a twisted angle of 0° between bilayer (red) and monolayer (black). (b) bilayer (red) twisted 60° from monolayer (black).

Second harmonic generation was measured at polarization angles from 0° to 360° with a step of 1° . Each spectrum was fitted with a gaussian and intensity is estimated. Figure 5.7(a,b) present the SHG intensity as a function of the polarization angle, obtained from crystals in figure 5.1(a,b). The polar graphs show the polarization dependence with the six-fold pattern.

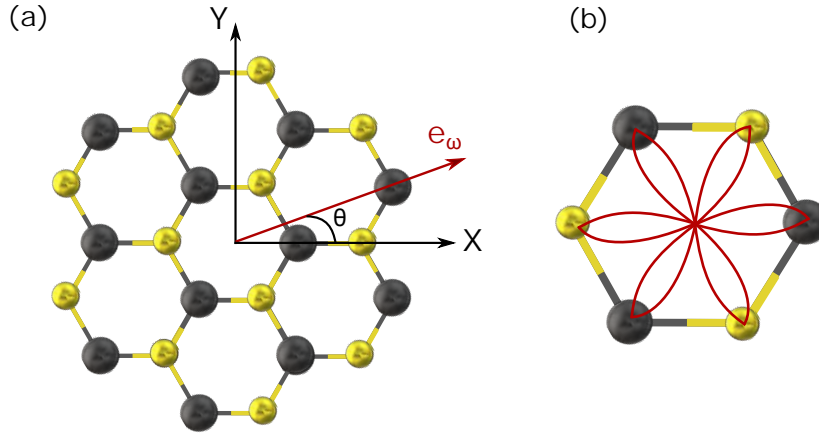


Figure 5.8: Schematics of (a) Top view of the MoS₂ crystallographic orientation with respect to the incident laser polarization e_ω . (b) Orientational dependence of SHG.

The flower-like six petals polarization dependence is due to the D_{3h} symmetry of the MoS₂ monolayer. Since MoS₂ has hexagonal crystal symmetry, the electron cloud oscillates (due to external electric field) as a function of angle θ . Hence, generating a graph with periodicity of 60° . Figure 5.8 is a sketch of a top view of hexagonal MoS₂, showing the angle of the crystallographic orientation to the incident laser polarization direction e_ω [51, 189].

D_{3h} symmetry group gives only one independent nonvanishing element of the nonlinear response i.e:

$$\chi^{(2)} = \chi_{xxx}^{(2)} = -\chi_{xyy}^{(2)} = -\chi_{yyx}^{(2)} = -\chi_{yxy}^{(2)} \quad (5-1)$$

where x corresponds to the armchair direction and y is the zigzag direction (see figure 5.8). The electric field of the generated second harmonic signal $E(2\omega)$ along a given direction $e_{2\omega}$ can be described in terms of $\chi^{(2)}$ and input light polarization vector e_ω as:

$$E(2\omega).e_{2\omega} = C e_{2\omega} \cdot \chi^{(2)} : e_\omega e_\omega \quad (5-2)$$

here 2ω is the second harmonic frequency, ω is the incident laser frequency, and C is constant (local-field factors determined by the local dielectric environment). For a laser polarization perpendicular or parallel to the polarization of the input laser, the generated second-harmonic electric field is expressed as [50, 190]:

$$E_{\perp}(2\omega) = C\chi^{(2)}\sin(3\theta + \theta_o) \quad (5-3)$$

or

$$E_{\parallel}(2\omega) = C\chi^{(2)}\cos(3\theta + \theta_o) \quad (5-4)$$

where θ is the angle between the input laser polarization and the x direction, θ_o is the initial crystallographic orientation of the sample. Since intensity is proportional to the square of the electric field ($I_{nt} \propto |E|^2$). Therefore, the intensity of the generated SHG is proportional to $\cos^2(3\theta + \theta_o)$ or $\sin^2(3\theta + \theta_o)$, giving six-fold polarization dependence.

By obtaining the polar plots it is possible to analyze the relationship of intensity of the layers and the phase angle between them.

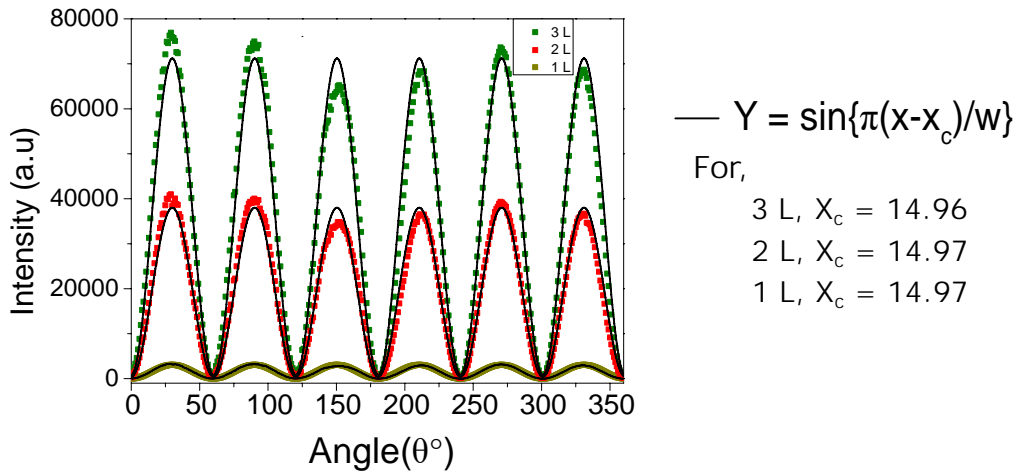


Figure 5.9: Polarization plot shown in figure 5.7(a), fitted with a sine wave function (black line) showing no phase difference between each layer.

Each polarization plot was fitted using a sine function with a period of 60° . Figure 5.9 presents the polarization plot shown in figure 5.7(a) along with the fitted sine wave function. These fittings gives us the phase difference between each layer. Table 5.1 shows the SHG intensity normalized by the monolayer and phase difference for two and three stacking MoS₂ layers with 0° and 60° twisted angle. We observed an enhancement of SHG intensity, for the bilayer with 0° , the value is ~ 12 times, and for trilayer is ~ 23 times higher than the monolayer intensity. The observed SHG increase is around four times higher than expected, most likely due to the perfect stacking of two layers in CVD growth [62]. For the 60° twisted angle, the SHG signal at the bilayer region is inhibited due to inversion-symmetry. The phase near 0° shows that the layers are aligned. Figures 5.10(a,b) show the schematics of relative stacking orientation of the top and bottom layers. In the 3R(AB) phase, our 0° bilayer and trilayer MoS₂, the metal atom is located at the centre of the bottom

hexagon. Thus we have a no-inversion symmetry and the SHG is present. In the 2H(AA') phase, our 60° bilayer MoS₂, the stacking of metal atom of the second layer sits precisely on top of the chalcogen atom of the bottom layer and shows the inversion symmetry and therefore no SHG signal [88,94]. The simple approach can explain qualitatively the absence of second-harmonic generation in 60° bilayer MoS₂, due to the presence of inversion symmetry the χ_2 tensor is equal to zero.

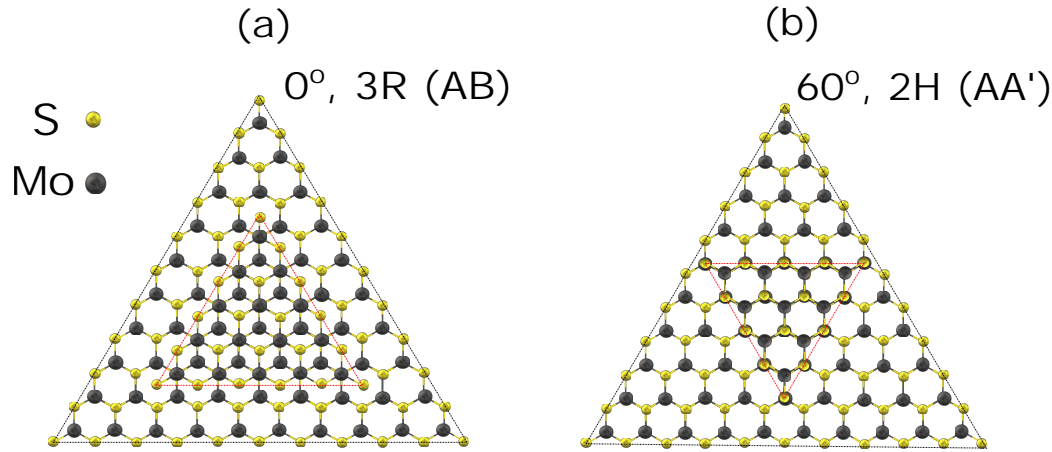


Figure 5.10: Schematics of relative stacking orientation of the top and bottom layers. (a) 3R(AB) phase, the metal atom is located at the center of the bottom hexagon. Thus has a no-inversion symmetry. (b) 2H(AA') phase, the metal atom of the second layer sits precisely on top of the chalcogen atom of the bottom layer, has the inversion symmetry.

Generally, even number of MoS₂ layers is known to have no SHG (even number of layers have inversion symmetry) [122], but it can be generated in an odd number of MoS₂ layers (no-inversion symmetry) [50–52]. Here, we have shown that CVD grown bilayers of MoS₂ could possess two types of stacking (i.e 2H and 3R) and could have inversion or no-inversion symmetries.

The polarization dependent third harmonic generation (THG) for these flakes were also studied. Third harmonic generation was measured at polarization angles from 0° to 360° with a step of 5°. In contrast to SHG, the THG is polarization independent, as can be seen from figures 5.11(a,b). The THG intensity increases with the number of layers [124]. As the thicker sample has longer light-matter interaction length. Also, we have THG in bilayer MoS₂ 60° sample, as it is not tied to the condition of non-centrosymmetry.

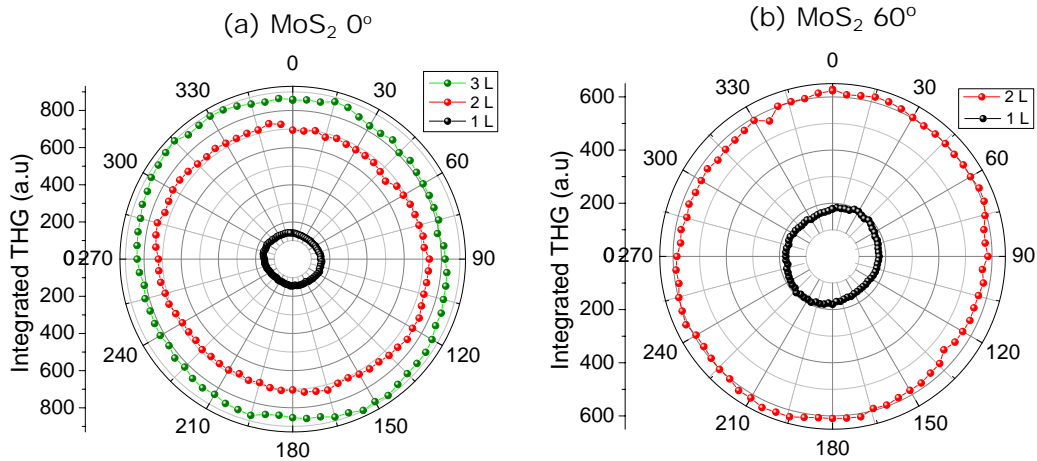


Figure 5.11: THG, constant intensity with θ (a) Trilayer MoS₂ shown in figure 5.1(a) (b) Bilayer MoS₂ shown in figure 5.1(b).

Figure 5.12(a,b) present the polarization plots of the nonlinear optical response for WS₂ trilayers and bilayers crystals shown in figure 5.1(c,d). We observed, once more, the six-fold pattern. The bilayers with 0° and 60° show similar behaviour compared with MoS₂ crystals. However, the top layer of the trilayer crystal is rotated 60°. The measurements also provided the possibility to verify the phase difference of the signal in each region, which could be caused by rotation between the layers.

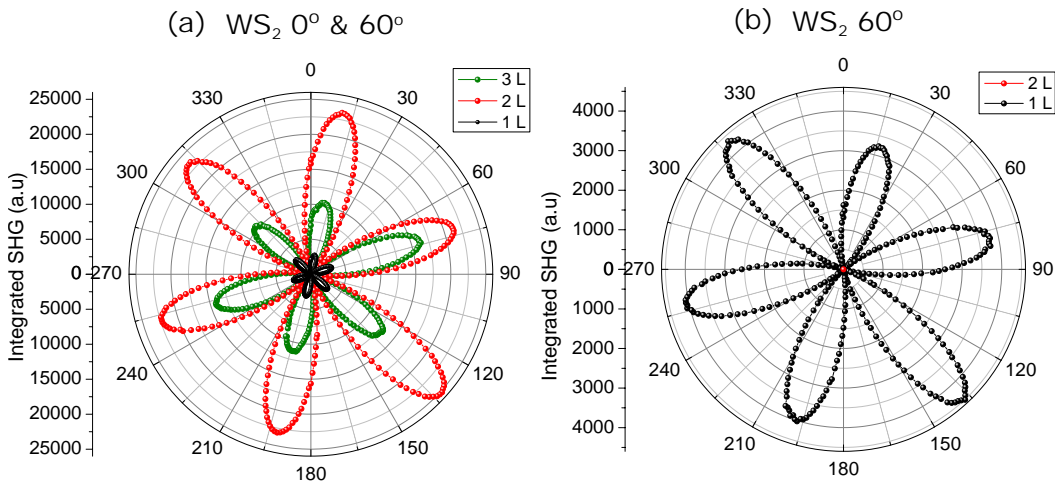


Figure 5.12: Intensity dependence of the SHG signal with the polarization angle. (a) Trilayer (green) with twisted angle of 0° between bilayer (red) and monolayer (black). (b) bilayer (red) twisted 60° from monolayer (black).

Table 5.1 shows the normalized SHG intensity and phase of bi and trilayer

of WS_2 . For bilayers with a twisted angle at 0° , the SHG intensity is ~ 7.7 times higher than the monolayer. For the trilayer region, we observed a reduction of SHG intensity, probably due to the inversion of symmetry generated by the top layer. In the crystals with 60° figure 5.1(d), it is not possible to detect the SHG signal, due to the centrosymmetry, and therefore eliminating second-order nonlinearities. By fitting the sine wave on the polarization plot in figure 5.12 it is confirmed that the WS_2 sample did not show rotation between its layers.

5.4.1

SHG in MoS_2/WS_2 Heterostructure with Different Stacking Orientation

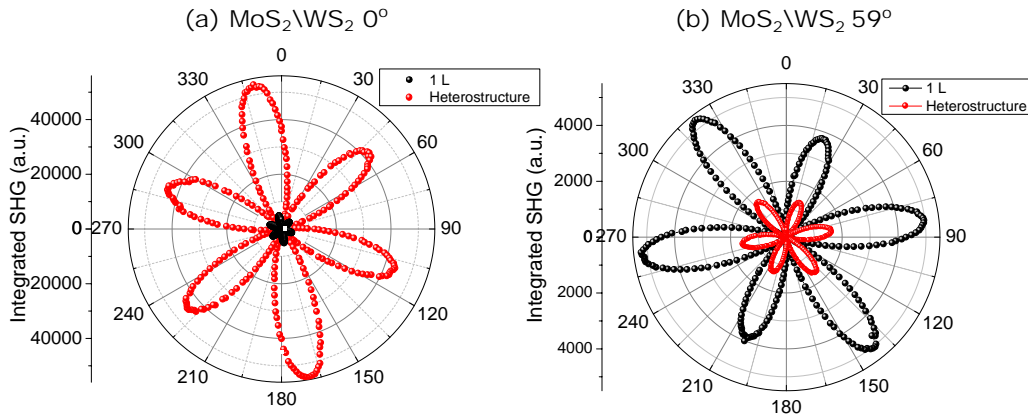


Figure 5.13: Intensity dependence of the SHG signal with the polarization angle. (a) MoS_2/WS_2 heterostructure 0° . and (b) MoS_2/WS_2 heterostructure 59° .

The SHG from MoS_2/WS_2 heterostructure samples (Figure 5.1(e,f)) was also measured. Figure 5.13(a,b) presents the polarization dependence of the SHG signal of heterostructure. The extinct rotational symmetry was observed in both graphs. In addition, the relationship between the intensity of SHG in the heterostructure and the intensity in the monolayer showed SHG signal is ~ 10 times higher in bilayer region than the monolayer [191].

In contrast to the same bilayer MoS_2 and WS_2 60° samples, heterostructure 60° sample produced a SHG signal but have very low intensity compared to monolayer, see figure 5.13(b). The sine function with a period of 60° is fitted to calculate the phase difference between each layer. For heterostructure 0° the phase difference is 0° between two layers but for 60° heterostructure the alignment is not exact, there is a phase difference of $\sim 1^\circ$. Since the phase difference between the two layers could result in SHG. To confirm our observation we took another heterostructure 60° crystal with 0° phase difference and

measured the polarization dependence of SHG again. Once again we observe SHG (figure 5.14). This is due to the presence of two different materials (i.e Mo and W), the complete cancellation of the SHG signal is not possible (there are not the same materials to generate exact inversion symmetry).

Figures 5.15(a,b) show the schematics of relative stacking orientation of the top and bottom layers of MoS₂/WS₂ heterostructure samples. Heterostructure possesses the same 2H and 3R phase stacking as bilayer MoS₂ and WS₂ did, but the different masses of W atom (top layer) and Mo atom (bottom layer) is responsible for SHG in 2H stacked heterostructure. This behaviour of SHG can be explained as the interference of two electromagnetic waves.

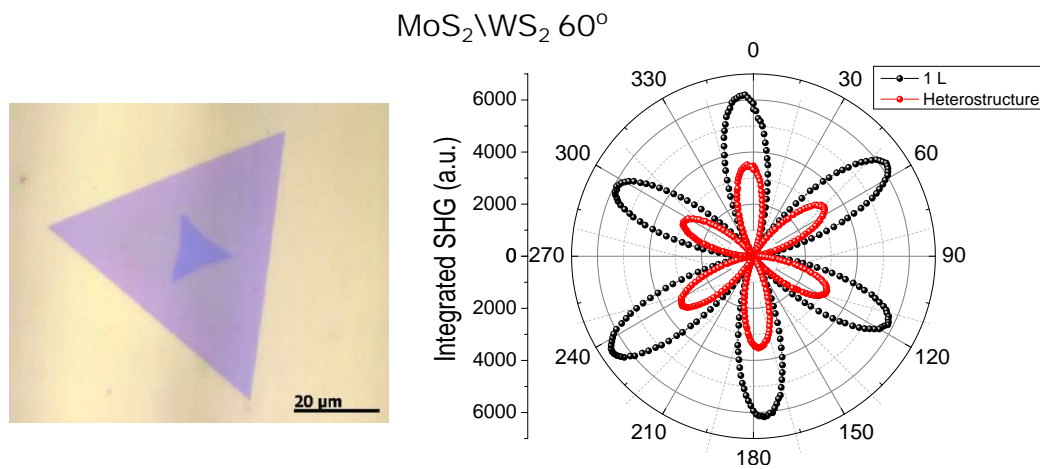


Figure 5.14: Optical image of MoS₂/WS₂ heterostructure 60°, and its intensity dependence of the SHG signal with the polarization angle.

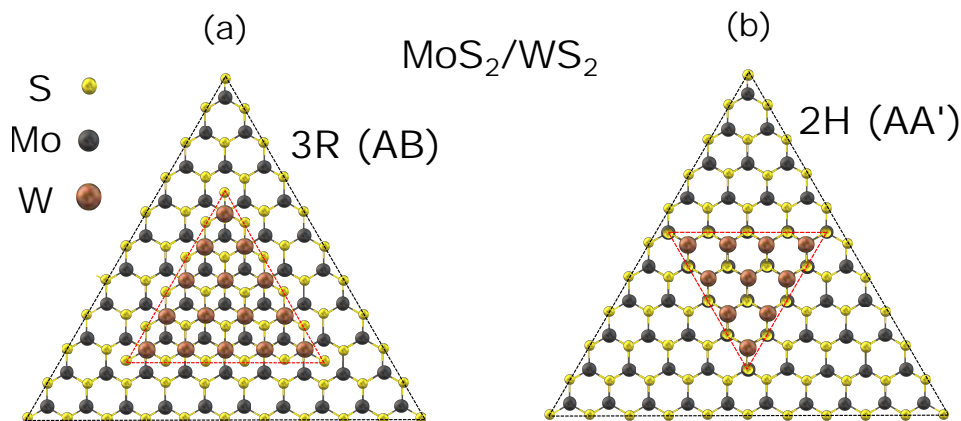


Figure 5.15: Schematics of relative stacking orientation of the top and bottom layers. (a) MoS₂/WS₂ 0°. (b) MoS₂/WS₂ 60°, mismatch between the masses of Mo and W atoms results in SHG.

Stacking	Normalized SHG Intensity	Phase
0° Bilayer MoS ₂	12.3 ± 1.2	0.0 ± 0.2°
0° Trilayer MoS ₂	23.1 ± 2.2	0.0 ± 0.1°
0° Bilayer WS ₂	7.71 ± 0.07	0.0 ± 0.1°
60° Trilayer WS ₂	5.0 ± 0.2	0.0 ± 0.2°
0° MoS ₂ /WS ₂	10.0 ± 0.01	0.0 ± 0.2°
59° MoS ₂ /WS ₂	0.34 ± 0.5	1.0 ± 0.2°
60° MoS ₂ /WS ₂	0.51 ± 0.4	0.0 ± 0.2°

Table 5.1: Normalized SHG intensity and phase of TMD's.

5.4.2

Interference of Two S.H Fields

SHG from the two distinct layers can be considered as the superposition of two second harmonic fields, generated from two individual layers. The phase difference between them depends on the stacking angle between these two layers [62]. Consider these layers as electrically decoupled layers. The linearly polarized incident laser generates linearly polarized second harmonic fields from each layer, with a polarization direction determined by the angle between laser polarization and the armchair direction of each layer. If the incident laser electric field $E(\omega)$ makes an angle of θ_1 and θ_2 w.r.t the armchair direction of our triangles. Therefore, the generated second harmonic electric field will be $E_1(2\omega)$ and $E_2(2\omega)$ making an angle $3\theta_1$ and $3\theta_2$ from the laser polarization (equation 5-3). The total second harmonic electric field will be (figure 5.16).

$$E_T(2\omega) = E_1(2\omega) + E_2(2\omega) \text{ --- (vector superposition)} \quad (5-5)$$

since total intensity $I_T \propto |E_T|^2$ then squaring 5-5

$$|E_T(2\omega)|^2 = (|E_1(2\omega)|)^2 + (|E_2(2\omega)|)^2 + 2|E_1(2\omega)| \cdot |E_2(2\omega)| \quad (5-6)$$

$$|E_T(2\omega)|^2 = |E_1(2\omega)|^2 + |E_2(2\omega)|^2 + 2\sqrt{|E_1(2\omega)|^2 |E_2(2\omega)|^2} \cdot \cos 3(\theta_1 - \theta_2) \quad (5-7)$$

Replacing $|E|^2$ with I

$$I_T = I_1 + I_2 + 2\sqrt{I_1 I_2} \cdot \cos 3\theta \quad (5-8)$$

Here θ is the stacking angle between two layers and I_1, I_2 stand for the second harmonic intensity in layer 1 and layer 2;

Case 1 If $\theta = 0^\circ$ and $I_1 \approx I_2$ (each layer is generating S.H with the same intensity), Then from equation 5-8

$$I_T = 2I + 2I(+1)$$

$$I_T = 4I \text{ - - - - - (constructive interference)}$$

In case of bilayers MoS₂ and WS₂ with 0° stacking.

Case 2 If $\theta = 60^\circ$ and $I_1 \approx I_2$,

Then from equation 5-8

$$I_T = 2I + 2I(-1)$$

$$I_T = 0 \text{ - - - - - (destructive interference)}$$

In case of bilayers MoS₂ and WS₂ 60° stacking.

Case 3 If $\theta = 60^\circ$ and $I_1 \neq I_2$ (each layer is generating S.H with different intensities i.e when we have two different layers),

Then from equation 5-8, we must have SHG intensity.

That is the case of MoS₂/WS₂ 60° sample.

Also at any arbitrary angle except 60° the two layers will show SHG.

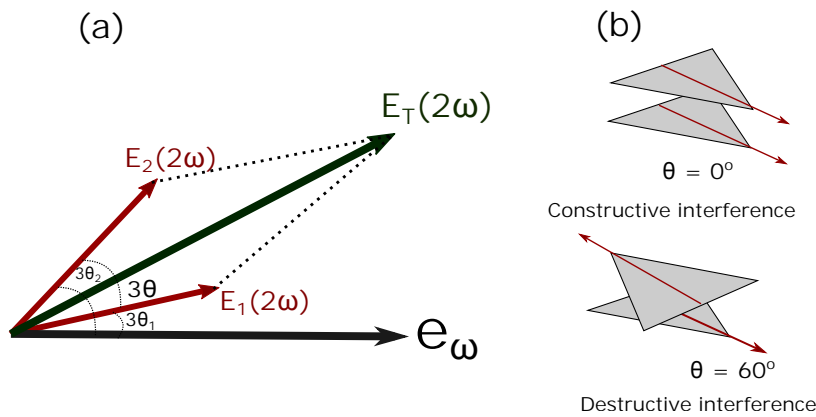


Figure 5.16: Schematic for illustrating the vector superposition of the second harmonic fields.

5.5 Partial Conclusion

We have grown a few layers of MoS₂ and WS₂ using chemical vapor deposition. The bilayer and trilayer crystals have 0° and 60° of the twisted angle. We used Raman and PL spectroscopies to characterized the crystals.

The optical properties of these materials confirmed their crystalline structure and thickness. The second harmonic generation was used to study the nonlinear properties of these layers. The SHG shows that the layers in bilayers grown with 0° have no inversion symmetry refers to 3R(AB) phase stacking. For 60° , we have an inversion symmetry (Centrosymmetric) and 2H(AA') phase stacking. These studies show that for CVD grown bilayer samples we can achieve both 2H(AA') and 3R(AB) phases. Moreover, the SHG from tri-layer MoS₂ and WS₂ crystals confirms our claim. The SHG keeps enhancing when all three layers are 0° stacked which referred to ABA stacking, if the third layer is replaced with 60° stacking concerning to the other two layers the SHG signal enhances in first two layers while blocked on the third layer, this referred to ABA' stacking. SHG is also observed in MoS₂/WS₂ 60° (2H stacking) due to difference of Mo and W masses. Such behaviour is explained as the interference of two electromagnetic waves.

6

Electrical Measurements

This chapter is devoted to the electrical performances of our CVD grown TMDs. Electrical performances were measured by fabricating two probe devices on them. It starts with the introduction and working of conventional field-effect transistors (FETs), including their working mechanisms and characteristics. This is then followed by the electrical measurements of our devices. Finally, devices were characterized by electro-Raman and the dependence of vibrational modes on gate voltage was studied.

6.1

Introduction

While studying the electro-optical properties of semiconducting TMDs, one question arises how the electro-optical properties of these materials change with the Fermi level. The Fermi level of TMDs can be tuned by applying a voltage across the material. This technique was used in order to tune the Fermi level of graphene [192–196]. The influence of the Fermi level, or carrier densities, on the optical properties of TMDs is also very important. In MoS₂ top gate field effect transistor configuration, Raman spectroscopy results show the dependence of vibrational mode with respect to the electron doping [81]. However, not much is known about the doping effect on vibrational modes of other TMDs. The influence of carrier density on the photoluminescence of monolayer MoS₂ was also observed [116]. TMDs based metal-oxide field effect transistors (MOSFETs) were deeply studied during the past decade. Not only monolayer TMDs but also their heterojunctions are considered useful for transistor applications [197–199]. These studies show a range of carrier mobilities, which is directly related to the quality of the TMDs.

The work intends to shed more light on the quality of our as-grown materials by electrical measurements. Especially our low temperature synthesized MoS₂ samples, how its carrier mobility differs from high temperature synthesized samples. Finally, the influence of electron doping (tuning the Fermi-level) on the vibrational modes of MoS₂/WS₂ heterostructure device.

6.2 Field Effect Transistor

Field effect transistor (FET) is a three terminals electronic device, widely used in digital integrated circuits. The three terminals are metallic electrodes i.e source, drain, and gate. FET uses a gate electrode potential V_G to control the conductivity of the semiconductor between the source and drain electrodes. The conduction path between drain and source is called a channel. In a FET, gate is practically separated from the entire body by a dielectric layer e.g SiO_2 . In particular, the field effect transistor (FET) works through the effect of an electric field in its active area. The dielectric of the device, which provides a medium for achieving electrostatic control of the channel by the gate, plays a very important role in influencing the performance of the device. Figure 6.1 shows a general structure of a field effect transistor.

6.2.1 Operating Principle of FETs

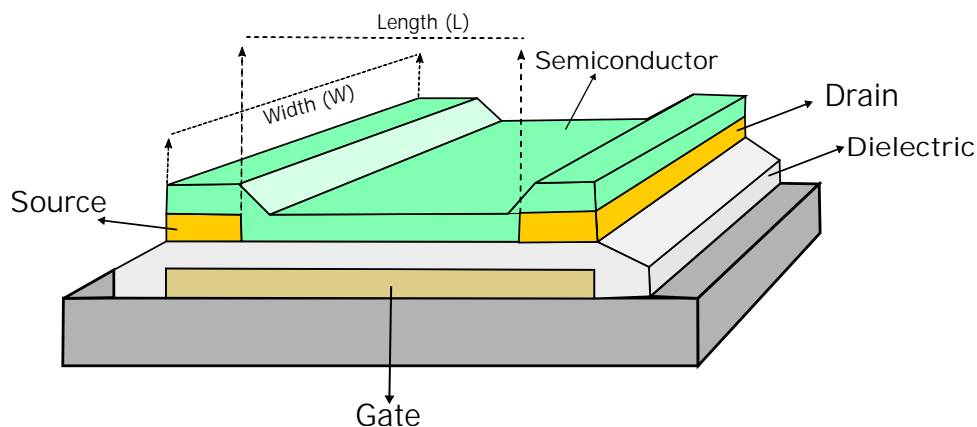


Figure 6.1: Illustration of the structure of a FET

The channel is the main part of a FET device, consisting of a thin semiconductor film sandwiched by two electrodes, the source (S) and the drain (D). The distance between the source and the drain is called length (L) of the channel. Width (W) of the channel is the area of a semiconductor touching the electrodes. A third electrode, called a gate electrode (G), is located along the channel, between the source and the drain. This electrode is isolated from the others and the semiconductor film by a thin dielectric film, see figure 6.1. Therefore, FETs are governed by two perpendicular and independent electric fields i.e potential difference generated by the gate electrode and the source electrode V_G , and the potential difference between the drain electrode and

the source electrode V_{DS} . This fact gives these devices a two-dimensional character.

A FET device is operated by controlling the V_{DS} potential and the V_G gate potential. Both V_{DS} and V_G simultaneously control the current between the drain and source I_{DS} . When a positive V_G is applied, electrons within the semiconducting channel are attracted by the gate, forming an inversion layer that enables charge carrier transport. When the applied gate voltage is larger than the threshold voltage V_{th} , the inversion layer connects the source and the drain, allowing conduction through the channel and thus switching on the transistor.

6.3 Device Structure

The structure of the devices considered in this work has a 1-3 nm thick TMDs (monolayer or bilayer). The devices were fabricated on p-doped SiO_2/Si substrate by lithography process as explained in chapter 3 see section 3.9. The p-doped silicon substrate serves as the global back gate and the SiO_2 as the dielectric [200]. The length of the channel ranges from 10 - 25 μm . The metallic electrodes source-drain thickness is taken as 50 - 80 nm and Cu/Au is used as the source materials. The schematic representation of our device is shown in figure 6.2(a). Figure 6.2(b) shows an optical image of a back gate FET device fabricated on an MoS_2 triangle.

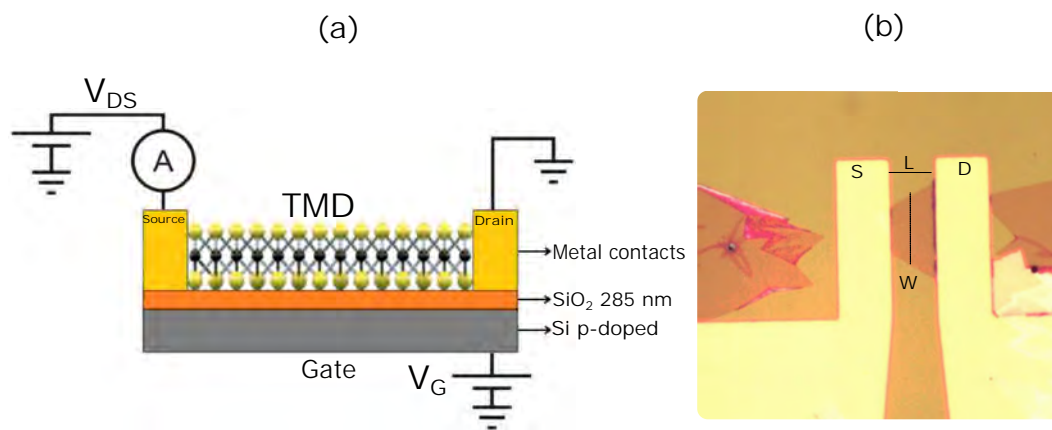


Figure 6.2: (a) Schematic representation of FET devices. (b) Optical image of a back gate FET device fabricated on SiO_2/Si , showing drain and source electrodes and channels L and W.

We have calculated the channel conductivity σ using the formula:

$$\sigma = \frac{L}{W} \frac{I_{DS}}{V_{DS}} \quad (6-1)$$

Here L and W are the length and width of the channel. Sheet conductivity is a normalized quantity which allows to compare samples and to extract quantities like field-effect mobility. This quantity does not take into account contact resistance but provides qualitative information on device behaviour. The electron mobility of the device is obtained by using the standard formula:

$$\mu = \frac{1}{C_o} \frac{L}{V_{DS}} \frac{\Delta I_{DS}}{W \Delta V_G} \quad (6-2)$$

The derivative in equation (6-2) is the maximum slope in the transfer characteristics. Where C_o is the gate capacitance and its value is

$$C_o = \frac{\epsilon_o \kappa_r}{d} \quad (6-3)$$

where

ϵ_o is permittivity of free space = $8.854 \times 10^{-12} \text{m}^{-3} \text{kg}^{-1} \text{s}^4 \text{A}^2$.

κ_r is the dielectric constant = 3.9 for SiO_2 .

d is the thickness of SiO_2 layer i.e 285 nm.

Evaluating eq 6-3

$$C_o = \frac{8.854 \times 10^{-12} \times 3.9}{285 \times 10^{-9}} \text{Fcm}^{-2} \quad (6-4)$$

Therefore $C_o = 1.21 \times 10^{-8} \text{Fcm}^{-2}$ for 285 nm SiO_2 . V_{DS} and I_{DS} are the drain-source voltage and current. V_G is the back gate voltage.

6.4

Transport Measurement of MoS_2

We investigated the electrical properties of our low temperature synthesized MoS_2 crystals by fabricating two probe device on the as-grown sample. We applied the drain-source voltage (V_{DS}) from the electrodes. The back-gate voltage from the p-doped Si substrate, where the 285 nm SiO_2 serves as a back gate dielectric. Figure 6.3(a) presents the transfer characteristic curve of a FET device at room temperature, showing the typical n-type behaviour. Figure 6.3(b) shows the drain-source current (I_{DS}) as a function of source-drain voltage (V_{DS}) at different gate voltages.

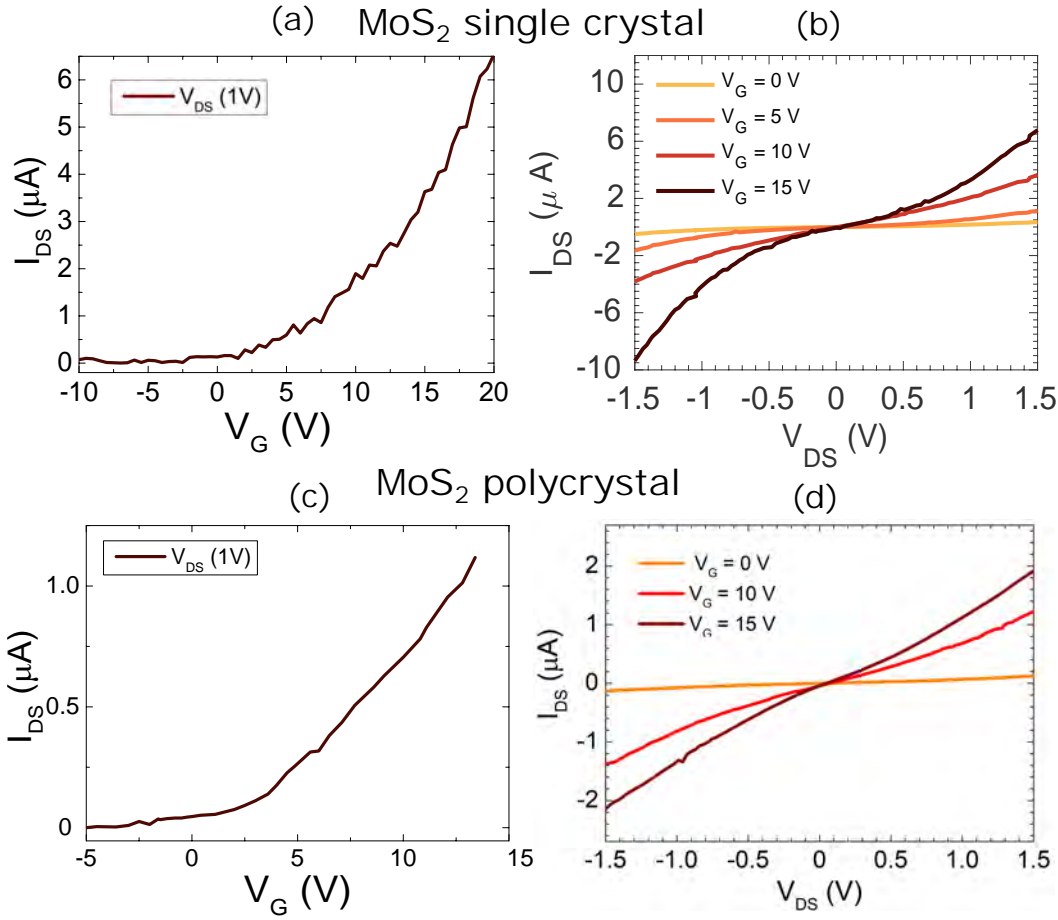


Figure 6.3: Transport measurements. (a) Transfer curve (I_{DS} vs. V_G) with V_{DS} fixed at 1 V, for MoS₂ single crystal. (b) Output curve (I_{DS} vs. V_{DS}) at different V_G values, for single crystal. (c) Transfer curve (I_{DS} vs. V_G) with V_{DS} fixed at 1 V for MoS₂ polycrystalline film. (d) Output curve (I_{DS} vs. V_{DS}) at different V_G values, for polycrystalline film.

Our single crystal MoS₂ device shows high electrical performance and the average electrical conductivity is estimated from the (I_{DS}) vs (V_{DS}) curve at 0 (V_G), $\sim 8.9 \times 10^{-7} \Omega^{-1}$. The mobility is estimated as $9.8 \pm 0.7 \text{ cm}^2\text{V}^{-1}\text{s}^{-1}$ which is comparable with the previous reports [28, 32, 69, 181, 201].

Similarly, the transfer characteristic curve and drain-source current (I_{DS}) vs. source-drain voltage (V_{DS}) for the polycrystalline film can be found at figure 6.3(c,d). Transfer curve for polycrystalline film is linear and symmetric compared to single crystal curve. The conductivity for polycrystalline film is almost equal to single crystal, $\sim 8 \times 10^{-7} \Omega^{-1}$. We estimated the mobility for the polycrystalline film at $2.7 \pm 0.5 \text{ cm}^2\text{V}^{-1}\text{s}^{-1}$. The relatively low electron mobility of the film is likely due to the presence of domain boundaries in the polycrystals, which could trap electrons and affect the charge transfer. Typically, in high-temperature synthesis, it is common to observe gate voltage

leakage through pinholes caused by the destruction of a thin SiO₂ layer. Another advantage of low-temperature synthesis is the possibility to direct fabrication of the device, avoiding the transfer procedure.

6.5 Transport Measurement of WS₂

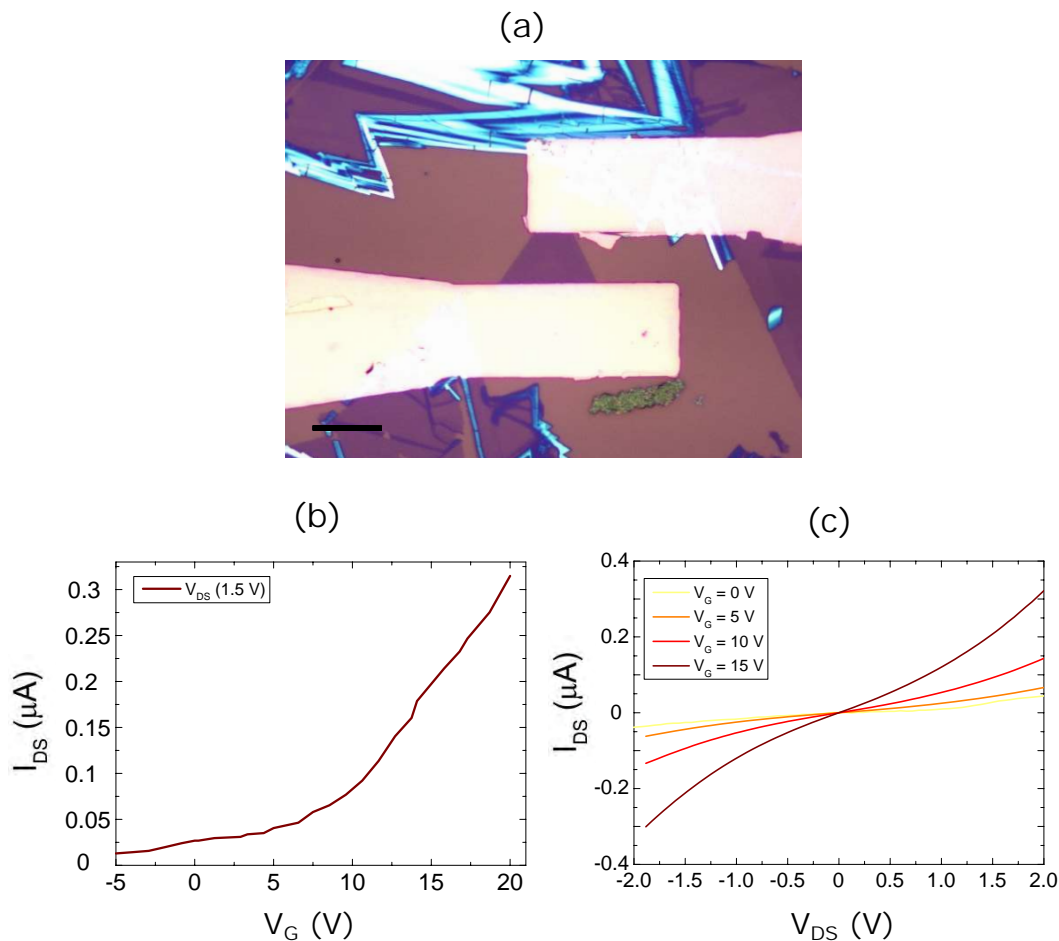


Figure 6.4: (a) Optical image of a FET device fabricated after transferring WS₂ on SiO₂/Si substrate, scale bar is 10 μm. (b) Transfer curve (I_{DS} vs. V_G) with V_{DS} fixed at 1.5 V for WS₂. (c) Output curve of WS₂ (I_{DS} vs. V_{DS}) for different V_G values.

Figure 6.4(a) depicts the optical image of the WS₂ FET device. WS₂ device was fabricated on the samples transferred on the SiO₂/Si substrate after growth to avoid any kind of leakage current from the SiO₂ dielectric. The transfer characteristic curve for WS₂ device is shown in figure 6.4(b). The output curve (I_{DS} vs. V_{DS}) of WS₂ was also measured see figure 6.4(c). WS₂ also shows n-type behaviour, the conductivity and mobility was also calculated for WS₂. The conductivity and mobility for WS₂ is $\sim 7 \times 10^{-9}$

Ω^{-1} and $\sim 0.53 \pm 0.1 \text{ cm}^2\text{V}^{-1}\text{s}^{-1}$ which is much lower compared to MoS₂. Relatively high mobility of MoS₂ compared to WS₂ shows sodium mediated low temperature synthesis grows better samples compared to high temperature synthesized WS₂.

6.6

Transport Measurement of MoS₂/WS₂ Heterostructure

Figure 6.5(a) shows the optical image of MoS₂/WS₂ heterostructure FET device on SiO₂/Si 285 nm substrate. The bottom triangle is the MoS₂ and on top of it is an incomplete grown WS₂ triangle. From the optical image, it seems a 0° (3R) stacked heterostructure. The drain-source current (I_{DS}) as a function of source-drain voltage (V_{DS}) at different gate voltages is shown in Figure 6.5(b). The conductivity estimated for MoS₂/WS₂ heterostructure, $\sim 2 \times 10^{-6} \Omega^{-1}$ which is highest compared to the other samples. Generally, CVD grown MoS₂/WS₂ vertical heterostructure are known to have high mobility than its counterparts [202]. Table 6.1 shows the comparison of mobility and conductivity of all of our devices.

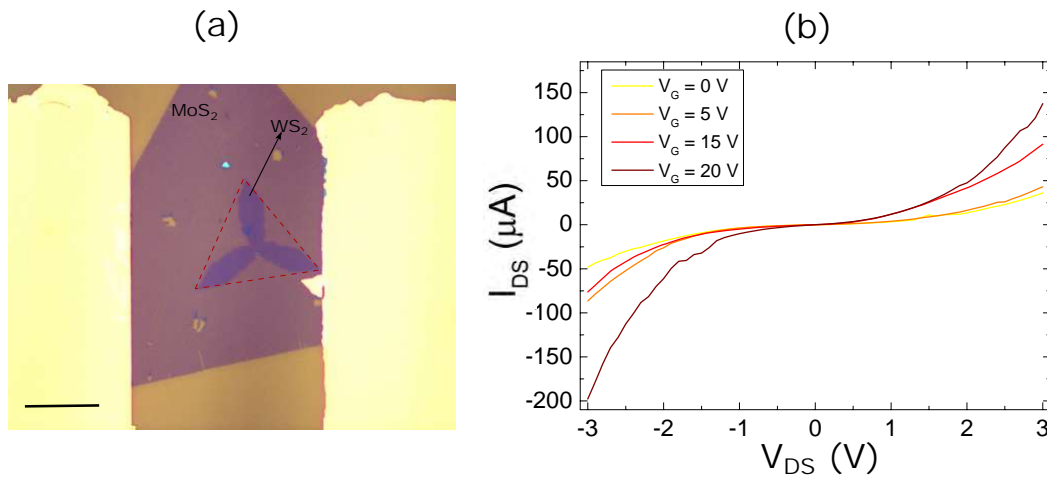


Figure 6.5: (a) Optical image of MoS₂/WS₂ heterostructure device on SiO₂/Si 285 nm substrate. The big triangle is the MoS₂ and on top of it flower shape is an incomplete grown WS₂ triangle. (b) Output curve of MoS₂/WS₂ (I_{DS} vs. V_{DS}) for different V_G values.

Strictly speaking, this is not the precise way of extracting conductivity and mobility. The exact value of conductivity needs four probe measurements rather than two probe, where we have minimum contact resistance and the shape of the TMD sheet should be rectangular. The standard complementary metal-oxide semiconductor technology requires equal and small values of

V_{DS} and V_G applied to determine these quantities. Our results are rather a comparison between our grown samples quality.

Sample	Average Conductivity at 0(V_G) Ω^{-1}	Mobility $cm^2V^{-1}s^{-1}$
MoS ₂ single crystal	8.9×10^{-7}	9.8 ± 0.7
MoS ₂ polycrystals	8×10^{-7}	2.7 ± 0.5
WS ₂	7×10^{-9}	0.53 ± 0.1
MoS ₂ /WS ₂	2×10^{-6}	—

Table 6.1: Average conductivity and mobility of TMDs.

6.7

Defect Related Raman Peak Reveled by Electro-Raman of MoS₂/WS₂ Device

Consider a voltage is applied across our device which will produce electric field. This electric field accumulates free or fixed charges at the interface between the oxide and the semiconductor throughout our TMD device. Such charges can effectively dope the semiconductor TMD in the region near the interface, and thus shifting the Fermi level. This shift in Fermi level could result in shifting of phonon modes. This effect is commonly used in electronic and optoelectronic devices to tune the conductivity as well as the electrical barrier in the devices. The gate voltage (V_G) creates an electrostatic potential difference between the sample and the gate electrode, and the addition of charge carriers leads to a shift in the Fermi level.

We measured the Raman spectra of MoS₂/WS₂ device shown in figure 6.5(a) and simultaneously applied the gate voltage. Figure 6.6 plots the Raman spectra at different values of back-gate voltage with 473 nm laser. After every step i.e increase in gate voltage, Raman spectrum was acquired after stabilization of the current I_{DS} . Each spectrum is collected at room temperature under ambient pressure for 50 sec. Figure 3.19 shows a schematic of the experimental setup of the Raman spectroscopy measurements with voltage.

Four prominent peaks were observed belonging to the in-plane and out of plane vibrational modes of WS₂ and MoS₂ layers. However, Raman signal from WS₂ (top layer) is stronger as compared to MoS₂. All the Raman peaks in figure 6.6 are fitted with Lorentzian function. Red dots are the experimental data, the black lines are fitted Lorentzians.

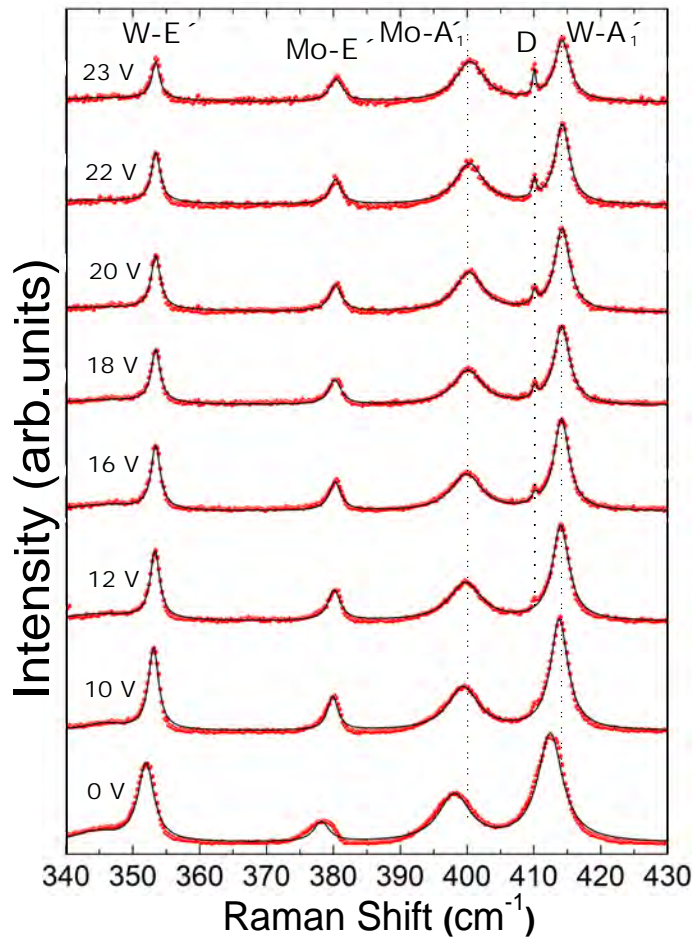


Figure 6.6: Raman spectra of MoS₂/WS₂ device at different back gate voltages V_G , laser wavelength 473 nm. Red circles are experimental data points, the black lines are Lorentzian fits to the total spectrum.

Figure 6.7(a) represents the dependence of peak position with applied gate voltage. The A'_1 modes show strong doping dependence, compared to E' . The $W-A'_1$ mode shows blueshift of $\sim 4 \text{ cm}^{-1}$, while $Mo-A'_1$ also shows blueshift of $\sim 3 \text{ cm}^{-1}$ with gate voltage. The FWHM of $W-A'_1$ and $Mo-A'_1$ extracted from lorentzian fit, decreases in both the cases see figure 6.7(b). This blueshift and decrease in FWHM is a result of electron doping. It is previously reported that the G-Band of graphene blueshifts and FWHM decreases with the electron and hole doping [193, 196, 203]. The FWHM of the Lorentzian components gives relevant information on the phonon lifetime. The intensity of the $W-A'_1$ and $Mo-A'_1$ mode is also attenuated by the high carrier density see figure 6.8(a).

A new peak emerges after $V_G = 10 \text{ V}$, at $\sim 410 \text{ cm}^{-1}$ which is related to defects (D) from the WS₂ crystal. Defects in the sample can be introduced during the (CVD) growth, device fabrication, or by electron doping. These defects are expected to worsen the device quality. However, these defects can also be beneficial for our device functionalities. Defects have been shown to

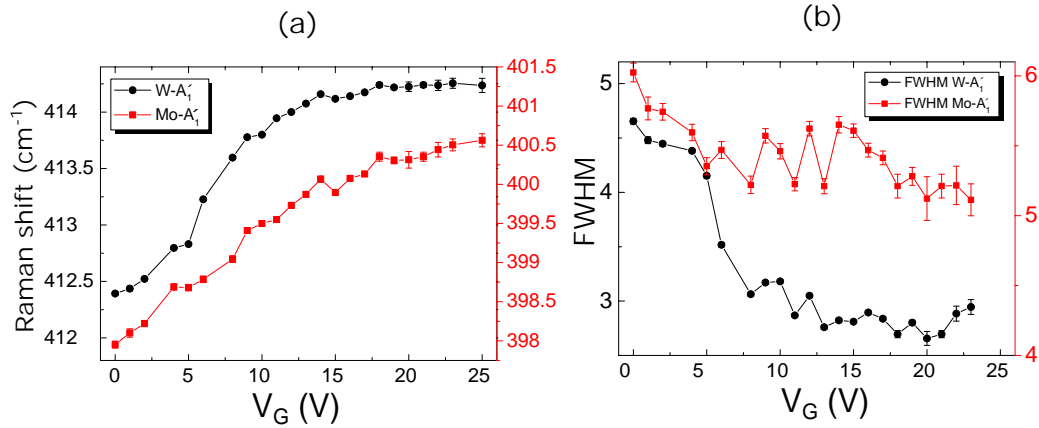


Figure 6.7: (a) Peak position of $W-A_1'$ and $Mo-A_1'$ as a function of V_G . (b) FWHM of $W-A_1'$ and $Mo-A_1'$ peak as a function of V_G .

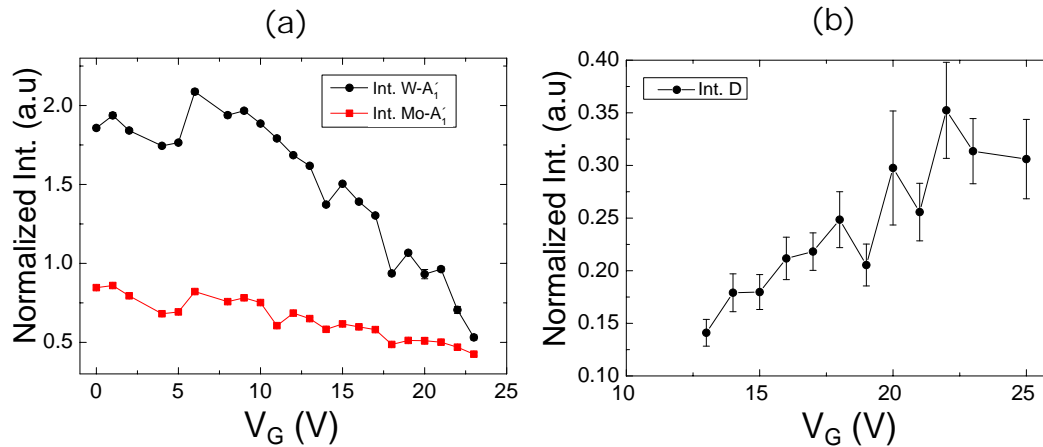


Figure 6.8: (a) Intensity normalized with Si peak $Mo-A_1'$ and $W-A_1'$ as a function of V_G . (b) Normalized intensity of D peak as a function of V_G .

be the dominant dopant in MoS_2 , and allows n-type and p-type regions to coexist across the regions of the same sample [204]. This D peak is most likely present in the Raman spectrum as shoulder peak with $W-A_1'$. Blueshifting of $W-A_1'$ peak have made it prominent. There is a strong correlation between the intensity of the D and A_1' peaks. The intensity of the D peak becomes more prominent with increase of gate voltage see figure 6.8(b), while the intensity of A_1' peaks shows opposite behavior see figure 6.8(a). The prominent appearance the D peak shows the density of defects. There is not much known about this D peak in the Raman spectrum. This peak was first reported by Chanwoo Lee et. al [205] by Tip-enhance Raman spectroscopy of monolayer WS_2 . The observed defect-related Raman mode can be utilized to evaluate the quality of our

sample and will be helpful to improve the performance of future optoelectronic devices.

We also did the electro-Raman measurements on WS₂ monolayer device. But no noticeable shift in the peaks were observed, likely due to the low conductivity of WS₂ device. More studies are required on the electro-Raman measurements to observe doping effects in different TMDs. The top gate FET devices might be a better option for higher doping at low gate voltage.

6.8

Partial Conclusion

In summary, we have investigated the transport properties of monolayer MoS₂, WS₂, and their heterostructure. The devices were fabricated by photolithography on the samples grown in the same CVD system, and characterized under the same ambient conditions to investigate their comparative performance. The back-gated, MoS₂/WS₂ heterostructure device show higher performance compared to the others. On the other hand, low temperature synthesised MoS₂ shows higher carrier mobility compared to WS₂. Further, we have demonstrated the electron doping dependence of Raman modes of MoS₂/WS₂ device. The A₁' peaks show blueshift following the decrease in FWHM, as result of change in Fermi level. A new peak emerges after sufficient electron doping following W-A₁' blueshift. This peak (D) is attributed to the defects in WS₂ layer.

In this thesis, we have reported the atmospheric pressure chemical vapor deposition (APCVD) synthesis of monolayer and bilayers MoS₂, WS₂, and their vertical heterostructure. We pointed out key elements in the CVD process for repeatable synthesis recipes. A new synthesis route was established mediated by sodium which leads us to the successful growth of monolayer MoS₂ single crystal and polycrystalline film at low temperature (550° C). The DFT calculation also shows that the critical element is the number of sodium in the system, which reduces the energy formation and allows to use a reduced temperature ($\Delta T = 250^\circ$ C). Single crystals were grown by controlling the Mo/Na ratio and polycrystals by increasing the growth time. We characterized the grown monolayers by optical microscopy, X-ray photoelectron spectroscopy (XPS), photoluminescence, Raman spectroscopy, atomic force microscopy (AFM), and transport experiments. The measurements confirm its monolayer thickness, crystallinity, optical and electrical properties. The analysis of Raman defective peak LA shows the same amount of defects in single and polycrystals. The optical and electrical performances are similar to those grown at high temperatures. This work would serve as a reference for the low-temperature synthesis of other TMDs.

The second harmonic generation (SHG) was studied on APCVD synthesised two and three layer samples. The SHG shows that the layers in bilayers grown with 0° have no inversion symmetry refers to 3R(AB) phase stacking. For 60°, we have an inversion symmetry (Centrosymmetric) and 2H(AA') phase stacking. These studies show that for CVD grown bilayer samples we can achieve both 2H(AA') and 3R(AB) phases.

The transport properties of monolayer MoS₂ and WS₂ and heterostructure was studied by fabricating devices on them. The back-gated, CVD grown MoS₂/WS₂ based device show higher performance compared to the others. Our study demonstrates high quality of material and further roots towards device optimization. We demonstrated the electron doping dependence of Raman modes of MoS₂/WS₂ device. The A_{1g} peaks show a blueshift following the decrease in FWHM, as a result of the change in Fermi level. A new peak emerges after sufficient electron doping. This peak (D') is attributed to the

defects in WS₂ layer.

Due to their uniqueness and diversity, TMDs are of far-reaching importance in scientific research and have various potential applications in future optoelectronic device technology. The direct bandgap and controllable valley polarization give TMDs promising opportunities in novel optoelectronics applications. Over 40 TMDs have been discovered yet [8], and the Van der Waals heterostructures gives infinite opportunities for new 2D-TMDs materials. We purpose the following works for the future on this topic:

A lot of work is already being done on MoS₂ and WS₂, we should move on to the synthesis of other TMDs e.g selenides and tellurides. Catalytic behaviour of sodium could be used in the synthesis of other TMDs. Since the theoretical calculations are fully in agreement with the experimental results, first principle calculations (DFT) before growing any new TMD, will be very helpful. More studies are needed on the synthesis of TMDs on glass. One should choose glass with low sodium concentration, which will help in growing clean samples and avoids multiple layers. Little is known about the transmission properties of CVD grown TMDs, direct synthesis on the ordinary glass will help in understanding the transmission properties and achieving novel flexible devices. Artificially stacked heterostructures, as well as CVD synthesized, opens an entirely new field of research, we should move on to the heterostructures of selenides, and sulphides which could provide us the controllable bandgap. We will try to synthesize new TMDs heterostructures and other 2D materials by CVD. The alternative way to achieve new heterostructures is transferring one TMD on another. We will search for the best candidates for fast-response, broadband photo-detecting, and high-efficiency light emission.

Second harmonic generation (SHG) should be studied on new artificially stacked layers e.g selenides and tellurides. WSe₂ field-effect transistor has already proved to be a new class of electrically tunable nonlinear optical device [58, 123]. We purpose to study the SHG in our heterostructure FET device. Also, the devices fabricated on different stacked heterostructures (i.e 0° and 60°) could be interesting to study. It will be interesting to see either nonlinear electric susceptibilities is tunable through electrostatic doping in a bilayer/heterostructure FET. A more interesting feature will be to check either it is possible to break the inversion symmetry in 2H stacked bilayer through electrostatic doping.

Improvements are needed in our back gate FET devices. Improved device engineering, including better gating schemes and waveguide integration, will enable enhanced tunability. We can reach much higher doping level with top gating than standard SiO₂ back gating. A suitable polymer electrolyte having high capacitance should be chosen as top gating material. The polymer should be transparent, which allows us to perform the optical measurements with simultaneous electrical characterization.

Bibliography

- [1] GEIM, A. K.; NOVOSELOV, K. S.. **The rise of graphene.** *Nat. Mater.*, 6(3):183–191, 2007.
- [2] SCHWIERZ, F.. **Graphene transistors.** *Nat. Nanotechnol.*, 5(7):487–496, 2010.
- [3] TIWARI, S. K.; SAHOO, S.; WANG, N. ; HUCZKO, A.. **Graphene research and their outputs: Status and prospect.** *J. Sci. Adv. Mater. Devices*, 5(1):10–29, 2020.
- [4] BERNARDI, M.; ATACA, C.; PALUMMO, M. ; GROSSMAN, J. C.. **Optical and Electronic Properties of Two-Dimensional Layered Materials.** *Nanophotonics*, 6(2):479–493, 2017.
- [5] SAMADI, M.; SARIKHANI, N.; ZIRAK, M.; ZHANG, H.; ZHANG, H. L. ; MOSHFEGH, A. Z.. **Group 6 transition metal dichalcogenide nanomaterials: Synthesis, applications and future perspectives.** *Nanoscale Horizons*, 3(2):90–204, 2018.
- [6] CHHOWALLA, M.; LIU, Z. ; ZHANG, H.. **Two-dimensional transition metal dichalcogenide (TMD) nanosheets.** *Chem. Soc. Rev.*, 44(9):2584–2586, 2015.
- [7] DUAN, X.; WANG, C.; PAN, A.; YU, R. ; DUAN, X.. **Two-dimensional transition metal dichalcogenides as atomically thin semiconductors: Opportunities and challenges.** *Chem. Soc. Rev.*, 44(24):8859–8876, 2015.
- [8] MD NURUNNABI, J. M.. **Biomedical Applications of Graphene and 2D Nanomaterials**, 1st Edition, volumen 1. Elsevier, 2019.
- [9] WILSON, J. A.; YOFFE, A. D.. **The transition metal dichalcogenides discussion and interpretation of the observed optical, electrical and structural properties.** *Adv. Phys.*, 18(73):193–335, 1969.
- [10] FRINDT, R. F.; YOFFE, A. D.. **Physical Properties of Layer Structures: Optical Properties and Photoconductivity of Thin Crystals.**

- tals of Molybdenum Disulphide. Proc. R. Soc. A Math. Phys. Eng. Sci., 273(1352):69–83, 1963.
- [11] SPLENDIANI, A.; SUN, L.; ZHANG, Y.; LI, T.; KIM, J.; CHIM, C. Y.; GALLI, G. ; WANG, F.. **Emerging photoluminescence in monolayer MoS₂**. Nano Lett., 10(4):1271–1275, 2010.
- [12] LI, H.; WU, J.; YIN, Z. ; ZHANG, H.. **Preparation and applications of mechanically exfoliated single-layer and multilayer MoS₂ and WSe₂ nanosheets**. Acc. Chem. Res., 47(4):1067–1075, 2014.
- [13] YUAN, L.; GE, J.; PENG, X.; ZHANG, Q.; WU, Z.; JIAN, Y.; XIONG, X.; YIN, H. ; HAN, J.. **A reliable way of mechanical exfoliation of large scale two dimensional materials with high quality**. AIP Adv., 6(12), 2016.
- [14] AMBROSI, A.; PUMERA, M.. **The CVD graphene transfer procedure introduces metallic impurities which alter the graphene electrochemical properties**. Nanoscale, 6(1):472–476, 2014.
- [15] LIN, Z.; THEE, M. T.; ELÍAS, A. L.; FENG, S.; ZHOU, C.; FUJISAWA, K.; PEREA-LÓPEZ, N.; CAROZO, V.; TERRONES, H. ; TERRONES, M.. **Facile synthesis of MoS₂ and Mo_xW_{1-x}S₂ triangular monolayers**. APL Mater., 2(9):092514, 2014.
- [16] WANG, X.; GONG, Y.; GANG, S.; CHOW, W. L.; KEYSHAR, W.; YE, G.; VAJTAI, R.; LOU, J.; LIU, Z.; RINGE, E.; TAY, B. K. ; AJAYAN, P. M.. **Chemical vapor deposition growth of Crystalline Monolayer MoSe₂**. ACS Nano, 8(5):5125–5131, 2014.
- [17] LEE, Y. H.; ZHANG, X. Q.; ZHANG, W.; CHANG, M. T.; LIN, C. T.; CHANG, K. D.; YU, Y. C.; WANG, J. T.; CHANG, C. S.; LI, L. J. ; LIN, T. W.. **Synthesis of large-area MoS₂ atomic layers with chemical vapor deposition**. Adv Mater, 24(17):2320–2325, 2012.
- [18] ZHAO, W. F.; YU, H.; LIAO, M. Z.; ZHANG, L.; ZOU, S. Z.; YU, H. J.; HE, C. J.; ZHANG, J. Y.; ZHANG, G. Y. ; LIN, X. C.. **Large area growth of monolayer MoS₂ film on quartz and its use as a saturable absorber in laser mode-locking**. Semicond. Sci. Technol., 32(2), 2017.
- [19] HAMMETT, B.; RESEARCH, BREANNE HAMMETT AND, A. . ; NANAYAKKARA, S.. **Optimizing growth conditions for 2D MoS₂**. , 2017.

- [20] BILGIN, I.; LIU, F.; VARGAS, A.; WINCHESTER, A.; MAN, M. K.; UP-MANYU, M.; DANI, K. M.; GUPTA, G.; TALAPATRA, S.; MOHITE, A. D. ; KAR, S.. **Chemical Vapor Deposition Synthesized Atomically Thin Molybdenum Disulfide with Optoelectronic-Grade Crystalline Quality.** *ACS Nano*, 9(9):8822–8832, 2015.
- [21] MUKULIKA DINARA, C. S. R.. **Two Dimensional Transition Metal Dichalcogenides**, volumen 1. Springer Singapore, 2019.
- [22] CHANG SEOK, L.; COSTEL SORIN, C.; WALEED, M.; BÉRENGÈRE, L.; MARC, C.; MARC, C.; FRANÇOIS LE, N. ; JEAN-LUC, M.. **Synthesis of conducting transparent few-layer graphene directly on glass at 450°C.** *Nanotechnology*, 23(26):265603, 2012.
- [23] CHEN, Y. Z.; MEDINA, H.; TSAI, H. W.; WANG, Y. C.; YEN, Y. T.; MANIKANDAN, A. ; CHUEH, Y. L.. **Low temperature growth of graphene on glass by carbon-enclosed chemical vapor deposition process and its application as transparent electrode.** *Chem. Mater.*, 27(5):1646–1655, 2015.
- [24] SUN, J.; CHEN, Y.; CAI, X.; MA, B.; CHEN, Z.; PRIYDARSHI, M. K.; CHEN, K.; GAO, T.; SONG, X.; JI, Q.; GUO, X.; ZOU, D.; ZHANG, Y. ; LIU, Z.. **Direct low-temperature synthesis of graphene on various glasses by plasma-enhanced chemical vapor deposition for versatile, cost-effective electrodes.** *Nano Res.*, 8(11):3496–3504, 2015.
- [25] PARK, B. J.; CHOI, J. S.; EOM, J. H.; HA, H.; KIM, H. Y.; LEE, S.; SHIN, H. ; YOON, S. G.. **Defect-Free Graphene Synthesized Directly at 150 °c via Chemical Vapor Deposition with No Transfer.** *ACS Nano*, 12(2):2008–2016, 2018.
- [26] JANG, J.; SON, M.; CHUNG, S.; KIM, K.; CHO, C.; LEE, B. H. ; HAM, M. H.. **Low-temperature-grown continuous graphene films from benzene by chemical vapor deposition at ambient pressure.** *Sci. Rep.*, 5(November):1–7, 2015.
- [27] MARCHENA, M.; JANNER, D.; CHEN, T. L.; FINAZZI, V. ; PRUNERI, V.. **Low temperature direct growth of graphene patterns on flexible glass substrates catalysed by a sacrificial ultrathin Ni film.** *Opt. Mater. Express*, 6(8):2487, 2016.

- [28] GONG, Y.; LIN, Z.; YE, G.; SHI, G.; FENG, S.; LEI, Y.; ELÍAS, A. L.; PEREA-LOPEZ, N.; VAJTAI, R.; TERRONES, H.; LIU, Z.; TERRONES, M.; AJAYAN, P. M.. **Tellurium-Assisted Low-Temperature Synthesis of MoS₂ and WS₂ Monolayers.** *ACS Nano*, 9(12):11658–11666, 2015.
- [29] CHOI, S. H.; KIM, Y. J.; YANG, W.; KIM, K. K.. **Alkali Metal-Assisted Growth of Single-Layer Molybdenum Disulfide.** *J. Korean Phys. Soc.*, 74(11):1032–1038, 2019.
- [30] HAN, W.; LIU, K.; YANG, S.; WANG, F.; SU, J.; JIN, B.. **Salt-assisted chemical vapor deposition of two-dimensional materials.** *SCIENCE CHINA Chemistry*, 2019.
- [31] WANG, P.; LEI, J.; QU, J.; CAO, S.; JIANG, H.; HE, M.; SHI, H.; SUN, X.; GAO, B.; LIU, W.. **Mechanism of Alkali Metal Compound-Promoted Growth of Monolayer MoS₂: Eutectic Intermediates.** *Chem. Mater.*, 31(3):873–880, 2019.
- [32] YANG, P.; ZOU, X.; ZHANG, Z.; HONG, M.; SHI, J.; CHEN, S.; SHU, J.; ZHAO, L.; JIANG, S.; ZHOU, X.; HUAN, Y.; XIE, C.; GAO, P.; CHEN, Q.; ZHANG, Q.; LIU, Z.; ZHANG, Y.. **Batch production of 6-inch uniform monolayer molybdenum disulfide catalyzed by sodium in glass.** *Nat. Commun.*, 9(1), 2018.
- [33] CHEN, W.; ZHAO, J.; ZHANG, J.; GU, L.; YANG, Z.; LI, X.; YU, H.; ZHU, X.; YANG, R.; SHI, D.; LIN, X.; GUO, J.; BAI, X.; ZHANG, G.. **Oxygen-Assisted Chemical Vapor Deposition Growth of Large Single-Crystal and High-Quality Monolayer MoS₂.** *J. Am. Chem. Soc.*, 137(50):15632–15635, 2015.
- [34] SHI, Y.; YANG, P.; JIANG, S.; ZHANG, Z.; HUAN, Y.; XIE, C.; HONG, M.; SHI, J.; ZHANG, Y.. **Na-assisted fast growth of large single-crystal MoS₂ on sapphire.** *Nanotechnology*, 30(3), 2019.
- [35] SORKIN, V.; PAN, H.; SHI, H.; QUEK, S. Y.; ZHANG, Y. W.. **Nanoscale transition metal dichalcogenides: Structures, properties, and applications.** *Crit. Rev. Solid State Mater. Sci.*, 39(5):319–367, 2014.
- [36] XU, K.; WANG, Z.; DU, X.; SAFDAR, M.; JIANG, C.; HE, J.. **Atomic-layer triangular WSe₂ sheets: Synthesis and layer-dependent photoluminescence property.** *Nanotechnology*, 24(46), 2013.

- [37] RUPPERT, C.; ASLAN, O. B. ; HEINZ, T. F.. **Optical properties and band gap of single- and few-layer MoTe₂ crystals.** Nano Lett., 14(11):6231–6236, 2014.
- [38] MAK, K.; LEE, C.; HONE, J.; SHAN, J. ; HEINZ, T.. **Atomically Thin MoS₂: A New Direct-Gap Semiconductor.** Phys. Rev. Lett., 105(13):136805, 2010.
- [39] LIU, G. B.; SHAN, W. Y.; YAO, Y.; YAO, W. ; XIAO, D.. **Three-band tight-binding model for monolayers of group-VIB transition metal dichalcogenides.** Phys. Rev. B - Condens. Matter Mater. Phys., 88(8):1–11, 2013.
- [40] KIM, E.; CHO, J.-W.; KIM, B. R.; THI, T.; NGUYEN, T.; NAM, Y.-H.; KIM, S.-K.; YOON, S.; KIM, Y. S.; LEE, J.-H. ; KIM, D.-W.. **Interference-Enhanced Broadband Absorption of Monolayer MoS₂ on Sub-100 nm Thick SiO₂/Si Substrates : Reflection and Transmission Phase Changes at Interfaces.** Advanced Materials., 1701637:1–7, 2018.
- [41] RUKELJ, Z.; ŠTRKALJ, A. ; DESPOJA, V.. **Optical absorption and transmission in a molybdenum disulfide monolayer.** Phys. Rev. B, 94(11):1–11, 2016.
- [42] LI, Y.; DONG, N.; ZHANG, S.; ZHANG, X.; FENG, Y.; WANG, K.; ZHANG, L. ; WANG, J.. **Giant two-photon absorption in monolayer MoS₂.** Laser Photonics Rev., 9(4):427–434, 2015.
- [43] LEE, C.; YAN, H.; BRUS, L.; HEINZ, T.; HONE, J. ; RYU, S.. **Anomalous lattice vibrations of single-and few-layer MoS₂.** ACS Nano, 4(5):2695–2700, 2010.
- [44] LI, H.; ZHANG, Q.; YAP, C. C. R.; TAY, B. K.; EDWIN, T. H. T.; OLIVIER, A. ; BAILLARGEAT, D.. **From bulk to monolayer MoS₂: Evolution of Raman scattering.** Adv. Funct. Mater., 22(7):1385–1390, 2012.
- [45] BERKDEMIR, A.; GUTIÉRREZ, H. R.; BOTELLO-MÉNDEZ, A. R.; PEREA-LÓPEZ, N.; ELÍAS, A. L.; CHIA, C. I.; WANG, B.; CRESPI, V. H.; LÓPEZ-URÍAS, F.; CHARLIER, J. C.; TERRONES, H. ; TERRONES, M.. **Identification of individual and few layers of WS₂ using Raman Spectroscopy.** Sci. Rep., 3:1–8, 2013.
- [46] MIGNUZZI, S.; POLLARD, A. J.; BONINI, N.; BRENNAN, B.; GILMORE, I. S.; PIMENTA, M. A.; RICHARDS, D. ; ROY, D.. **Effect of disorder**

- on Raman scattering of single-layer MoS₂. *Phys. Rev. B - Condens. Matter Mater. Phys.*, 91(19):1–7, 2015.
- [47] AUTERE, A.; JUSSILA, H.; DAI, Y.; WANG, Y.; LIPSANEN, H. ; SUN, Z.. **Nonlinear Optics with 2D Layered Materials**. *Adv. Mater.*, 30(24):1–24, 2018.
- [48] WEN, X.; GONG, Z. ; LI, D.. **Nonlinear optics of two-dimensional transition metal dichalcogenides**. *InfoMat*, 1(3):317–337, 2019.
- [49] WAGONER, G. A.; PERSANS, P. D.; VAN WAGENEN, E. A. ; KORNOWSKI, G. M.. **Second-harmonic generation in molybdenum disulfide**. *J. Opt. Soc. Am. B*, 15(3):1017, 1998.
- [50] LI, Y.; RAO, Y.; MAK, K. F.; YOU, Y.; WANG, S.; DEAN, C. R. ; HEINZ, T. F.. **Probing Symmetry Properties of Few-Layer MoS₂ and h-BN by Optical Second-Harmonic Generation**. *Nano Letters*, p. 3329–3333, 2013.
- [51] MALARD, L. M.; ALENCAR, T. V.; BARBOZA, A. P. M.; MAK, K. F. ; DE PAULA, A. M.. **Observation of intense second harmonic generation from MoS₂ atomic crystals**. *Phys. Rev. B - Condens. Matter Mater. Phys.*, 87(20):1–5, 2013.
- [52] KUMAR, N.; NAJMAEI, S.; CUI, Q.; CEBALLOS, F.; AJAYAN, P. M.; LOU, J. ; ZHAO, H.. **Second harmonic microscopy of monolayer MoS₂**. *Phys. Rev. B - Condens. Matter Mater. Phys.*, 87(16):1–6, 2013.
- [53] WOODWARD, R. I.; MURRAY, R. T.; PHELAN, C. F.; DE OLIVEIRA, R. E. P.; RUNCORN, T. H.; KELLEHER, E. J. R.; LI, S.; DE OLIVEIRA, E. C.; FECHINE, G. J. M.; EDA, G. ; DE MATOS, C. J. S.. **Characterization of the second- and third-order nonlinear optical susceptibilities of monolayer MoS₂ using multiphoton microscopy**. *2D Mater.*, 2016.
- [54] CHEN, H.; CORBOLIOU, V.; SOLNTSEV, A. S.; CHOI, D.-Y.; VINCENTI, M. A.; DE CEGLIA, D.; DE ANGELIS, C.; LU, Y. ; NESHEV, D. N.. **Enhanced second-harmonic generation from two-dimensional MoSe₂ on a silicon waveguide**. *Light Sci. Appl.*, 6(10):e17060, 2017.
- [55] LIN, X.; LIU, Y.; WANG, K.; WEI, C.; ZHANG, W.; YAN, Y.; LI, Y. J.; YAO, J. ; ZHAO, Y. S.. **Two-Dimensional Pyramid-like WS₂ Layered Structures for Highly Efficient Edge Second-Harmonic Generation**. *ACS Nano*, 12(1):689–696, 2018.

- [56] HU, L.; WEI, D.; HUANG, X.; HU, L.; WEI, D. ; HUANG, X.. **Second harmonic generation property of monolayer TMDCs and its potential application in producing terahertz radiation.** THE JOURNAL OF CHEMICAL PHYSICS, 244701, 2017.
- [57] JANISCH, C.; WANG, Y.; MA, D.; MEHTA, N.; ELÍAS, A. L.; PEREA-LÓPEZ, N.; TERRONES, M.; CRESPI, V. ; LIU, Z.. **Extraordinary second harmonic generation in Tungsten disulfide monolayers.** Sci. Rep., 4(c):1–5, 2014.
- [58] SEYLER, K. L.; SCHAIBLEY, J. R.; GONG, P.; RIVERA, P.; JONES, A. M.; WU, S.; YAN, J.; MANDRUS, D. G.; YAO, W. ; XU, X.. **Electrical control of second-harmonic generation in a WSe₂ monolayer transistor.** Nat. Nanotechnol., 10(5):407–411, 2015.
- [59] RIBEIRO-SOARES, J.; JANISCH, C.; LIU, Z.; ELÍAS, A. L.; DRESSELHAUS, M. S.; TERRONES, M.; CANÇADO, L. G. ; JORIO, A.. **Second harmonic generation in WSe₂.** 2D Mater., 2(4):1–6, 2015.
- [60] PSILODIMITRAKOPOULOS, S.; MOUCHLIADIS, L.; PARADISANOS, I.; KOURMOULAKIS, G.; LEMONIS, A.; KIOSEOGLU, G. ; STRATAKIS, E.. **Twist Angle mapping in layered WS₂ by Polarization-Resolved Second Harmonic Generation.** Sci. Rep., 9(1):1–11, 2019.
- [61] TOH, R. J.; SOFER, Z.; LUXA, J.; SEDMIDUBSKÝ, D. ; PUMERA, M.. **3R phase of MoS₂ and WS₂ outperforms the corresponding 2H phase for hydrogen evolution.** Chem. Commun., 53(21):3054–3057, 2017.
- [62] HSU, W. T.; ZHAO, Z. A.; LI, L. J.; CHEN, C. H.; CHIU, M. H.; CHANG, P. S.; CHOU, Y. C. ; CHANG, W. H.. **Second harmonic generation from artificially stacked transition metal dichalcogenide twisted bilayers.** ACS Nano, 8(3):2951–2958, 2014.
- [63] RADISAVLJEVIC, B.; RADENOVIC, A.; BRIVIO, J.; GIACOMETTI, V. ; KIS, A.. **Single-layer MoS₂ transistors.** Nat. Nanotechnol., 6(3):147–150, 2011.
- [64] CHOI, W.; CHO, M. Y.; KONAR, A.; LEE, J. H.; CHA, G. B.; HONG, S. C.; KIM, S.; KIM, J.; JENA, D.; JOO, J. ; KIM, S.. **High-detectivity multilayer MoS₂ phototransistors with spectral response from ultraviolet to infrared.** Adv. Mater., 24(43):5832–5836, 2012.

- [65] PARK, M. J.; MIN, J. K.; YI, S. G.; KIM, J. H.; OH, J. ; YOO, K. H.. **Near-infrared photodetectors utilizing MoS₂-based heterojunctions.** *J. Appl. Phys.*, 118(4), 2015.
- [66] WANG, W.; KLOTS, A.; PRASAI, D.; YANG, Y.; BOLOTIN, K. I. ; VALENTINE, J.. **Hot Electron-Based Near-Infrared Photodetection Using Bilayer MoS₂.** *Nano Lett.*, 15(11):7440–7444, 2015.
- [67] VAN DER ZANDE, A. M.; HUANG, P. Y.; CHENET, D. A.; BERKELBACH, T. C.; YOU, Y.; LEE, G.-H.; HEINZ, T. F.; REICHMAN, D. R.; MULLER, D. A. ; HONE, J. C.. **Grains and grain boundaries in highly crystalline monolayer molybdenum disulphide.** *Nat. Mater.*, 12(6):554–561, 2013.
- [68] CHENG, R.; JIANG, S.; CHEN, Y.; LIU, Y.; WEISS, N.; CHENG, H.-C.; WU, H.; HUANG, Y. ; DUAN, X.. **Few-layer molybdenum disulfide transistors and circuits for high-speed flexible electronics.** *Nat. Commun.*, 5:5143, 2014.
- [69] LI, X.; YANG, L.; SI, M.; LI, S.; HUANG, M.; YE, P. ; WU, Y.. **Performance potential and limit of MoS₂ transistors.** *Adv. Mater.*, 27(9):1547–1552, 2015.
- [70] AHN, J.-H.; PARKIN, W. M.; NAYLOR, C. H.; JOHNSON, A. T. C. ; DRNDIĆ, M.. **Ambient effects on electrical characteristics of CVD-grown monolayer MoS₂ field-effect transistors.** *Sci. Rep.*, 7(1):4075, 2017.
- [71] HSU, T.; YIN, Z.; LI, H. H.; LI, H. H.; JIANG, L.; SHI, Y.; SUN, Y.; LU, G.; ZHANG, Q.; CHEN, X. ; ZHANG, H.. **Single-layer MoS₂ phototransistors.** *ACS Nano*, .(1):74–80, 2012.
- [72] THAKAR, K.; LODHA, S.. **Optoelectronic and photonic devices based on transition metal dichalcogenides.** *Mater. Res. Express*, 7(1), 2019.
- [73] KUFER, D.; NIKITSKIY, I.; LASANTA, T.; NAVICKAITE, G.; KOPPENS, F. H. ; KONSTANTATOS, G.. **Hybrid 2D-0D MoS₂-PbS quantum dot photodetectors.** *Adv. Mater.*, 27(1):176–180, 2015.
- [74] GONG, F.; FANG, H.; WANG, P.; SU, M.; LI, Q.; HO, J. C.; CHEN, X.; LU, W.; LIAO, L.; WANG, J. ; HU, W.. **Visible to near-infrared photodetectors based on MoS₂ vertical Schottky junctions.** *Nanotechnology*, 28(48), 2017.

- [75] WANG, Y.; HUANG, X.; WU, D.; ZHUO, R.; WU, E.; JIA, C.; SHI, Z.; XU, T.; TIAN, Y.; LI, X.. **A room-temperature near-infrared photodetector based on a MoS₂/CdTe p-n heterojunction with a broadband response up to 1700 nm.** *J. Mater. Chem. C*, 6(18):4861–4865, 2018.
- [76] HWANG, I.; KIM, J. S.; CHO, S. H.; JEONG, B.; PARK, C.. **Flexible Vertical p-n Diode Photodetectors with Thin N-type MoSe₂ Films Solution-Processed on Water Surfaces.** *ACS Appl. Mater. Interfaces*, 10(40):34543–34552, 2018.
- [77] ZHANG, B. Y.; LIU, T.; MENG, B.; LI, X.; LIANG, G.; HU, X.; WANG, Q. J.. **Broadband high photoresponse from pure monolayer graphene photodetector.** *Nat. Commun.*, 4(May):1811, 2013.
- [78] HUO, N.; KONSTANTATOS, G.. **Recent progress and future prospects of 2D-based photodetectors.** *Adv. Mater.*, 30(51):1–27, 2018.
- [79] LOPEZ-SANCHEZ, O.; LEMBKE, D.; KAYCI, M.; RADENOVIC, A.; KIS, A.. **Ultrasensitive photodetectors based on monolayer MoS₂.** *Nat. Nanotechnol.*, 8(7):497–501, 2013.
- [80] KOPPENS, F. H.; MUELLER, T.; AVOURIS, P.; FERRARI, A. C.; VI-TIELLO, M. S.; POLINI, M.. **Photodetectors based on graphene, other two-dimensional materials and hybrid systems.** *Nat. Nanotechnol.*, 9(10):780–793, 2014.
- [81] CHAKRABORTY, B.; BERA, A.; MUTHU, D. V. S.; BHOWMICK, S.; WAGHMARE, U. V.; SOOD, A. K.. **Symmetry-dependent phonon renormalization in monolayer MoS₂ transistor.** *Phys. Rev. B - Condens. Matter Mater. Phys.*, 85(16):2–5, 2012.
- [82] FLOWERS, P.; ROBINSON, W. R.. **Chemistry 2e.**, volumen 1. Open stax, 2015.
- [83] CHHOWALLA, M.; SHIN, H. S.; EDA, G.; LI, L. J.; LOH, K. P.; ZHANG, H.. **The chemistry of two-dimensional layered transition metal dichalcogenide nanosheets.** *Nat. Chem.*, 5(4):263–275, 2013.
- [84] WANG, Q. H.; KALANTAR-ZADEH, K.; KIS, A.; COLEMAN, J. N.; STRANO, M. S.. **Electronics and optoelectronics of two-dimensional transition metal dichalcogenides.** *Nat. Nanotechnol.*, 7(11):699–712, 2012.

- [85] PODBEREZSKAYA, N. V.; MAGARILL, S. A.; PERVUKHINA, N. V. ; BORISOV, S. V.. **Crystal chemistry of dichalcogenides MX₂**. *J. Struct. Chem.*, 42(4):654–681, 2001.
- [86] ZAFEIRATOS, S.. **2D Nanomaterials for Energy Applications**. Elsevier, 1st ed. edition, 2019.
- [87] ZHANG, Y. J.; OSHIDA, M. Y.; SUZUKI, R. ; IWASA, Y.. **2D crystals of transition metal dichalcogenide and their iontronic functionalities**. *2D Mater.*, 2(4):44004, 2015.
- [88] RIBEIRO-SOARES, J.; ALMEIDA, R. M.; BARROS, E. B.; ARAUJO, P. T.; DRESSELHAUS, M. S.; CANÇADO, L. G. ; JORIO, A.. **Group Theory analysis of phonons in two-dimensional Transition Metal Dichalcogenides**. *PHYSICAL REVIEW B*, 115438, 2014.
- [89] LIU, G. B.; XIAO, D.; YAO, Y.; XU, X. ; YAO, W.. **Electronic structures and theoretical modelling of two-dimensional group-VIB transition metal dichalcogenides**. *Chem. Soc. Rev.*, 44(9):2643–2663, 2015.
- [90] MOLINA-SÁNCHEZ, A.; WIRTZ, L.. **Phonons in single-layer and few-layer MoS₂ and WS₂**. *Phys. Rev. B - Condens. Matter Mater. Phys.*, 84(15):1–8, 2011.
- [91] YAN, J.; XIA, J.; WANG, X.; LIU, L.; KUO, J. L.; TAY, B. K.; CHEN, S.; ZHOU, W.; LIU, Z. ; SHEN, Z. X.. **Stacking-Dependent Interlayer Coupling in Trilayer MoS₂ with Broken Inversion Symmetry**. *Nano Lett.*, 15(12):8155–8161, 2015.
- [92] YAN, A.; CHEN, W.; OPHUS, C.; CISTON, J.; LIN, Y.; PERSSON, K. ; ZETTL, A.. **Identifying different stacking sequences in few-layer CVD-grown MoS₂ by low-energy atomic-resolution scanning transmission electron microscopy**. *Phys. Rev. B*, 93(4):1–5, 2016.
- [93] SUZUKI, R.; SAKANO, M.; ZHANG, Y. J.; AKASHI, R.; MORIKAWA, D.; HARASAWA, A.; YAJI, K.; KURODA, K.; MIYAMOTO, K.; OKUDA, T.; ISHIZAKA, K.; ARITA, R. ; IWASA, Y.. **Valley-dependent spin polarization in bulk MoS₂ with broken inversion symmetry**. *Nat. Nanotechnol.*, 9(8):611–617, 2014.
- [94] ZENG, Z.; SUN, X.; ZHANG, D.; ZHENG, W.; FAN, X.; HE, M.; XU, T.; SUN, L.; WANG, X. ; PAN, A.. **Controlled Vapor Growth and**

- Nonlinear Optical Applications of Large-Area 3R Phase WS₂ and WSe₂ Atomic Layers.** *Adv. Funct. Mater.*, 29(11):1–8, 2019.
- [95] JIANG, T.; LIU, H.; HUANG, D.; ZHANG, S.; LI, Y.; GONG, X.; SHEN, Y. R.; LIU, W. T. ; WU, S.. **Valley and band structure engineering of folded MoS₂ bilayers.** *Nat. Nanotechnol.*, 9(10):825–829, 2014.
- [96] WIETING, T. J.; VERBLE, J. L.. **Infrared and Raman studies of long-wavelength optical phonons in hexagonal MoS₂.** *Phys. Rev. B*, 3(12):4286–4292, 1971.
- [97] HORZUM, S.; SAHIN, H.; CAHANGIROV, S.; CUDAZZO, P.; RUBIO, A.; SERIN, T. ; PEETERS, F. M.. **Phonon softening and direct to indirect band gap crossover in strained single-layer MoSe₂.** *Phys. Rev. B - Condens. Matter Mater. Phys.*, 87(12):1–5, 2013.
- [98] CAI, Y.; LAN, J.; ZHANG, G. ; ZHANG, Y. W.. **Lattice vibrational modes and phonon thermal conductivity of monolayer MoS₂.** *Phys. Rev. B - Condens. Matter Mater. Phys.*, 89(3):1–8, 2014.
- [99] ZHANG, X.; QIAO, X. F.; SHI, W.; WU, J. B.; JIANG, D. S. ; TAN, P. H.. **Phonon and Raman scattering of two-dimensional transition metal dichalcogenides from monolayer, multilayer to bulk material.** *Chem. Soc. Rev.*, 44(9):2757–2785, 2015.
- [100] ZHAO, W.; RIBEIRO, R. M. ; EDA, G.. **Electronic structure and optical signatures of semiconducting transition metal dichalcogenide nanosheets.** *Acc. Chem. Res.*, 48(1):91–99, 2015.
- [101] CHANG, C. H.; FAN, X.; LIN, S. H. ; KUO, J. L.. **Orbital analysis of electronic structure and phonon dispersion in MoS₂, MoSe₂, WS₂, and WSe₂ monolayers under strain.** *Phys. Rev. B - Condens. Matter Mater. Phys.*, 88(19):1–9, 2013.
- [102] SUN, Y.; WANG, D. ; SHUAI, Z.. **Indirect-to-Direct Band Gap Crossover in Few-Layer Transition Metal Dichalcogenides: A Theoretical Prediction.** *J. Phys. Chem. C*, 120(38):21866–21870, 2016.
- [103] YAZYEV, O. V.; KIS, A.. **MoS₂ and semiconductors in the flatland.** *Mater. Today*, 18(1):20–30, 2015.
- [104] YAKOVKIN, I.. **Dirac Cones in Graphene, Interlayer Interaction in Layered Materials, and the Band Gap in MoS₂.** *Crystals*, 6(11):143, 2016.

- [105] ELLIS, J. K.; LUCERO, M. J. ; SCUSERIA, G. E.. **The indirect to direct band gap transition in multilayered MoS₂ as predicted by screened hybrid density functional theory.** *Appl. Phys. Lett.*, 99(26):261908, 2011.
- [106] TUSCHEL, D.. **Raman Spectroscopy and Imaging of Low-Energy Phonons Raman.** *Spectroscopy Solutions for Materials Analysis*, 30(September), 2015.
- [107] EDA, G.; MAIER, S. A.. **Two-dimensional crystals: Managing light for optoelectronics.** *ACS Nano*, 7(7):5660–5665, 2013.
- [108] PIPER, J. R.; FAN, S.. **Broadband Absorption Enhancement in Solar Cells with an Atomically Thin Active Layer.** *ACS Photonics*, 3(4):571–577, 2016.
- [109] QIU, D. Y.; DA JORNADA, F. H. ; LOUIE, S. G.. **Optical spectrum of MoS₂: Many-body effects and diversity of exciton states.** *Phys. Rev. Lett.*, 111(21):1–5, 2013.
- [110] SIE, E. J.; FRENZEL, A. J.; LEE, Y. H.; KONG, J. ; GEDIK, N.. **Intervalley biexcitons and many-body effects in monolayer MoS₂.** *Phys. Rev. B - Condens. Matter Mater. Phys.*, 92(12):1–9, 2015.
- [111] BELLUS, M. Z.; CEBALLOS, F.; CHIU, H. Y. ; ZHAO, H.. **Tightly Bound Trions in Transition Metal Dichalcogenide Heterostructures.** *ACS Nano*, 9(6):6459–6464, 2015.
- [112] CAO, T.; WANG, G.; HAN, W.; YE, H.; ZHU, C.; SHI, J.; NIU, Q.; TAN, P.; WANG, E.; LIU, B. ; FENG, J.. **Valley-selective circular dichroism of monolayer molybdenum disulphide.** *Nat. Commun.*, 3(May), 2012.
- [113] LIU, Y.; GAO, Y.; ZHANG, S.; HE, J.; YU, J. ; LIU, Z.. **Valleytronics in transition metal dichalcogenides materials.** *Nano Res.*, 12(11):2695–2711, 2019.
- [114] VERHAGEN, T.; GUERRA, V. L.; HAIDER, G.; KALBAC, M. ; VEJPRAVOVA, J.. **Towards the evaluation of defects in MoS₂ using cryogenic photoluminescence spectroscopy.** *Nanoscale*, 12(5):3019–3028, 2020.
- [115] MAK, K. F.; HE, K.; LEE, C.; LEE, G. H.; HONE, J.; HEINZ, T. F. ; SHAN, J.. **Tightly bound trions in monolayer MoS₂.** *Nat. Mater.*, 12(3):207–211, 2013.

- [116] NEWAZ, A. K. M.; PRASAI, D.; ZIEGLER, J. I.; CAUDEL, D.; ROBINSON, S.; HAGLUND, R. F. ; BOLOTIN, K. I.. **Electrical Control of Optical Properties of Monolayer MoS₂**. *Solid State Communications.*, 2:1–5, 2012.
- [117] PIMENTA, M. A.; DEL CORRO, E.; CARVALHO, B. R.; FANTINI, C. ; MALARD, L. M.. **Comparative Study of Raman Spectroscopy in Graphene and MoS₂-type Transition Metal Dichalcogenides**. *Acc. Chem. Res.*, 48(1):41–47, 2015.
- [118] TERRONES, H.; DEL CORRO, E.; FENG, S.; POUMIROL, J. M.; RHODES, D.; SMIRNOV, D.; PRADHAN, N. R.; LIN, Z.; NGUYEN, M. A.; ELÍAS, A. L.; MALLOUK, T. E.; BALICAS, L.; PIMENTA, M. A. ; TERRONES, M.. **New First Order Raman-active Modes in Few Layered Transition Metal Dichalcogenides**. *Sci. Rep.*, 4:1–9, 2014.
- [119] ZHU, S.; WANG, Q.. **A simple method for understanding the triangular growth patterns of transition metal dichalcogenide sheets**. *AIP Adv.*, 5(10), 2015.
- [120] CAO, D.; SHEN, T.; LIANG, P.; CHEN, X. ; SHU, H.. **Role of chemical potential in flake shape and edge properties of monolayer MoS₂**. *J. Phys. Chem. C*, 119(8):4294–4301, 2015.
- [121] WANG, Y.; XIAO, J.; YANG, S.; WANG, Y. ; ZHANG, X.. **Second harmonic generation spectroscopy on two-dimensional materials**. *Opt. Mater. Express*, 9(3):1136, 2019.
- [122] SÄYNÄTJOKI, A.; KARVONEN, L.; ROSTAMI, H.; AUTERE, A.; MEHRAVAR, S.; LOMBARDO, A.; NORWOOD, R. A.; HASAN, T.; PEYGHAMBARIAN, N.; LIPSANEN, H.; KIEU, K.; FERRARI, A. C.; POLINI, M. ; SUN, Z.. **Ultra-strong nonlinear optical processes and trigonal warping in MoS₂ layers**. *Nat. Commun.*, 8(1):1–8, 2017.
- [123] YU, H.; TALUKDAR, D.; XU, W.; KHURGIN, J. B. ; XIONG, Q.. **Charge-Induced Second-Harmonic Generation in Bilayer WSe₂**. *Nano Lett.*, 15(8):5653–5657, 2015.
- [124] WANG, R.; CHIEN, H. C.; KUMAR, J.; KUMAR, N.; CHIU, H. Y. ; ZHAO, H.. **Third-harmonic generation in ultrathin films of MoS₂**. *ACS Appl. Mater. Interfaces*, 6(1):314–318, 2014.

- [125] LIU, H.; ANTWI, K. K.; CHUA, S. ; CHI, D.. **Vapor-phase growth and characterization of $\text{Mo}_{1-x}\text{W}_x\text{S}_2$ ($0 \leq x \leq 1$) atomic layers on 2-inch sapphire substrates.** *Nanoscale*, 6(1):624–629, 2014.
- [126] FU, Q.; YANG, L.; WANG, W.; HAN, A.; HUANG, J.; DU, P.; FAN, Z.; ZHANG, J. ; XIANG, B.. **Synthesis and Enhanced Electrochemical Catalytic Performance of Monolayer $\text{WS}_{2(1-x)}\text{Se}_{2x}$ with a Tunable Band Gap.** *Adv. Mater.*, 27(32):4732–4738, 2015.
- [127] TONGAY, S.; NARANG, D. S.; KANG, J.; FAN, W.; KO, C.; LUCE, A. V.; WANG, K. X.; SUH, J.; PATEL, K. D.; PATHAK, V. M.; LI, J. ; WU, J.. **Two-dimensional semiconductor alloys: Monolayer $\text{Mo}_{1-x}\text{W}_x\text{Se}_2$.** *Appl. Phys. Lett.*, 104(1), 2014.
- [128] LIN, Y. K.; CHEN, R. S.; CHOU, T. C.; LEE, Y. H.; CHEN, Y. F.; CHEN, K. H. ; CHEN, L. C.. **Thickness-Dependent Binding Energy Shift in Few-Layer MoS_2 Grown by Chemical Vapor Deposition.** *ACS Appl. Mater. Interfaces*, 8(34):22637–22646, 2016.
- [129] SYARI'ATI, A.; KUMAR, S.; ZAHID, A.; ALI EL YUMIN, A.; YE, J. ; RUDOLF, P.. **Photoemission spectroscopy study of structural defects in molybdenum disulfide (MoS_2) grown by chemical vapor deposition (CVD).** *Chem. Commun.*, 55(70):10384–10387, 2019.
- [130] LI, X.; CAI, W.; AN, J.; KIM, S.; NAH, J.; YANG, D.; PINER, R.; VELAMAKANNI, A.; JUNG, I.; TUTUC, E.; BANERJEE, S. K.; COLOMBO, L. ; RUOFF, R. S.. **Large-area synthesis of high-quality and uniform graphene films on copper foils.** *Science (80-.)*, 324(5932):1312–1314, 2009.
- [131] ZHU, H. W.; XU, C. L.; WU, D. H.; WEI, B. Q.; VAJTAI, R. ; AJAYAN, P. M.. **Direct synthesis of long single-walled carbon nanotube strands.** *Science (80-.)*, 296(5569):884–886, 2002.
- [132] SONG, L.; CI, L.; LU, H.; SOROKIN, P. B.; JIN, C.; NI, J.; KVASHNIN, A. G.; KVASHNIN, D. G.; LOU, J.; YAKOBSON, B. I. ; AJAYAN, P. M.. **Large scale growth and characterization of atomic hexagonal boron nitride layers.** *Nano Lett.*, 10(8):3209–3215, 2010.
- [133] KALITA, G.; TANEMURA, M.. **Fundamentals of Chemical Vapor Deposited Graphene and Emerging Applications.** *Graphene Mater. - Adv. Appl.*, 2017.

- [134] YU, J.; LI, J.; ZHANG, W. ; CHANG, H.. **Synthesis of high quality two-dimensional materials via chemical vapor deposition.** *Chem. Sci.*, 6(12):6705–6716, 2015.
- [135] YOU, J.; HOSSAIN, M. D. ; LUO, Z.. **Synthesis of 2D transition metal dichalcogenides by chemical vapor deposition with controlled layer number and morphology.** *Nano Converg.*, 5(1), 2018.
- [136] ZHANG, Y.; YAO, Y.; SENDEKU, M. G.; YIN, L.; ZHAN, X.; WANG, F.; WANG, Z. ; HE, J.. **Recent Progress in CVD Growth of 2D Transition Metal Dichalcogenides and Related Heterostructures.** *Adv. Mater.*, 31(41):1–30, 2019.
- [137] CAI, Z.; LIU, B.; ZOU, X. ; CHENG, H.-M.. **Chemical Vapor Deposition Growth and Applications of Two-Dimensional Materials and Their Heterostructures.** *Chem. Rev.*, 118:acs.chemrev.7b00536, 2018.
- [138] ZHANG, T.; FU, L.. **Controllable Chemical Vapor Deposition Growth of Two-Dimensional Heterostructures.** *Chem*, 4(4):671–689, 2018.
- [139] YIN, G.; ZHU, D.; LV, D.; HASHEMI, A.; FEI, Z.; LIN, F.; KRASHENINNIKOV, A. V.; ZHANG, Z.; KOMSA, H. P. ; JIN, C.. **Hydrogen-assisted post-growth substitution of tellurium into molybdenum disulfide monolayers with tunable compositions.** *Nanotechnology*, 29(14), 2018.
- [140] .. <https://www.shutterstock.com/editorial/image-editorial/education-2557517a>. ..
- [141] C.V. RAMAN. **The Raman Effect: Investigation of molecular structure by light scattering.** *Trans. Faraday Soc.*, 25(September):781–792, 1929.
- [142] FERRARO, J. R.; NAKAMOTO, K. ; BROWN, C. W.. **Introductory Raman Spectroscopy: Second Edition.** Elsevier, 2003.
- [143] DONG, Z.; XU, H.; LIANG, F.; LUO, C.; WANG, C.; CAO, Z. Y.; CHEN, X. J.; ZHANG, J. ; WU, X.. **Raman characterization on two-dimensional materials-based thermoelectricity.** *Molecules*, 24(1), 2019.

- [144] TUSCHEL, D.. **Photoluminescence spectroscopy using a Raman spectrometer**. Spectroscopy Solutions for Materials Analysis, 31(9):14–21, 2016.
- [145] BAYKARA, M. Z.; SCHWARZ, U. D.. **Atomic force microscopy: Methods and applications**. Elsevier Inc., 3 edition, 2016.
- [146] .. <https://upload.wikimedia.org/wikipedia/commons/5/5e/AFMsetup.jpg>.
- [147] NT-MDT. <https://www.ntmdt-si.com/products/afm-raman-nano-ir-systems/ntegra-spectra-ii>.
- [148] STOJILOVIC, N.. **Why can't we see hydrogen in X-ray photoelectron spectroscopy?** J. Chem. Educ., 89(10):1331–1332, 2012.
- [149] ORTEN, D.. **<Einstein-1905-Annalen_der_Physik.pdf>**. , .(.):., 1905.
- [150] HUFNER. **Photoelectron Spectroscopy**. Springer-Verlag Berlin Heidelberg GmbH, 2003.
- [151] WEIMER, J. J.. **X-RAY PHOTOELECTRON SPECTROSCOPY**. Wiley Online Library, p. 1493–1535, 2012.
- [152] .. <https://upload.wikimedia.org/wikipedia/commons/f/f2/System2.gif>.
- [153] FRANKEN, P. A.; HILL, A. E.; PETERS, C. W. ; WEINREICH, G.. **Generation of optical harmonics**. Phys. Rev. Lett., 7(4):118–119, 1961.
- [154] CHEN, H.; TANG, Y.; JIANG, T. ; LI, G.. **Nonlinear nanophotonics with 2D transition metal dichalcogenides**, volumen 1-5. Elsevier Ltd., 2019.
- [155] SUÑÉ, G. R.. **Electron beam lithography for Nanofabrication**. Nanomater. Nanostructures, Nanotechnologie, .(January):1–20, 2008.
- [156] RODDARO, S.; PINGUE, P.; PIAZZA, V.; PELLEGRINI, V. ; BELTRAM, F.. **The optical visibility of graphene: Interference colors of ultrathin graphite on SiO₂**. Nano Lett., 7(9):2707–2710, 2007.
- [157] NI, Z. H.; WANG, H. M.; KASIM, J.; FAN, H. M.; YU, T.; WU, Y. H.; FENG, Y. P. ; SHEN, Z. X.. **Graphene Thickness Determination Using Reflection and Contrast Spectroscopy**. Nano Letters, 2007.

- [158] LI, H.; WU, J.; HUANG, X.; LU, G.; YANG, J.; LU, X.; XIONG, Q. ; ZHANG, H.. **Rapid and Reliable Thickness Identification of Two-Dimensional Nanosheets Using Optical Microscopy.** ACS Nano, (Xx), 2013.
- [159] SHI, B.; ZHOU, D.; FANG, S.; DJEBBI, K.; FENG, S.; ZHAO, H.; TLILI, C. ; WANG, D.. **Facile and controllable synthesis of large-area monolayer WS₂ flakes based on WO₃ precursor drop-casted substrates by chemical vapor deposition.** Nanomaterials, 9(4), 2019.
- [160] MARTIN I. PECH-CANUL; RAVINDRA, N. M.. **Semiconductors Synthesis, properties and applications.** Springer, 2019.
- [161] LEE, J.-U.; PARK, J.; SON, Y.-W. ; CHEONG, H.. **Anomalous excitonic resonance Raman effects in few-layered MoS₂.** Nanoscale, 7(7):3229–3236, 2015.
- [162] CARVALHO, B. R.; WANG, Y.; MIGNUZZI, S.; ROY, D.; TERRONES, M.; FANTINI, C.; CRESPI, V. H.; MALARD, L. M. ; PIMENTA, M. A.. **Intervalley scattering by acoustic phonons in two-dimensional MoS₂ revealed by double-resonance Raman spectroscopy.** Nature Communications, 8(1):14670, 2017.
- [163] CHEN, J. M.; WANG, C. S.. **Second order Raman spectrum of MoS₂.** Solid State Commun., 14(9):857–860, 1974.
- [164] CHAKRABORTY, B.; MATTE, H. S. S. R.; SOOD, A. K. ; RAO, C. N. R.. **Layer-dependent resonant Raman scattering of a few layer MoS₂.** J. Raman Spectrosc., 44(1):92–96, 2013.
- [165] CARVALHO, B. R.; WANG, Y.; MIGNUZZI, S.; ROY, D.; TERRONES, M.; FANTINI, C.; CRESPI, V. H.; MALARD, L. M. ; PIMENTA, M. A.. **Intervalley scattering by acoustic phonons in two-dimensional MoS₂ revealed by double-resonance Raman spectroscopy.** Nat. Commun., 8:1–8, 2017.
- [166] XIAO, S.; XIAO, P.; ZHANG, X.; YAN, D.; GU, X.; QIN, F.; NI, Z.; HAN, Z. J. ; OSTRIKOV, K. K.. **Atomic-layer soft plasma etching of MoS₂.** Sci. Rep., 6(December 2015):1–8, 2016.
- [167] SHI, W.; LIN, M. L.; TAN, Q. H.; QIAO, X. F.; ZHANG, J. ; TAN, P. H.. **Raman and photoluminescence spectra of two-dimensional nanocrystallites of monolayer WS₂ and WSe₂.** 2D Mater., 3(2):1–10, 2016.

- [168] GAUR, A. P. S.; SAHOO, S.; SCOTT, J. F. ; KATIYAR, R. S.. **Electron - Phonon interaction and double-resonance Raman studies in monolayer WS₂**. J. Phys. Chem. C, 119(9):5146–5151, 2015.
- [169] MOLAS, M. R.; NOGAJEWSKI, K.; POTEMSKI, M. ; BABIŃSKI, A.. **Raman scattering excitation spectroscopy of monolayer WS₂**. Sci. Rep., 7(1):1–8, 2017.
- [170] KIM, M. S.; NAM, G.; PARK, S.; KIM, H.; HAN, G. H.; LEE, J.; DHAKAL, K. P.; LEEM, J. Y.; LEE, Y. H. ; KIM, J.. **Photoluminescence wavelength variation of monolayer MoS₂ by oxygen plasma treatment**. Thin Solid Films, 590:318–323, 2015.
- [171] KOZAWA, D.; KUMAR, R.; CARVALHO, A.; KUMAR AMARA, K.; ZHAO, W.; WANG, S.; TOH, M.; RIBEIRO, R. M.; CASTRO NETO, A. H.; MATSUDA, K. ; EDA, G.. **Photocarrier relaxation pathway in two-dimensional semiconducting transition metal dichalcogenides**. Nat. Commun., 5:1–7, 2014.
- [172] GUTIÉRREZ, H. R.; PEREA-LÓPEZ, N.; ELÍAS, A. L.; BERKDEMIR, A.; WANG, B.; LV, R.; LÓPEZ-URÍAS, F.; CRESPI, V. H.; TERRONES, H. ; TERRONES, M.. **Extraordinary room-temperature photoluminescence in triangular WS₂ monolayers**. Nano Lett., 13(8):3447–3454, 2013.
- [173] MAK, K. F.; LEE, C.; HONE, J.; SHAN, J. ; HEINZ, T. F.. **Atomically thin MoS₂: A new direct-gap semiconductor**. Phys. Rev. Lett., 105(13):2–5, 2010.
- [174] ZHOU, B.; YANG, L.; CHEN, F.; XU, M.; WU, T.; WU, G.; CHEN, X. ; FENG, D.. **Evolution of Electronic Structure in Atomically Thin Sheets of WS₂ and WSe₂**. ACS Nano, 7(Xx):1, 791–797, 2013.
- [175] BOND, B. D.; JACOBS, W. M.. **The Thermal Decomposition of Sodium Nitrate**. Journal Chemical Society (A), p. 2–5, 1966.
- [176] BRUIX, A.; FÜCHTBAUER, H. G.; TUXEN, A. K.; WALTON, A. S.; ANDERSEN, M.; PORSGAARD, S.; BESENBACHER, F.; HAMMER, B. ; LAURITSEN, J. V.. **In Situ Detection of Active Edge Sites in Single-Layer MoS₂ Catalysts**. ACS Nano, 9(9):9322–9330, 2015.
- [177] GIANNOZZI, P.; BARONI, S.; BONINI, N.; CALANDRA, M.; CAR, R.; CAVAZZONI, C.; CERESOLI, D.; CHIAROTTI, G. L.; COCCIONI, M.;

- DABO, I.; CORSO, A. D.; DE GIRONCOLI, S.; FABRIS, S.; FRATESI, G.; GEBAUER, R.; GERSTMANN, U.; GOUGOUSSIS, C.; KOKALJ, A.; LAZZERI, M.; MARTIN-SAMOS, L.; MARZARI, N.; MAURI, F.; MAZZARELLO, R.; PAOLINI, S.; PASQUARELLO, A.; PAULATTO, L.; SBRACCIA, C.; SCANDOLO, S.; SCLAUZERO, G.; SEITSONEN, A. P.; SMOGUNOV, A.; UMARI, P. ; WENTZCOVITCH, R. M.. **QUANTUM ESPRESSO: a modular and open-source software project for quantum simulations of materials.** *Journal of Physics: Condensed Matter*, 21(39):395502, sep 2009.
- [178] CAROZO, V.; WANG, Y.; FUJISAWA, K.; CARVALHO, B. R.; MCCREARY, A.; FENG, S.; LIN, Z.; ZHOU, C.; PEREA-LÓPEZ, N.; ELÍAS, A. L.; KABIUS, B.; CRESPI, V. H. ; TERRONES, M.. **Optical identification of sulfur vacancies: Bound excitons at the edges of monolayer tungsten disulfide.** *Sci. Adv.*, 3(4):e1602813, 2017.
- [179] ROSSI, T. P.; WINTHER, K. T.; JACOBSEN, K. W.; NIEMINEN, R. M.; PUSKA, M. J. ; THYGESEN, K. S.. **Effect of edge plasmons on the optical properties of MoS₂ monolayer flakes.** *Phys. Rev. B*, 96(15), 2017.
- [180] LI, H.; CONTRYMAN, A. W.; QIAN, X.; ARDAKANI, S. M.; GONG, Y.; WANG, X.; WEISSE, J. M.; LEE, C. H.; ZHAO, J.; AJAYAN, P. M.; LI, J.; MANOHARAN, H. C. ; ZHENG, X.. **Optoelectronic crystal of artificial atoms in strain-textured molybdenum disulphide.** *Nat. Commun.*, 6(May):6–11, 2015.
- [181] CHANG, H. Y.; YOGESH, M. N.; GHOSH, R.; RAI, A.; SANNE, A.; YANG, S.; LU, N.; BANERJEE, S. K. ; AKINWANDE, D.. **Large-Area Monolayer MoS₂ for Flexible Low-Power RF Nanoelectronics in the GHz Regime.** *Adv. Mater.*, 28(9):1818–1823, 2016.
- [182] HENRIE, J.; KELLIS, S.; SCHULTZ, S. M. ; HAWKINS, A.. **Electronic color charts for dielectric films on silicon.** *Opt. Express*, 12(7):1464, 2004.
- [183] YOON, D.; MOON, H.; SON, Y. W.; CHOI, J. S.; PARK, B. H.; CHA, Y. H.; KIM, Y. D. ; CHEONG, H.. **Interference effect on Raman spectrum of graphene on SiO₂/Si.** *Phys. Rev. B - Condens. Matter Mater. Phys.*, 80(12):1–21, 2009.
- [184] SHOUTE, L. C.; BERGREN, A. J.; MAHMOUD, A. M.; HARRIS, K. D. ; MCCREERY, R. L.. **Optical interference effects in the design**

- of substrates for surface-enhanced raman spectroscopy. *Appl. Spectrosc.*, 63(2):133–140, 2009.
- [185] LIANG, L.; MEUNIER, V.. **First-principles Raman spectra of MoS₂, WS₂ and their heterostructures.** *Nanoscale*, 6(10):5394–5401, 2014.
- [186] QIAO, S.; YANG, H.; BAI, Z.; PENG, G. ; ZHANG, X.. **Identifying the number of WS₂ layers via Raman and photoluminescence spectrum.** *Advances in Engineering Research*, 141(lcmmcce):1408–1413, 2017.
- [187] YUANZHENG, L.; XINSHU, L.; TONG, Y.; GUOCHUN, Y.; HEYU, C.; CEN, Z.; QIUSHI, F.; JIANGANG, M.; WEIZHEN, L.; HAIYANG, X.; YICHUN, L. ; XINFENG, L.. **Accurate identification of layer number for few-layer WS₂ and WSe₂ via spectroscopic study.** *Nanotechnology*, 29(12):124001, 2018.
- [188] MILTOS MARAGKAKIS, G.; PSILODIMITRAKOPOULOS, S.; MOUCHLIADIS, L.; PARADISANOS, I.; LEMONIS, A.; KIOSEOGLOU, G. ; STRATAKIS, E.. **Imaging the crystal orientation of 2D transition metal dichalcogenides using polarization-resolved second-harmonic generation.** *Opto-Electronic Adv.*, 2(11):19002601–19002608, 2019.
- [189] QI, Z.; CAO, P. ; PARK, H. S.. **Density functional theory calculation of edge stresses in monolayer MoS₂.** *J. Appl. Phys.*, 114(16):1–5, 2013.
- [190] BOYD, R.. **R. Boyd, Nonlinear Optics (Academic, London, 2008).** Elsevier Inc., 2008.
- [191] VIANNA, P. G.; HAMZA SAFEER, S.; ORE, A. S.; GORDO, V. O.; CARVALHO, I. C.; CAROZO, V. ; DE MATOS, C. J.. **Synthesis and Characterization of MoS₂/WS₂ Heterostructures by Second Harmonic Generation.** 2019 Sbfot. Int. Opt. Photonics Conf. Sbfot. IOPC 2019, .:4–7, 2019.
- [192] SAGAR, A.; BALASUBRAMANIAN, K.; BURGHARD, M.; KERN, K. ; SORDAN, R.. **Polymer-electrolyte gated graphene transistors for analog and digital phase detection.** *Appl. Phys. Lett.*, 99(4):2009–2012, 2011.
- [193] DAS, A.; PISANA, S.; CHAKRABORTY, B.; PISCANEC, S.; SAHA, S. K.; WAGHMARE, U. V.; NOVOSELOV, K. S.; KRISHNAMURTHY, H. R.;

- GEIM, A. K.; FERRARI, A. C. ; SOOD, A. K.. **Monitoring dopants by Raman scattering in an electrochemically top-gated graphene transistor.** *Nat. Nanotechnol.*, 3(4):210–215, 2008.
- [194] MAK, K. F.; LUI, C. H.; SHAN, J. ; HEINZ, T. F.. **Observation of an electric-field-induced band gap in bilayer graphene by infrared spectroscopy.** *Phys. Rev. Lett.*, 102(25):100–103, 2009.
- [195] EFETOV, D. K.; KIM, P.. **Controlling electron-phonon interactions in graphene at ultrahigh carrier densities.** *Phys. Rev. Lett.*, 105(25):2–5, 2010.
- [196] YAN, J.; HENRIKSEN, E. A.; KIM, P. ; PINCZUK, A.. **Observation of anomalous phonon softening in bilayer graphene.** *Phys. Rev. Lett.*, 101(13):26–29, 2008.
- [197] SCHWIERZ, F.; PEZOLDT, J. ; GRANZNER, R.. **Two-dimensional materials and their prospects in transistor electronics.** *Nanoscale*, 7(18):8261–8283, 2015.
- [198] TONG, X.; ASHALLEY, E.; LIN, F.; LI, H. ; WANG, Z. M.. **Advances in MoS₂-Based Field Effect Transistors (FETs).** *Nano-Micro Lett.*, 7(3):203–218, 2015.
- [199] DHAR, S.; PATTANAIK, M.. **Layered TMDFETS for Nano Devices: A Short Review.** *J. At. Mol. Condens. Nano Phys.*, 6(3):191–198, 2019.
- [200] BENKA, S. G.. **Two-dimensional atomic crystals.** *Phys. Today*, 58(9):9–9, 2005.
- [201] ŞAR, H.; ÖZDEN, A.; YORULMAZ, B.; SEVIK, C.; KOSKU PERKGOZ, N. ; AY, F.. **A comparative device performance assesment of CVD grown MoS₂ and WS₂ monolayers.** *J. Mater. Sci. Mater. Electron.*, 29(10):8785–8792, 2018.
- [202] GONG, Y.; LIN, J.; WANG, X.; SHI, G.; LEI, S.; LIN, Z.; ZOU, X.; YE, G.; VAJTAI, R.; YAKOBSON, B. I.; TERRONES, H.; TERRONES, M.; TAY, B. K.; LOU, J.; PANTELIDES, S. T.; LIU, Z.; ZHOU, W. ; AJAYAN, P. M.. **Vertical and in-plane heterostructures from WS₂/MoS₂ monolayers.** *Nat. Mater.*, 13(12):1135–1142, 2014.
- [203] YAN, J.; ZHANG, Y.; KIM, P. ; PINCZUK, A.. **Electric field effect tuning of electron-phonon coupling in graphene.** *Phys. Rev. Lett.*, 98(16):1–4, 2007.

- [204] MCDONNELL, S.; ADDOU, R.; BUIE, C.; WALLACE, R. M. ; HINKLE, C. L.. **Defect-DOMINATED DOPING and CONTACT RESISTANCE in MoS₂**. ACS Nano, 8(3):2880–2888, 2014.
- [205] LEE, C.; JEONG, B. G.; YUN, S. J.; LEE, Y. H.; LEE, S. M. ; JEONG, M. S.. **Unveiling Defect-Related Raman Mode of Monolayer WS₂ via Tip-Enhanced Resonance Raman Scattering**. ACS Nano, 12(10):9982–9990, 2018.